

GRAPHENE – MELAMINE COMPOSITES

MICROSTRUCTURE AND ORGANIC FILM ASSEMBLY

Dissertation zur Erlangung des akademischen Grades

Dr. rer. nat.

im Fach Technische Chemie

Alexander Kröger

Geboren am 13.06.1984 in Steinheim

1st supervisor: Prof. Dr. Wolfgang Bremser

2nd supervisor: Prof. Dr. Jörg K.N. Lindner

ACKNOWLEDGEMENT

Before jumping to the actual content of this thesis I would like to express some thoughts that come to mind when looking back at the last years. The time I spent in the workgroup of Wolfgang Bremser was enriching in a variety of ways, both on a professional and a personal level. When I started this thesis I was under the impression that the life I became a custom to had to stop in order to grow. However, Wolfgang was and hopefully still is convinced that doctoral studies are best perceived as an extended “play time”. The resulting professional and personal freedom to do whatever I felt was right was a unique experience. For granting this environment I would like to express my deepest gratitude to Wolfgang Bremser. Over the years I have met many colleagues who have influenced both my personal and professional life. I would like to express my gratitude to Karl Hiltrop who in my view is one of the most critical thinking and honest people I have met. I do and will miss the professional discussions with him. Further I would like to thank Oliver Seewald, whom I got to know in my first year of university. He enriched the working atmosphere with his joyful and open personality. Not being educated as a coating engineer but rather as an inorganic chemist his view on things enriched many discussions and opened up new ways of approaching things. The youngest colleague, although older than me, I would like to thank individually is Daniel Briesenick. I got to know him a couple of years ago when he was doing his project-based study on one of my projects. His different engineering inspired approach enriched the workgroup. Even though we “had to share” an office the last two years were lots of fun. So thank you, not only for the SEM images. I would like to thank all my other colleagues who made up the working environment like I perceived it – a great

opportunity to develop personally and professionally. Finally I would like to thank my parents and grandparents who no matter what always believed in me. I sincerely hope I did not forget anyone who would have deserved to be addressed in this chapter.

Enjoy reading this book.

ABSTRACT

The development of novel electrically conductive materials holds great potential for a variety of applications. The carbon allotrope graphene combines electrical conductivity with mechanical strength and flexibility. The most promising route towards large-scale, ecologically reasonable graphene synthesis relies on production of aqueous dispersions. Aqueous graphene dispersions are easily deposited to yield conductive thin films (TCFs). TCFs serve as starting point for development of conductive composite materials and flexible electronic devices. The incompatibility of graphene and water requires utilization of stabilizing agents. Since the material itself is hardly chemically reactive, interaction between graphene and suitable stabilizer molecules mainly relies on physical adsorption processes.

Hexamethoxymethyl melamine (HMMM) is a widely used cross-linking agent in the coatings industry and was previously employed to synthesize aqueous nano particle dispersions (MP). The particles possess positive surface charge. MP-polymer composites exhibit enhanced hardness compared to the unmodified polymer matrix. In addition it was shown that s-triazines in general show a high affinity towards graphene and some were successfully employed for synthesis of graphene composite dispersions. This study consists of six interrelated sections on HMMM and graphene.

HMMM shows a complex phase behavior in water which strongly depends on concentration and temperature. Up to 10 g/L the HMMM system consists solely of emulsion droplets with diameters around 150 nm (HMMM in water emulsion, H/W). Between 10 and 50 g/L HMMM exhibits both emulsion and microemulsion droplets. Above 50 g/L the system consists solely of

microemulsion droplets. The droplet diameters range between 2 and 10 nm and depend on the actual concentration and age of the mixture. In addition aqueous HMMM systems exhibit a concentration dependent phase inversion. Determined inversion temperatures vary from 30 to 60 °C. The resulting water in HMMM emulsions (W/H) exhibit diameters above 1 µm. Due to ageing, the phase inversion temperature increases with time.

HMMM nano particle dispersions were synthesized using educt concentrations between 10 and 55 g/L. This range corresponds to the presence of both emulsion and microemulsion droplets. Beyond the lower threshold successful synthesis is not possible. Higher concentrations cause sedimentation of excess MP as aggregates. The process is based on acid-catalyzed self-condensation of HMMM methoxy groups. The reaction temperature has to exceed the phase inversion temperature of the system. Kinetic analyses of the complex reaction revealed an activation energy of 136 kJ/mol. By varying the amount of catalyst and thus the pH value of the educt mixture the resulting particle diameters can be controlled between 5 and 250 nm. Particle growth occurs anisotropically. In contrast to sphere-like primary particles larger particles exhibit disc-like structures. The determined zeta potentials do not depend on either catalyst concentration or particle diameter. Measured values range between +25 mV and +40 mV. The positive charge originates from protonated dimethylene ether bridges. Spectroscopic results confirm the presence ternary hydrogen bonds. The particles are partially crystalline. X-ray and FTIR measurements revealed that stacking of triazine rings is a major structural characteristic.

Aqueous graphene dispersions were synthesized using both HMMM emulsions and HMMM nano particle dispersions. Graphene-HMMM hybrid dispersions ($G-M^{\ominus}$) were synthesized by ultrasonic exfoliation of graphite in HMMM emulsions at concentrations equal to or below 10 g/L. The grey to black colored dispersions contain up to 0.26 mg/ml single- and multilayer graphene. Single

layer graphene dispersions were prepared with concentrations up to 0.043 mg/ml. The majority of G-M[⊕] particle diameters range between 50 and 900 nm. Larger particles with several micron in diameter were detected as well. Above pH 4.1 the particles exhibit negative zeta potentials around -40 mV. The origin of the negative surface charge is a charge transfer from graphene to adsorbed HMMM molecules. In addition, π -stacking interactions contribute to the overall stability. Positively charged G-M[⊕] is stable at pH 3.5. Lower values cause rapid precipitation.

Aqueous graphene HMMM nano particle hybrid dispersions (G-MP[⊕]) were synthesized accordingly. Ultrasonic exfoliation of graphite in MP dispersions yielded dark grey to black colored dispersions with graphene concentrations up to 0.8 mg/ml. Particle diameters range between 50 and 1000 nm. The hybrid particle height depends on MP height thus amounts to at least 11 nm. This corresponds to MP adsorbed to both sides of a graphene sheet. Up to pH 10.9 G-MP[⊕] dispersions are positively charged. Higher pH values cause rapid precipitation due to lack of negative charge carriers. Zeta potentials range between +30 and +60 mV. The complex interaction mechanisms is based on π -stacking interactions, hydrogen bridges and cation- π interactions.

Cathodic electrodeposition (C-ED) of G-MP[⊕] results in highly conductive transparent graphene thin films. The deposited films exhibit thicknesses between 11 and 105 nm. Thickness control relies on deposition voltage, duration and G-MP[⊕] concentration. Monolayer films with thickness around 12 nm exhibit conductivities up to $3 \cdot 10^4$ Sm⁻¹. Higher film thickness causes a decrease in conductivity and ultimately yields insulating films. Electroosmotic effects cause formation of separate patches of stacked G-MP[⊕] and diffusion of MP to the surface. This results in formation of an insulating MP layer. Both effects contribute to the overall decreasing conductivity.

Layer-by-layer assembly (LBL) of G-MP[⊕] and G-M[⊖] results in densely packed, smooth graphene thin films. LBL films were prepared by dip (D-LBL) and spray (S-LBL) coating. Optimal deposition conditions were elaborated regarding deposition time and dispersion pH values. G-M[⊖] was deposited at pH 8.2, G-MP[⊕] was deposited at pH 6.5. Dip deposition of each dispersion was performed for 20 minutes, spray deposition for 5 seconds. S-LBL films are prepared in a fraction of the time necessary for D-LBL and exhibit lower roughness, higher transmission and lower double layer thickness (one layer of both G-M[⊖] and G-MP[⊕]). By choosing the suitable number of double layers the thickness of the deposited films can accurately controlled between 15 and 300 nm.

CONTENTS

CHAPTER I - INTRODUCTION.....	13
CHAPTER II – THEORETICAL BACKGROUND	19
2.1 HISTORICAL OVERVIEW	20
2.2 STRUCTURE AND ELECTRONIC PROPERTIES OF GRAPHENE	23
2.2.1 <i>Electronic Structure of Graphene</i>	24
2.2.2 <i>Massless Dirac Fermions in Graphene</i>	28
2.3 CHARGE CARRIER MOBILITY AND CONDUCTIVITY.....	30
2.4 GRAPHENE PROPERTIES AND APPLICATIONS	34
2.5 PHONONS AND RAMAN ACTIVITY OF GRAPHENE	36
2.5.1 <i>Raman G and G' Bands in Graphene</i>	38
2.6 GRAPHENE SYNTHESIS	41
2.6.1 <i>Micromechanical Cleavage</i>	41
2.6.2 <i>Graphitization of Silicon Carbide</i>	42
2.6.3 <i>Chemical Vapor Deposition of Epitaxial Graphene</i>	44
2.6.4 <i>Chemically Converted Graphene Oxide</i>	46
2.6.4.1 <i>Graphite Oxide</i>	46
2.6.4.2 <i>Graphene Oxide</i>	48
2.6.4.3 <i>Reduced Graphene Oxide</i>	50
2.6.5 <i>Pristine Graphene Dispersions</i>	52
2.6.5.1 <i>Solvent-Borne Graphene Dispersions</i>	52
2.6.5.2 <i>Aqueous Graphene Dispersions</i>	54
2.7 INTERACTION MECHANISMS IN GRAPHENE COMPOSITE SCIENCE.....	57
2.7.1 <i>π-stacking Interactions</i>	57
2.7.2 <i>Ion-π Interactions</i>	58
2.7.3 <i>Charge-Transfer Interactions</i>	58

2.8 GRAPHENE THIN FILMS	60
2.8.1 Layer-by-Layer Assembly of Functional Graphene (LBL)	60
2.8.2 Electrodeposition of Functionalized Graphene (ED).....	64
2.8.3 Langmuir-Blodgett Films (LB).....	<i>Fehler! Textmarke nicht definiert.</i>
2.9 HEXAMETHOXYMETHYL MELAMINE – PROPERTIES AND APPLICATIONS.....	68
2.10 EMULSIONS AND MICROEMULSIONS	71
CHAPTER III – PHASE BEHAVIOR OF AQUEOUS HMMM SYSTEMS	73
3.1 INTRODUCTION	74
3.2 EXPERIMENTAL	75
3.2.1 Preparation of HMMM Systems.....	75
3.2.2 Analytical Studies.....	75
3.3 RESULTS.....	76
3.3.1 Estimation of HLB Value and Hansen Solubility Parameters.....	76
3.3.2 Phase Behavior as Function of Time and HMMM Concentration	77
3.3.3 HMMM Phase Inversion.....	81
3.4 SUMMARY AND CONCLUSIONS.....	83
CHAPTER IV – AQUEOUS HMMM NANO PARTICLE DISPERSIONS	85
4.1 INTRODUCTION	86
4.2 EXPERIMENTAL	87
4.2.1 Synthesis and Kinetic Studies.....	87
4.2.2 Analytical Studies.....	87
4.3 RESULTS	89
4.4 SUMMARY AND CONCLUSION	99
CHAPTER V – AQUEOUS GRAPHENE-HMMM COMPOSITES	101
5.1 INTRODUCTION	102
5.2 EXPERIMENTAL	103
5.2.1 Graphene-HMMM Composite Synthesis.....	103

5.2.2	<i>Analytical Studies</i>	104
5.2.3	<i>Computational Studies</i>	105
5.3	RESULTS.....	106
5.4	SUMMARY AND CONCLUSION.....	115
CHAPTER VI – AQUEOUS GRAPHENE-HMMM NANO PARTICLE COMPOSITES		117
6.1	INTRODUCTION	118
6.2	EXPERIMENTAL	119
6.2.1	<i>Synthesis of Nano Composites</i>	119
6.2.2	<i>Analytical Studies</i>	120
6.3	RESULTS.....	121
6.4	SUMMARY AND CONCLUSION	127
CHAPTER VII – ELECTRODEPOSITION OF FUNCTIONALIZED GRAPHENE.....		129
7.1	INTRODUCTION	130
7.2	EXPERIMENTAL	131
7.2.1	<i>Electrodeposition Experiments</i>	131
7.2.2	<i>Analytical Studies</i>	132
7.3	RESULTS.....	134
7.4	SUMMARY AND CONCLUSION	140
CHAPTER VIII – LAYER-BY-LAYER ASSEMBLY OF FUNCTIONALIZED GRAPHENE ..		143
8.1	INTRODUCTION	144
8.2	EXPERIMENTAL	145
8.2.1	<i>Layer-by-Layer Assembly Experiments</i>	145
8.2.2	<i>Analytical Studies</i>	146
8.3	RESULTS	147
8.4	SUMMARY AND CONCLUSION	153
CHAPTER IX – SUMMARY, CONCLUSIONS AND OUTLOOK.....		155

Chapter I

INTRODUCTION

Graphene has advanced to one of the most intriguing materials discovered. Due to its physical properties the two-dimensional material opens up new fields of research in both physics and chemistry. Starting with the discovery of the electric field of effect in graphene single layers by Novoselov and Geim in 2004, vast research has been conducted to utilize the electrical and mechanical properties in materials science and applied physics. Table 1.1 highlights some physical properties of graphene.

Table 1.1: Physical properties of graphene

Property	Determined value
Electrical conductivity	1700 Sm ⁻¹
Specific surface area	2630 m ² g ⁻¹
Thermal conductivity	5300 Wm ⁻¹ K ⁻¹
Young's modulus	1.1 TPa
Tensile strength	130 MPa
Transmittance of white light	97.7 %

Graphene synthesis is based on four different processes – micromechanical cleavage, chemical vapor deposition, graphitization of silicon carbide and suspension processing. Samples obtained from micromechanically cleaved graphite, chemical vapor deposition techniques and graphitization of silicon carbide possess high crystal quality. These techniques are primarily useful for applications like electronic devices, gas sensing technology or field effect transistors. Suspension processing of graphite and graphite oxide presents a versatile method for large-scale production of graphene. A second advantage is the facile chemical functionalization. Reduction and subsequent exfoliation of graphite oxide offers both compatibility with water and options for functionalization due to the various oxide groups of graphene oxide. The properties of the material are inferior to those of pristine graphene since the carbon network remains partially oxidized and corrupted after the reduction step.

In contrast to graphite oxide, suspension processing of graphite requires either the use of solvents like N-methyl pyrrolidone (NMP) or stabilizing agents. Exfoliation of graphite in NMP yields stable single layer graphene dispersions. However, NMP is controversial due to its physical and toxicological properties. Subsequent research showed that low boiling point solvents are also suitable for graphene dispersion synthesis. Aqueous graphene dispersions have received a much attention due to the obvious ecological advantages over solvent-borne systems. Exfoliation of graphite in water requires stabilizing agents since graphene reacts highly hydrophobic. Several routes towards aqueous graphene dispersions have been reported including use of emulsifiers, chemical functionalization and adsorption of polymers. Depending on the nature of the stabilizing agent several possible interaction mechanisms occur. Adsorption mechanisms mainly rely on π -stacking, cation- π and charge transfer interactions. The substance 2,4,6-triamino-s-triazine (melamine) is known to interact with the graphene surface.

Potential applications for graphene dispersions are versatile. Synthesis of mechanically reinforced and/or conductive polymer composites is widespread and complex research field. There are numerous reports on mechanically reinforced polymer composites using both pristine graphene and graphene oxide dispersions. Establishing electric conductivity in a polymer usually relies on processing of conductive polymers. The dispersed graphene sheets have to percolate in order to conduct electricity. The percolation of individual sheets however also implies re-stacking which decreases the overall performance of the polymer, especially its mechanical properties. Deposition of conductive graphene thin films offers several possibilities for subsequent processing in polymeric matrices, e.g. by manufacture of sandwich structures. However, owing to the mechanical stability and optical transmittance of the material the

main application of graphene thin films is production of flexible electronic devices.

There are two popular processes for deposition of graphene thin films – electrodeposition (ED) and layer-by-layer assembly (LBL). Electrodeposition of charged graphene sheets is a very fast method for thin film processing. The required electric charge of the sheets can be introduced by a variety of mechanisms, e.g. adsorption of metal cations or charge transfer interactions. The properties of the resulting films depend on the actual nature of the graphene samples. Characterization of the deposition process is difficult as it depends on many additional parameters including e.g. suspension conductivity, electrode setup and applied electric field. Layer-by-layer assembly (LBL) describes the alternating deposition of oppositely charged species. Like electrodeposition LBL of graphene requires charged sheets. By selecting specific negatively and positively charged graphene samples the resulting films offer a diverse possible properties. The process is mainly driven by diffusive forces hence is more time-consuming than electrodeposition. The main challenges of LBL include finding suitable deposition parameters and optimization of process time.

The triazine derivative hexamethoxymethyl melamine (HMMM) is used as a cross-linking agent in coatings technology. Despite the high industrial value of the material there is little information about microscopic properties. Acid catalyzed self-condensation of aqueous HMMM suspensions leads to highly reactive nano particle dispersions. The positively charged particles possess a rigid structure and are electrostatically stabilized. Based on the nature of HMMM the particle growth occurs anisotropically. Possible applications include the reinforcement of polymeric matrices.

This study consists of six interrelated research projects on HMMM and graphene. The first goal of this study is the characterization of HMMM phase behavior. The second part will elaborate the HMMM nano particle synthesis. In

the third and fourth part both HMMM emulsions and HMMM nano particle dispersions are employed for the synthesis of aqueous graphene dispersions. The last two parts deal with the deposition of the graphene dispersions by means of electrodeposition and layer-by-layer assembly.

Chapter II

THEORETICAL BACKGROUND

2.1 HISTORICAL OVERVIEW

The history of graphene began prior to its actual discovery by Novoselov and Geim in 2004 ^[1]. Graphene's timeline originates from two individual timelines of graphite and graphite oxide which join to form a third line around 1962. Both graphite's and graphite oxide's lines contribute significantly to the evolution of graphene. Graphite has been used in manufacture of black paintings for millennia. The pre-modern era began around 1500 when a huge deposit of natural graphite was found in Gray Knotts, England. Graphite was then used to mark sheep before the English crown realized its value for military weaponry. Graphite's high temperature resistance made it an ideal material for line molds in cannonball production ^[2, 3]. At the time people mistakenly were under the impression that graphite was actually galena (lead sulfide). This opinion manifested itself in the German word for pencil – Bleistift (lead pen). In 1779, Carl Wilhelm Scheele provided evidence that graphite consists purely of carbon instead of lead sulfide ^[4]. Ten years later, in 1789, the mineralogist Abraham Gottlob Werner deduced the name graphite from the Greek word $\gamma\rho\alpha\pi\eta\varepsilon\iota\upsilon$ (grafein, write) ^[5]. Apart from natural graphite Acheson managed to synthesize graphite from Carborundum (silicon carbide) in 1898, which was used as an abrasive agent at the time ^[6]. His process serves as a prototype of epitaxial graphene synthesis decades later.

To this point, little was known about structural and chemical properties of the material. The most noteworthy work on the structure of graphite was published in the early 20th century by Hull in 1917 and Bernal in 1924 ^[7,8]. While Hull was the first to propose the layered structure of graphite, Bernal managed to provide evidence for Hull's findings, thereby earning the glory ("Bernal stacking"). During the nuclear-enthusiastic post-world war decades, research on graphite intensified. In 1947 Wallace published the "Band theory of graphite" ^[9]. His findings had major impact on today's understanding of graphene's electrical

properties since he deduced graphite's electronic properties from those of a single, theoretical graphite sheet. Between 1957 and 1958 some inadequacies of Wallace's model were rectified in the Slonczewski-Weiss-McClure (SWM) model^[10,11]. The SWM model has been revisited multiple times to imply electron and hole pockets^[12] as well as multi-body effects including interlayer van der Waals forces^[13]. Due to graphite's mechanical and electronic properties, the material is widely used today. Applications include batteries, refractories, steelmaking, brake linings, pencils and so forth.

Although research on graphene oxide started as late as 2006^[14], the material already had nearly 150 years of history. In 1859, the English surgeon Benjamin Collins Brodie found that treatment of graphite with potassium chlorate and nitric acid for several hours results in swelling of the educt material^[15]. He called this prototype of graphite oxide "graphitic acid" due its acidic properties. During the next 100 years, Staudenmaier and Hummers proposed two other methods of preparing graphite oxide which, including Brodie's method and several minor modifications, comprise the majority of graphite oxide syntheses today^[16,17]. During the following decades little research on graphite oxide was published. Minor topics included potential applications like graphite oxide membranes, lithium ion batteries and intercalation compounds^[18-20]. However, there was disagreement about the actual structure of graphite oxide concerning both type and position of oxide functionalities. These misconceptions led Lerf and Klinowski to propose a structural model in 1998 which is generally accepted by the scientific community^[21]. Their work showed that graphite oxide's basal planes are primarily covered with hydroxy and epoxy functionalities while sheet edges are decorated with carboxyl and carbonyl groups. The expression graphene oxide was introduced in 2006 which ultimately makes today's graphene precursor its successor. From this point on the amount of reports about graphene oxide have vastly increased in number. This is attributed to its

intriguing properties and the extreme development of graphene research. Graphene oxide is used for e.g. mechanically improved polymer composites, paper-like materials, nano hybrid composites and biological as well as medical applications.

The history of graphene began as early as the 1960s when Badami first managed to prepare graphite monolayers from silicon carbide [22]. During the following years two groundbreaking experiments led to formation of graphite monolayers on platinum and nickel substrates by adsorption of small organic molecules [23,24]. However, the importance of these early experiments was not realized to an appropriate extent. In 1986 Boehm, who earlier managed to effectively produce reduced graphene oxide, proposed the name graphene for single layer carbon which was accepted and formalized by the International Union of Pure and Applied Chemistry (IUPAC) more than ten years later [25,26]. While single layer graphite was believed to gain its stability from an adequate substrate, the existence of freely floating graphene was thought not to be realistic. According to the Mermin-Wagner theorem 2D crystals with diameters larger than a few nanometers were supposed to be unstable [27,28]. In 1999, Ruoff tried to exfoliate graphite by mechanical cleavage which resulted in few-layer graphene. Isolation of single layer graphene sheets could not be confirmed [29]. Despite the common belief of 2D crystal instability, Geim and Novoselov managed to isolate graphene by mechanical cleavage of highly oriented pyrolytic graphite in 2004 [1]. In addition to their discovery they also managed to demonstrate some of the materials extraordinary physical properties during the following years. The discovery of the room temperature quantum Hall Effect and the electric field effect in graphene samples were an unexpected discoveries which led to graphene finding its place in modern physics.

2.2 STRUCTURE AND ELECTRONIC PROPERTIES OF GRAPHENE

Graphite is composed of individual graphene sheets stacked in an offset configuration with an interlayer spacing of 3.354 Å (Bernal stacking).

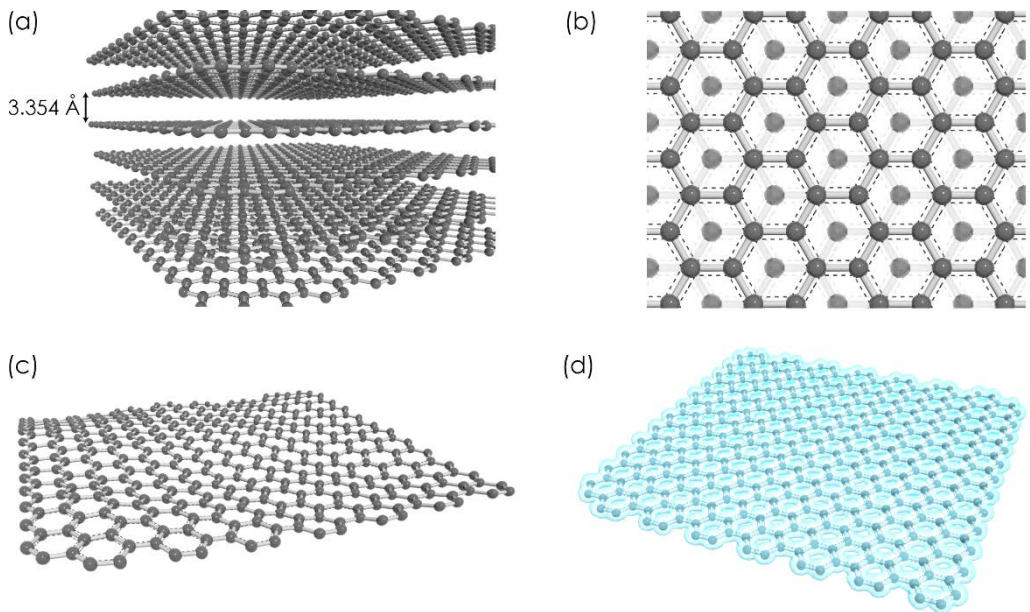


Figure 2.1: (a) Graphite; (b) Graphite top view; (c) Floating graphene sheet; (d) Electron density map of single layer graphene

The individual layers are held together via weak van der Waals forces and π -stacking interactions. Graphene sheets are composed of carbon atoms arranged in a hexagonal honeycomb lattice. The sp^2 carbon atoms form an aromatic π network due to the perpendicular oriented half-filled $2p_z$ orbitals. The graphene crystal lattice is composed of two triangular lattices of atoms A and B. The respective lattice vectors are ^[30]

$$\mathbf{a}_1 = \frac{a}{2} (3, \sqrt{3}), \quad \mathbf{a}_2 = \frac{a}{2} (3, -\sqrt{3}) \quad (2.1)$$

with the carbon-carbon distance of $a = 1.42$ Å. The respective reciprocal lattice vectors are given by

$$\mathbf{b}_1 = \frac{2\pi}{3a} (1, \sqrt{3}) \quad \text{and} \quad \mathbf{b}_2 = \frac{2\pi}{3a} (1, -\sqrt{3}) \quad (2.2)$$

The Dirac points K and K' are located at

$$\mathbf{K} = \left(\frac{2\pi}{3a}, \frac{2\pi}{3\sqrt{3}a} \right), \quad \mathbf{K}' = \left(\frac{2\pi}{3a}, -\frac{2\pi}{3\sqrt{3}a} \right) \quad (2.3)$$

and are of particular importance (figure 2.3).

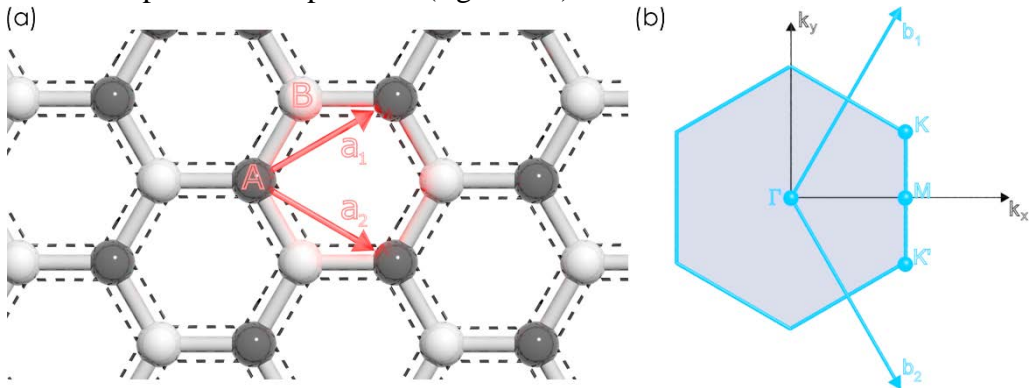


Figure 2.2: (a) Real space crystal lattice of graphene; (b) 1st Brillouin zone of graphene unit cell

K and K' are not connected by reciprocal lattice vectors hence individually contribute to the electronic behavior. This is a direct consequence of the crystal structure which is described as two trigonal Bravais lattices. In hexagonal lattices, the reciprocal lattice is in plane with the direct lattice. The lattice vectors \mathbf{b}_1 and \mathbf{b}_2 span an angle of 30° to the direct lattice vectors \mathbf{a}_1 and \mathbf{a}_2 .

2.2.1 ELECTRONIC STRUCTURE OF GRAPHENE

Graphene's electronic structure is described via the tight-binding approximation. Tight-binding approximation implies that there is only little overlap between electronic wave functions of neighboring atoms. This is a suitable description for the $2p_z$ orbitals of single layer graphene. The following derivation is in close analogy to the work of Castro Neto et al. [30]. The complete tight-binding

Hamiltonian for graphene electrons includes hopping between nearest neighboring and next-nearest neighboring atoms and reads

$$H = -t \sum_{\langle i,j \rangle, \sigma} (a_{\sigma,i}^\dagger b_{\sigma,j} + H.C.) - t' \sum_{\langle\langle i,j \rangle\rangle, \sigma} (a_{\sigma,i}^\dagger a_{\sigma,j} + b_{\sigma,i}^\dagger b_{\sigma,j} + H.C.)^1 \quad (2.4)$$

with

- $a_{\sigma,i}^\dagger, b_{\sigma,i}^\dagger$: Creation operators on sublattices A, B (Site \mathbf{R}_i , spin σ ($\sigma = \uparrow, \downarrow$))
- $a_{\sigma,j}, b_{\sigma,j}$: Annihilation operators on sublattices A,B (Site \mathbf{R}_j , spin σ ($\sigma = \uparrow, \downarrow$))
- t : Nearest neighbor hopping energy ($E \approx 2.8$ eV)
- t' : next-nearest neighbor hopping energy ($E \approx 0.1$ eV)

The Hamiltonian includes two energy terms. The left term describes hopping between nearest neighboring atoms and the right term describes hopping to next-nearest neighboring atoms. Hence, if an electron hops from atom A to atom B it is annihilated on A and created on B. The hopping energies cannot be predicted within the tight-binding approximation. Density functional theory (DFT) calculations resulted in values around 2.8 eV for t and values between 0.02t and 0.2t for t' . The energy bands derived from equation 2.4 read

$$E_{\pm}(\mathbf{k}) = \pm t \sqrt{3 + f(\mathbf{k})} - t' f(\mathbf{k}) \quad (2.5)$$

$$f(\mathbf{k}) = 2 \cos(\sqrt{3}k_y a) + 4 \cos\left(\frac{\sqrt{3}}{2}k_y a\right) \cos\left(\frac{3}{2}k_x a\right) \quad (2.6)$$

The positive sign applies to π^* band (hole-like states) and the negative sign to the π band (electron-like states). Further reading including a detailed derivation of equations 2.5 and 2.6 is provided by McCann [31].

¹ H.c. in this context means hermitian conjugate or, more descriptively, the vice versa creation and annihilation operation to creation on A site and annihilation on B site (in case of nearest-neighbor hopping)

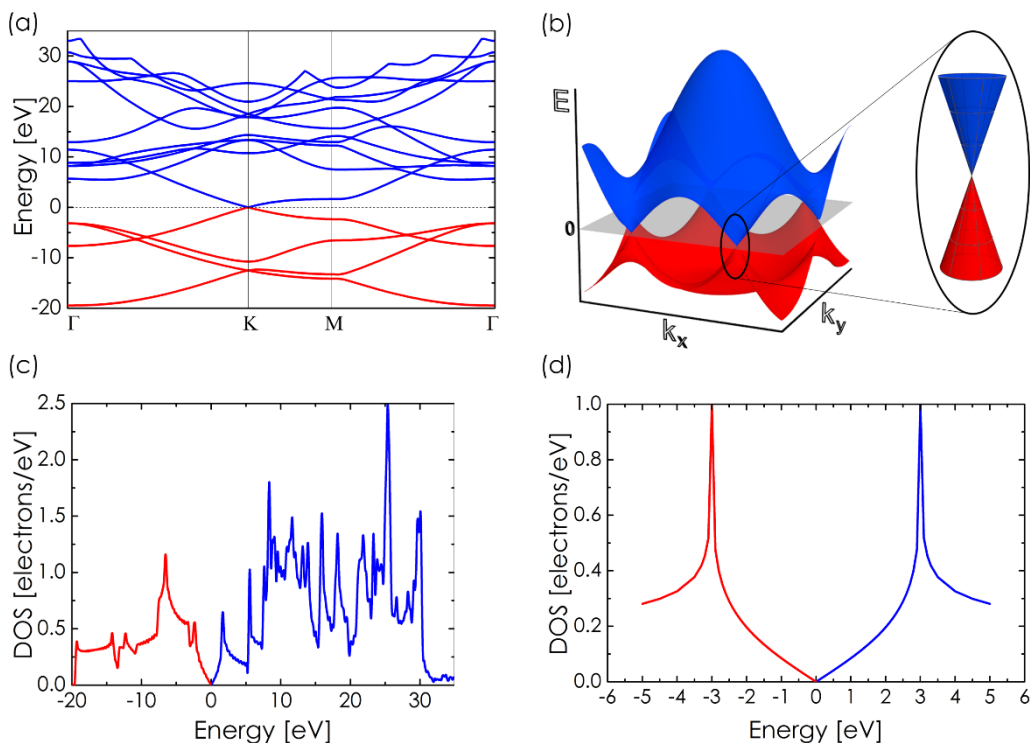


Figure 2.3: (a) Electronic dispersions of graphene; (b) Electronic dispersion in 1st Brillouin zone 3D; (c) Full density of states; (d) Density of states around Dirac point (analytical solution)

Since the $2p_z$ orbitals in pristine SLG are half filled, the valence band is completely filled by electron-like states while the conduction band is completely filled by hole-like states. Thus, the Fermi energy is exactly at $E_F = 0$. This result underlines that the electronic behavior of graphene is dominated by the low energy excitons around K and K'. Expansion of equation 2.5 around K (or K') ($\mathbf{k} = \mathbf{K} + \mathbf{q}$, $\mathbf{q} \ll \mathbf{K}$) results in the linear dispersion relation

$$E_{\pm} \approx \pm v_F |\mathbf{q}| + O\left[\left(\mathbf{q}/\mathbf{K}\right)^2\right] \quad (2.7)$$

with

\mathbf{q} : momentum relative to K/K'

v_F : Fermi velocity; $v_F = \frac{3ta}{2} \approx 10^6 \text{ ms}^{-1}$

Equation 2.7 closely resembles the dispersion relation of massless Dirac fermions. An analogous dispersion would be obtained by solving the 2D Dirac

equation. As a consequence of the electronic dispersion, the density of states (DOS) of single layer graphene exhibits an intriguing behavior. Calculation of DOS (only including nearest-neighbor hopping in the crystal lattice) via

$$\rho(E) = \frac{4}{\pi^2 t^2} \cdot \frac{1}{\sqrt{Z_0}} F\left(\frac{\pi}{2}, \sqrt{\frac{Z_1}{Z_0}}\right)^2 \quad (2.8)$$

with

$$Z_0 = \begin{cases} \left(1 + \left|\frac{E}{t}\right|\right)^2 - \frac{\left[\left(\frac{E}{t}\right)^2 - 1\right]^2}{4}, & -t \leq E \leq t \\ 4\left|\frac{E}{t}\right|, & -3t \leq E \leq -t \vee t \leq E \leq 3t \end{cases}$$

$$Z_1 = \begin{cases} 4\left|\frac{E}{t}\right|, & -t \leq E \leq t \\ \left(1 + \left|\frac{E}{t}\right|\right)^2 - \frac{\left[\left(\frac{E}{t}\right)^2 - 1\right]^2}{4}, & -3t \leq E \leq -t \vee t \leq E \leq 3t \end{cases}$$

is approximated around K and K' as

$$\rho(E) = \frac{dN(E)}{dE} = \frac{2|E|}{\pi\sqrt{3t^2}} \quad (2.9)$$

The DOS possesses zero density at the Fermi energy level, or in reciprocal space terms at the K and K' points (Figure 2.3). Calculation of the full density of states using computational methods results in broken symmetry distributions. In contrast to the analytical expression, DFT and other methods do not imply nearest-neighbor hopping only. Theoretically, the zero charge carrier density at the Fermi level would render graphene electrically insulating. The particular reasons for the contrary observed behavior in graphene are discussed in chapter 2.3.

² $F(\pi/2, x)$: Complete elliptical integral of the first kind; $F(x) = \int_0^{\pi/2} \frac{d\theta}{\sqrt{1 - x^2 \sin^2 \theta}}$

2.2.2 MASSLESS DIRAC FERMIONS IN GRAPHENE

The linearity of the energy dispersion in the Dirac valleys suggests that the excitations may be described by the two-dimensional Dirac equation for ultrarelativistic particles³ since there is high resemblance between both dispersion relations.

$$-iV_F \boldsymbol{\sigma} \cdot \nabla \psi(\mathbf{r}) = E \psi(\mathbf{r}) \quad (2.10)$$

The Dirac-Hamiltonian includes the constant Fermi velocity and the Pauli matrices

$$\boldsymbol{\sigma} = (\sigma_x, \sigma_y, \sigma_z) \quad \sigma_x = \begin{pmatrix} 0 & 1 \\ 1 & 0 \end{pmatrix}; \quad \sigma_y = \begin{pmatrix} 0 & -i \\ i & 0 \end{pmatrix}; \quad \sigma_z = \begin{pmatrix} 1 & 0 \\ 0 & -1 \end{pmatrix} \quad (2.11)$$

This analogy results in characteristic properties of low energy graphene excitons. The energy eigenvalues and eigenstates read

$$E_{\pm} = \pm V_F |\mathbf{q}| \quad (2.12)$$

$$\psi_{\pm, \mathbf{k}}(\mathbf{k}) = \frac{1}{\sqrt{2}} \begin{pmatrix} e^{-i\theta_k/2} \\ \pm e^{i\theta_k/2} \end{pmatrix} \quad (2.13)$$

$$\psi_{\pm, \mathbf{k}}(\mathbf{k}) = \frac{1}{\sqrt{2}} \begin{pmatrix} e^{i\theta_k/2} \\ \pm e^{-i\theta_k/2} \end{pmatrix} \quad (2.14)$$

where

$$\theta_k = \arctan \left(\frac{q_x}{q_y} \right) \quad (2.15)$$

is the angle between \mathbf{k} and x-axis. The signs of the spinor wave functions correspond to either conduction (hole-like) or valence band (electron-like). The two-components of the Hamiltonian and the eigenstates however do not represent electron spin but originate from the relative amplitude of the Bloch

³ Ultrarelativistic particles: Particles that move close to the speed of light. The respective dispersion relation is $E = cq$ derived from the general dispersion $E^2 = m^2c^4 + q^2c^2$ with $qc \gg mc^2$. In contrast, the classical particle dispersion can be approximated by $E = mc^2 + p^2/2m$

function on the two sublattices A and B (Figure 2.4)⁴. This so-called pseudospin represents an additional degree of freedom and has major influence the low-energy electronic behavior of graphene.

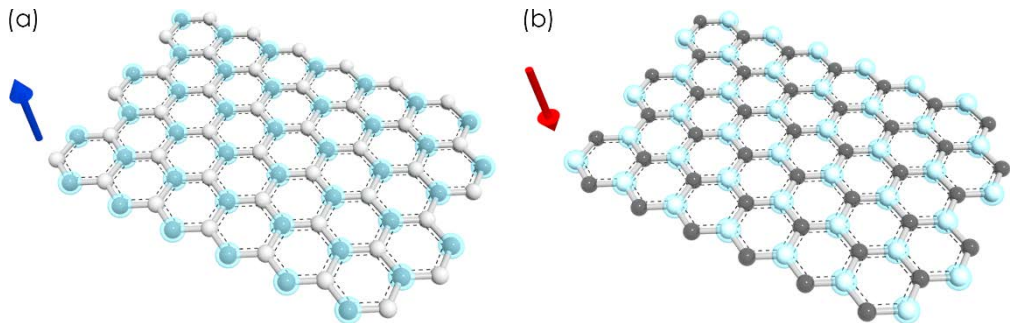


Figure 2.4: Graphene lattice with pseudospin (a) up and (b) down

Both pseudospin up and down represent limiting values. In a graphene lattice there is always mixing between these two states. Projection of the pseudospin on the direction of the electronic momentum results in electron chirality, or helicity⁵. The two concepts do not differ for massless fermions. This is the underlying cause for an observable Berry's phase of π and Klein tunneling in graphene. A geometric phase, or Berry's phase, of π is a characteristic property of spinors. In order to describe the behavior of pseudospin in relation to electronic momentum, the helicity operator

$$\hat{h} = \frac{1}{2} \boldsymbol{\sigma} \cdot \frac{\mathbf{p}}{|\mathbf{p}|} \quad (2.16)$$

is introduced. The two eigenvalues of σ describe right- and left-handed helicity. The direction notation corresponds to equal directions (right-handed) and

⁴ This is in close analogy to the physical origin of electron spin. The two components of a wave function satisfying the Dirac equation for an electron (the full description includes four components for electrons and positrons) originate from the fact that electron spin is generated by an incoming and an outgoing wave acting on a plane wave. Further reading is provided in specific literature^[32]

⁵ Chirality is a general concept to elementary particle physics. Since the velocity of massive fermions always depends on the observer, a definite chirality cannot be found. Instead massless fermions do have a constant velocity, hence possess a distinct chirality.

opposite directions (left-handed) of momentum and pseudospin, respectively. By this definition electrons possess right-handed helicity while holes possess left-handed helicity. The helicity is of course only valid in the low energy regime close to K and K'.

2.3 CHARGE CARRIER MOBILITY AND CONDUCTIVITY

Electric conductivity is one of the most intriguing properties of graphene. According to the Drude theory, conductivity depends on the two variables charge carrier density and mobility. Both quantities will be discussed in detail.

$$\sigma = n e \mu = \frac{n e^2 \tau}{m} \quad (2.17)$$

Charge carrier mobility may be determined by means of Hall resistance measurements or field effect measurements. Both methods have been used frequently to gain information about this quantity in graphene systems. According to this simplified model, charge carrier mobility depends on charge carrier mass, charge and the relaxation time. The most important variable in this context is the relaxation time which denotes the time a charge carrier can travel before encountering a scattering center. Scattering mechanisms in graphene are multifaceted. Depending on the actual device used for transport measurements, several different values for mobility have been reported. Early experiments of graphene on a substrate consisting of silica with a 300 nm top layer of silicon oxide (Si/SiO₂) revealed mobility values around 10000 cm²V⁻¹s⁻¹. Experiments on suspended graphene sheets yielded mobility values as high as 200.000 cm²V⁻¹s⁻¹ (table 2.1).

Table 2.1: Charge carrier mobilities of different graphene samples; Abbreviations: SiC-G: graphene obtained from graphitization of silicon carbide; CVD-G: Graphene obtained from chemical vapor deposition; MMC-G: Graphene obtained from micromechanical cleavage

Graphene sample	Charge carrier mobility [cm ² V ⁻¹ s ⁻¹]	Ref.
SiC-G, Ar atmosphere	1,850	[33]
CVD-G on copper	4,050	[34]
MMC-G on Si/SiO ₂	10,000	[35]
MMC-G on Si/SiO ₂ suspended	200,000	[36]
MMC-G between h-BN	500,000	[37]

Graphene exhibits the Klein paradox, or Klein tunneling, due to the chiral nature of its low energy excitons. Chirality in graphene causes a highly suppressed long-range backscattering probability of Dirac Fermions due to finite potentials. The effect accounts for the high mobility observed in suspended graphene devices. Suspended graphene, if properly annealed, exhibits flexural phonons as possible scatterers. These long range scatterers do not significantly impair the charge carrier mobility. Klein tunneling however does not affect short-range scatterers like ad-atoms or point defects. Without proper annealing the measured mobility is up to tenfold smaller, even in suspended samples,. Further reading on scattering mechanisms in graphene is provided in several reviews on graphene transport properties [33, 38, 39].

Charge carrier density is the second important factor influencing graphene conductivity. As already pointed out in chapter 2.2.1, pristine graphene has zero charge carrier density at the Fermi level which intuitively would lead to the conclusion that the material is an electrical insulator. This hypothetical type of sample is called intrinsic graphene. On the other hand doped graphene exhibits a finite charge carrier density and is denoted extrinsic graphene. In contrast to the theoretical expectations transport measurements indicate a quantum limited resistivity of about $4e^2/h$ [40-43]. The reason for this contradiction is quite trivial. Perfectly ordered, pristine graphene is not realistic. Every sample shows at least some amount of disorder owing to the various types of possible scatterers.

Computational studies revealed that disorder causes the density of states at the Fermi level to become finite, hence there is always some conductivity regardless of graphene source and device type. In the case of MMC-G on Si/SiO₂ it was shown that the random electrostatic potential of the substrate translates to the graphene sheet as electron and hole puddles [44, 45]. This effect is foremost accountable for the finite density of states (DOS) in these devices.

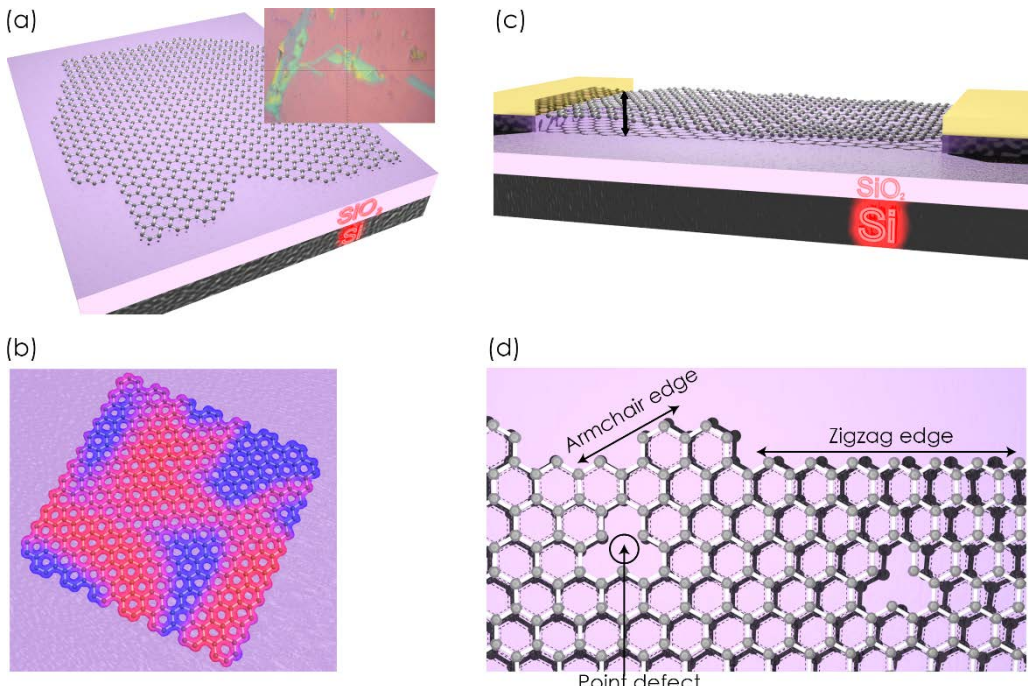


Figure 2.5: (a) Graphene on Si/SiO₂ substrate, inset: microscopic image; (b) Electrostatic potential puddles of graphene on Si/SiO₂; (c) Suspended graphene exhibiting flexural phonons as primary scattering mechanism; (d) Point defects and edges as secondary source of scattering in suspended graphene

As can be easily deduced from the DOS of graphene, the charge carrier density increases by a multitude above or below the Dirac point. Tuning of graphene by means of doping is commonly performed in two ways. Tuning of MMC-G, on Si/SiO₂ or suspended graphene by applying a suitable gate voltage has been investigated by several authors [1, 46-48]. The second method is chemical doping. Chemical doping of graphene by inducing charge-transfer interactions results in p- or n-doped samples. Most investigations on the subject have been done by

means of computational studies [49-55]. Due to the different mechanism involved, the measurable conductivity increases for p-doped graphene while n-doping decreases the conductivity. In reality, some amount of chemical doping is expected to occur in every sample due to the adsorption of small molecules. In fact it was shown that graphene is extremely sensitive to adsorption of single gas molecules. Further reading on this topic is provided by Schedin et al. [56]. In light of the increasing data available for charge-transfer interactions between graphene and suitable chemical species, this field of research holds great potential. The importance manifests itself in manufacture of transparent conductive graphene films (TCFs). TCFs are a promising means for economical manufacture of e.g. dye-sensitized solar cells and electronic devices.

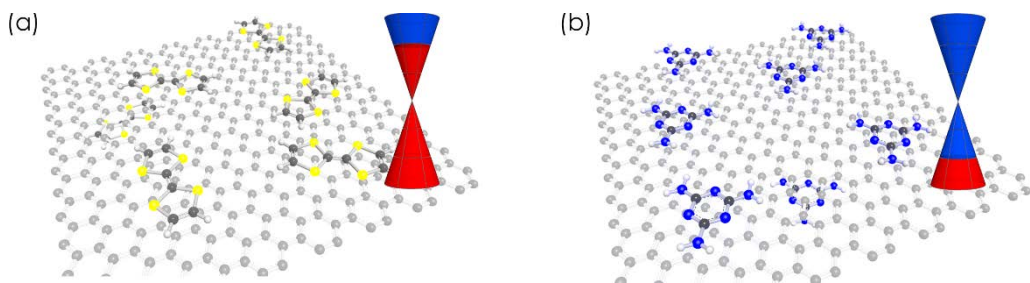


Figure 2.6: (a) n-doping in tetrathiafulvalene decorated graphene; (b) p-doping in melamine decorated graphene

Compounding single layer graphene and polymer matrices has been studied extensively. Electrically conductive polymers require direct contact between individual graphene layers. This introduces substantial problems regarding direct compounding using e.g. extrusion techniques. The high shear forces which are required for polymer processing cause folding of the graphene sheets which decreases contact probability. Further, re-agglomeration of individual sheets cannot be excluded. Conductive polymers are commonly used to act as bridges between individual graphene sheets.

2.4 GRAPHENE PROPERTIES AND APPLICATIONS

In addition to electrical conductivity, graphene exhibits several other interesting properties. A single layer of graphene with thickness of 0.354 nm is expected to be optically transparent. Within the independent electron approximation the optical transmittance may be calculated as [38]

$$T = \left| 1 + \frac{\sigma(\omega)}{2c\epsilon_0} \right|^{-2} \quad (2.18)$$

with

$$\sigma(\omega) = \sigma_0 \theta(\omega\hbar - 2E_F) + i\sigma_0 \frac{4E_F}{\pi\omega\hbar} - i\frac{\sigma_0}{\pi} \ln \left| \frac{\hbar\omega + 2E_F}{\hbar\omega - 2E_F} \right| \quad (2.19)$$

By inserting $E_F = 0$ for pristine graphene one obtains

$$T = 1 - \pi \frac{e^2}{4\pi\epsilon_0\hbar c} \approx 0.977 \quad (2.20)$$

This results indicates that a single layer of pristine graphene transmits 97.7 % of visible light. Although this value is high enough for processing of transparent electrodes, it is remarkable that a one-atom thick membrane is visible to the eye. Experimental verifications of the transmittance value are provided in several publications [57, 58].

The high diameter/height aspect ratio of graphene results in an extremely high specific surface area. In conjunction with the electronic properties several studies have geared towards manufacture of graphene electric double layer capacitors and single-molecule gas sensing devices [56, 59-62]. Theoretical calculations based on the actual surface area of a graphene hexagon and the atomic weight of carbon predict a theoretical value of $2630 \text{ m}^2/\text{g}$ [63]. The actual value of available surface area depends on graphene source and morphology. Measured values of graphene oxide and reduced graphene oxide are considerably lower owing to the structure of the samples. Reduction of available surface area is usually caused by re-

agglomeration, crumpling and folding of individual sheets. Insertion of spacer particles has been laid emphasis on in order to prevent these mechanisms [64-67]. Due to the strong σ -backbone of the two-dimensional crystal, graphene is expected to exhibit extreme mechanical properties. Lee et al. investigated the mechanical properties by means of atomic force microscopy. In their experiments they deposited single layer graphene sheets on top of a Si/SiO₂ substrate which contained an array of holes of varying diameter. Careful indentation experiments yielded extreme values for Young's modulus (1.1 TPa) and breaking strength (42 Nm⁻¹) [68]. The actual value depends on graphene crystal quality, hence crystal disorder decreases these values markedly. This effect accounts for the inferior properties of graphene oxide. Although the basic morphology is comparable to pristine graphene, the antecedent oxidation induces high amount of disorder which results in highest reported values around 470 GPa. The high Young's modulus and the high breaking strength make graphene an ideal material for polymer nano-composites. Incorporation of graphene into a polymer matrix generally enhances the overall mechanical performance [69-74]. The final performance depends on several parameters. Aside from graphene-matrix compatibility, parameters include graphene type, size and morphology, degree of exfoliation and re-agglomeration. The maximum graphene content must not exceed a specific threshold in order to improve mechanical properties. Crossing this threshold usually lowers the overall performance due to re-agglomeration. This factor plays a crucial role in formulating graphene-polymer composites. The effect is traced back to slipping of graphene sheets within the re-formed graphite crystallites. Further, in order to achieve the best results, especially with respect to impact resistance, orientation of the sheets within the matrix has to be taken into account.

Confocal micro-Raman studies were employed to probe the thermal conductivity of graphene. Balandin et al. utilized the temperature dependence of the Raman

G peak position to determine the thermal conductivity of suspended samples [75]. Values up to $5300 \text{ Wm}^{-1}\text{K}^{-1}$ were reported which is close to the theoretical value of carbon nano tubes [76]. For comparison purposes, diamond exhibits thermal conductivities up to $2300 \text{ Wm}^{-1}\text{K}^{-1}$. Values for polymeric materials range between 0.1 and $0.3 \text{ Wm}^{-1}\text{K}^{-1}$ [77]. In conjunction with the electronic properties the thermal conductivity highlights graphene's potential for electronic applications.

2.5 PHONONS AND RAMAN ACTIVITY OF GRAPHENE

Phonons represent the frequency dependent vibrational modes in solid matter [78-81]. Phonon dispersions can either be measured via inelastic X-ray scattering (limited to graphite) or calculated using various density functionals (DFT). Since the graphene unit cell consists of two atoms, there are three optical and three acoustical phonon branches. The degenerate in-plane longitudinal optical (iLO) and in-plane transversal optical (iTO) bands (E_{2g} representation) at the Brillouin zone center (Γ -point, $q = 0$) give rise to a 1st order Raman process. The process is accompanied by electron-hole creation processes. The resulting G band around 1582 cm^{-1} provides information about the electronic nature of the investigated graphene sample. A detailed discussion about the size and shape of this band follows (chapter 2.5.1).

Graphene shows several other bands related to second-order processes around the Dirac point K (K'). Kohn anomalies are observed around Γ and K in the phonon dispersions [82, 83]. The iLO branch shows Kohn anomalies around Γ and the iTO branch around K as indicated by the small kink in the dispersions. This kink closely resembles the linear energy dispersion around K and K'. The effect was first discovered by Walter Kohn in 1959 as a means for visualizing the Fermi

surface of metals. Kohn anomalies are a direct result of electron-phonon interactions. Conduction electrons screen lattice vibrations to a certain extent. At specific points, in the case of graphene Γ and K, this screening is determined by the shape of the Fermi surface. The presence of Kohn anomalies results in energy-dispersive Raman bands around Γ and K. This does not hold exactly at Γ and K. The effect has to be taken into account in discussion of Raman D and G' bands.

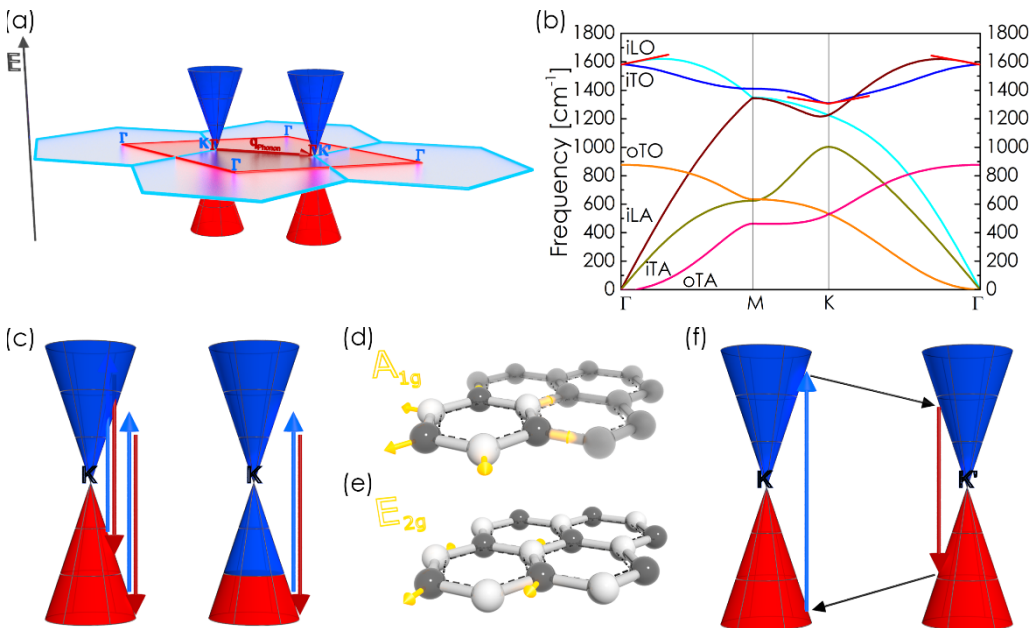


Figure 2.7: (a) 1st Phonon Brillouin zone; (b) Phonon dispersions of graphene, Kohn anomalies around G and K are depicted as red lines; (c) G band transitions of graphene; (d) Ring breathing A_{1g} mode; (e) E_{2g} mode; (f) Double resonance process leading to G' band

In addition to the 1st order G band Raman spectra of graphene show two additional characteristic bands, the D band around 1300 cm⁻¹ ($E_{\text{Laser}} = 2.4$ eV) and the G' band⁶ around 2700 cm⁻¹ ($E_{\text{Laser}} = 2.4$ eV). The D band originates from the iTO branch (A_{1g} representation) around K and is a second-order process

⁶ The nomenclature of the different Raman bands is determined by historical aspects and underwent partial changes due to misconceptions over the years. For further reference, G is short for “graphite” and D is short for “disorder”. Since for a long time there was disagreement one usually finds two designations for the Raman band around 2700 cm⁻¹. The process was not well understood and attributed to disorder in the investigated samples. Hence, in addition to the correct designation G' the designation 2D is still in use.

activated by defects in the crystal structure. In real space this mode is caused by ring breathing (figure 2.7e). The defect requirement arises from the fundamental Raman selection rule ($q = 0$). The wave vector has to be cut down by a defect structure in order for this band to be observed. The presence and shape of this band is therefore a direct measure of the graphene crystal quality. The G' band arises from the iTO branch as well, however in this second-order process there are two phonons involved. During the process an electron with wave vector \mathbf{k} at K absorbs incident laser light and is inelastically scattered by a phonon with wave vector \mathbf{q} to a point around K' ($\mathbf{k} + \mathbf{q}$). The electron is then backscattered to \mathbf{k} , emits a photon and recombines with a hole at K (figure 2.7f).

While several other Raman processes are possible the most important bands are the described G, the D and the G' band. These three signals alone contain plenty of information about graphene quality and electronic structure. For a more detailed description of other Raman processes in graphene and the underlying processes involved the reader is referred to several reviews and books about this topic [78, 84-86]. In the following the G and G' band are discussed in detail as they provide direct information about the degree of exfoliation and the electronic nature of graphene and graphene composites.

2.5.1 RAMAN G AND G' BANDS IN GRAPHENE

The Raman G and G' bands are highly sensitive to graphene layer count, doping, edges, mechanical stress, disorder and other factors [87-90]. In the present study Raman spectra were recorded to gain insight into degree of exfoliation and the electronic nature of graphene nanocomposites. These two factors will be discussed in detail.

The degree of exfoliation of graphite influences the shape of the G' band (figure 2.8). Graphite or multi-layer graphene (MLG) shows numerous superimposed bands leading to a high full width at half maximum (FWHM) of the G' peak. Due to the multi-layer structure there are several more Raman modes to consider. Bi-layer graphene already shows four distinct modes leading to a broadening of the peak, while single layer graphene exhibits a single Lorentzian shaped band. In addition, the G' band is red-shifted in SLG compared to MLG. Further, the relative ratio between G' and G increases with decreasing layer number. This effect can easily be understood by considering that more layers result in more E_{2g} vibrations. The G band further shows a red-shift which increases nearly linear with decreasing layer number. This shift arises from increasing substrate influence. In comparison to the usual Si/SiO_2 substrates the effect is even stronger when using sapphire substrates. Further, the $\text{FWHM}(G)$ which is about 16 cm^{-1} increases slightly. The straightforward interpretation is applicable for pristine graphene samples only since doping of any kind influences the shape of the peak as well.

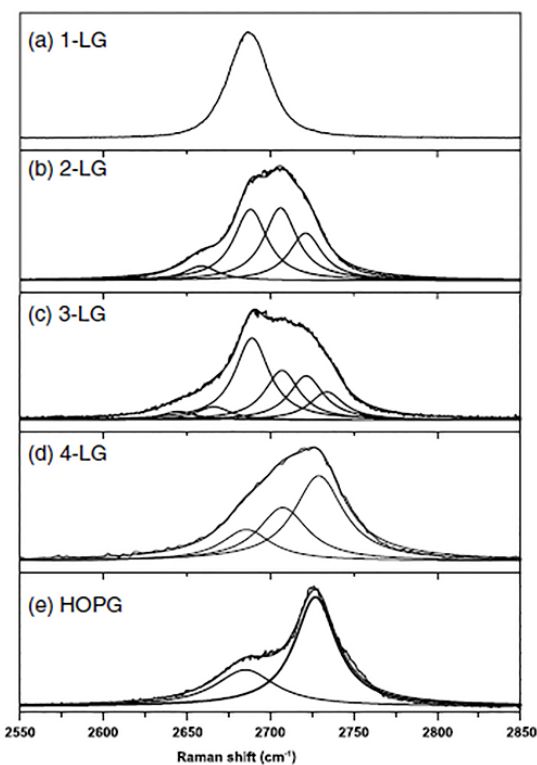


Figure 2.8: Dependence of G' band on graphene layer number^[80]

Both G and G' band show distinct features in chemically doped graphene. The underlying charge transfer interactions cause an opposite shift of the G band for

electron and hole doping. Subrahmanyam et al. investigated the interaction in graphene-tetrathiafulvalene (TTF, electron donor) and graphene-tetracyanoethylene (TCNE, electron acceptor) [90]. Graphene-TTF showed a blue-shift of the G band, while graphene-TCNE showed a redshift. Further it was shown that the extent of blue- or redshift is highly dependent on dopant concentration. Similar results were obtained by Das et al. who investigated graphene-nitrobenzene and graphene-aniline systems [91]. Due to its double-resonant nature, the G' is highly susceptible to doping. The G' band intensity decreases with increasing doping level. Excessive dopant concentration causes disappearance of the G' band. Like the G band, the G' band is sensitive to both n- (electron) and p- (hole). n-doping results in a blue-shift while p-doping causes a red-shift. The heightened Fermi level in n-doped graphene decreases the energy for electron-hole recombination, while the lowered level in p-doped does just the opposite. In real space this behavior can be interpreted as a stiffening or softening of the crystal lattice due to n- or p-doping respectively.

2.6 GRAPHENE SYNTHESIS

Graphene synthesis by micromechanical cleavage of graphite was introduced by Geim and Novoselov and receives special attention in the scientific community. Although it is often used for production of large-area, high-quality

graphene sheets, several other routes have been developed to circumvent the obvious disadvantages of the method. Modern graphene synthesis is primarily based on four different methods. Including micromechanical cleavage of graphite, these methods are chemical vapor deposition, graphitization of silicon carbide and suspension processing. Suspension processing is subdivided into graphite oxide and graphite exfoliation. Advantages and disadvantages will be elaborated to provide an overview of the different graphene types. Throughout scientific literature a plethora of acronyms are used to describe the respective synthesis methods. Table 2.2 provides an overview of the different routes and the acronyms used throughout this chapter.

Table 2.2: Acronyms of graphene prepared by different methods

Graphene synthesis method	Acronym
Micromechanical cleavage of graphite	MMC-G
Graphitization of silicon carbide	SiC-G
Chemical vapor deposition methods	CVD-G
Reduction of graphite oxide	rGO
Ultrasound-assisted liquid exfoliation	EG

2.6.1 MICROMECHANICAL CLEAVAGE

Micromechanical cleavage of highly oriented pyrolytic graphite (HOPG) is a top-bottom synthesis route for pristine single layer graphene sheets. Further and further cleavage of graphite ultimately leads to single layer graphene. Problems arise from distinguishing single layers from multi-layered graphene. Aside from

high resolution transmission electron microscopy and scanning probe microscopy graphene is visible in white light when deposited on a silicon substrate with a 300 nm silicon dioxide layer on top of it [92].

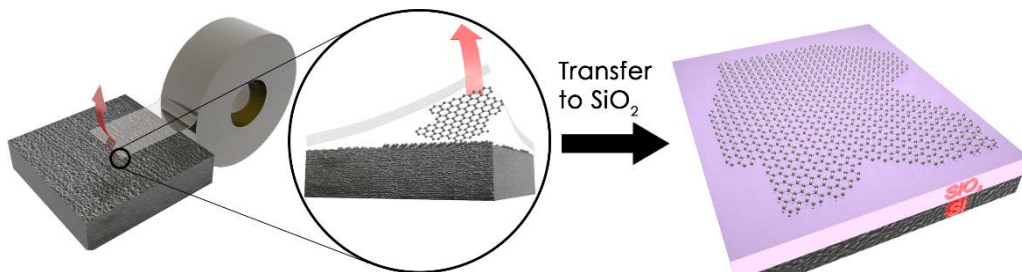


Figure 2.9: Micromechanical cleavage of HOPG yielding graphene and subsequent transfer to Si/SiO₂

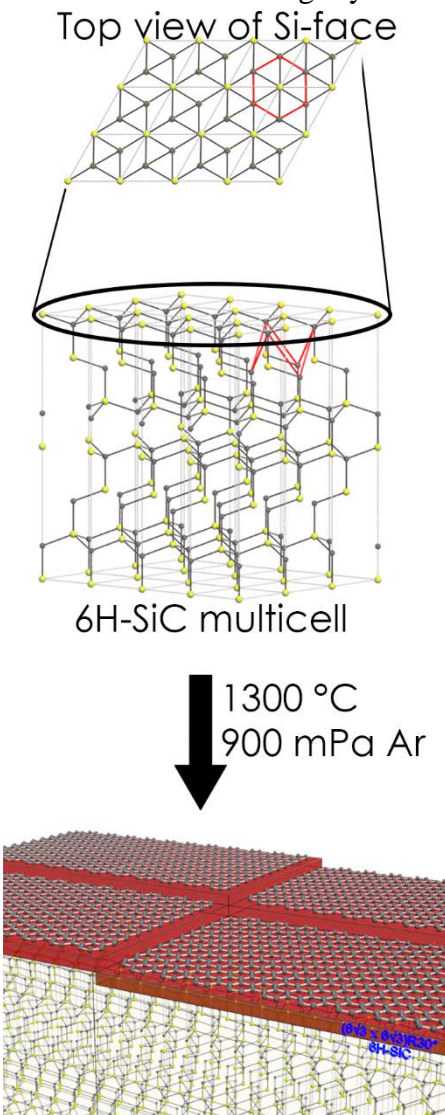
Since micromechanical cleavage is highly time-consuming and results not only in single layers but a mix of single- and multilayer graphene, the method is predestined for academic research. MMC-G is frequently used in studies related to transport and magnetic properties.

2.6.2 GRAPHITIZATION OF SILICON CARBIDE

Graphitization of silicon carbide laid the basis for epitaxial graphene synthesis. The first experiments were conducted by Busch in 1960 [93]. At 2000 °C in vacuo silicon carbide converts to graphite. The resulting graphite flakes possess a common c-axis orientation with the underlying substrate [94]. At high temperatures silicon atoms diffuse out of the crystal lattice and leave two layers of carbon atoms. These two layers collapse and form the hexagonal lattice structure of graphite. The resulting graphite exhibits ABAB stacking.

Production of SiC-G underlies the three parameters 6H-SiC crystal orientation, temperature and environment. The unit cell of silicon carbide has two faces, a silicon face and a carbon face [95, 96]. Most research on epitaxial graphene is performed using the Si-face. Graphitization of the C-face is slightly faster compared to the Si-face but yields a variety of crystal orientations [97, 98].

The reaction temperature primarily affects the resulting film roughness. Increasing temperature results in faster Si evaporation, hence faster graphene formation. In vacuum this usually results in poorly structured graphene films on a corrupted SiC surface. During the graphitization, the SiC surface is under constant $(6\sqrt{3} \times 6\sqrt{3})R30^\circ$ reconstruction due to Si evaporation [99]. Higher temperatures cause faster surface diffusion processes which would result in smoother films. However, the high sublimation rate effectively decreases diffusion processes resulting in a poorly structured surface. The result is formation of graphene domains of varying thickness. The solution is decoupling of diffusion in the surface from transport away from the surface. Utilization of ambient gas atmosphere, e.g. argon or disilanes, effectively enables simultaneous surface reconstruction and optimal graphene growth.^[100-103] In 2009 Emtsev et al. reported formation of well-defined single-layer graphene



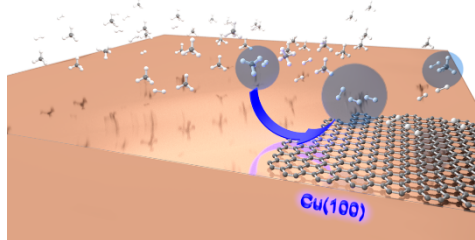
using argon gas atmosphere at 900 mbar and temperatures between 1250 and 1450 °C. The graphene films showed Hall-mobilities almost twice as high as UHV-grown graphene.

Due to their structural order graphene films prepared from 6H-SiC show high potential for electronic applications. However, some obstacles remain to resolve. Compared to suspended graphene, SiC-G shows about 100 times less electron mobility [103, 104]. The reason for this behavior is under discussion. Surface steps of SiC promote formation of two- to three-layered graphene which could be one reason for scattering. Further, the $(6\sqrt{3} \times 6\sqrt{3})R30^\circ$ layer may be the primary scattering source. While substrate quality can be further improved, the reconstruction layer is necessary for the synthesis itself thus would intrinsically limit SiC-G properties.

2.6.3 CHEMICAL VAPOR DEPOSITION OF EPITAXIAL GRAPHENE

In 1968 Morgan and Somorjai investigated the adsorption behavior of various gases to the platinum (100) surface [105]. Carbon monoxide, ethylene and acetylene show high adsorption affinity to the noble metal surface and form a c(2x2) structure. Methane and ethane gas in contrast do not adsorb. Blakely et al. investigated the segregation of carbon to Ni(100) surfaces. Temperatures below 920 °C result in surface adherent graphite structures [106]. In addition to Ni(100) modern CVD graphene synthesis is primarily conducted on copper substrates. CVD on nickel and copper results in uniform graphene layers on the surface [107].

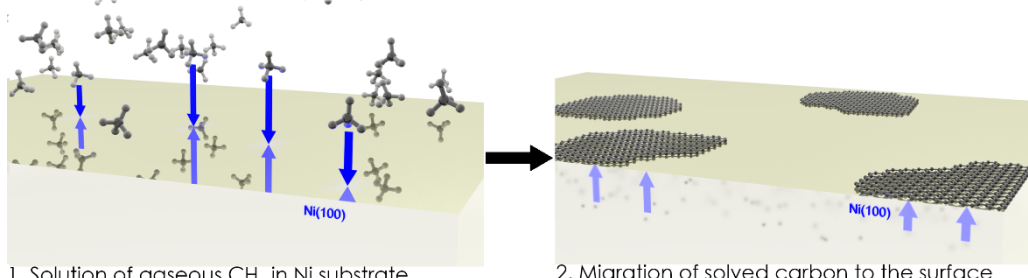
(a) CVD-G on Cu(100) substrate



Catalytic reaction between CH_4 and H_2 on Cu

- one-step process
- 1000-1050 °C
- deposition of carbon on the Cu surface
- Evolution of hydrogen

(b) CVD-G on Ni(100) substrate



1. Solution of gaseous CH_4 in Ni substrate
- 800-1100 °C

2. Migration of solved carbon to the surface
- tempering results in ordered graphene layers

Figure 2.11: Chemical vapor deposition techniques for graphene production

Chemical vapor deposition on Ni(100) substrates involves three sub steps [108-111]. The process. Pre-annealing of Ni-substrates is performed at temperatures between 800 and 1000 °C in gas atmosphere (primarily H_2 or Ar) or in vacuo. The pre-treatment increases the grain size which is essential for well-defined graphene films. Fine-grained substrates promote formation of multi-layer graphene. Graphene growth, is performed in methane-hydrogen atmosphere at 800 to 1100 °C. Reaction time varies between 5 and 100 minutes. During the process, carbon is dissolved in the nickel substrate. Following the solution phase the substrate is cooled down at rates between 0.1 and 50 °C per minute. Previously dissolved carbon migrates out of the substrates and forms a continuous graphene layer. The resulting film thickness depends on substrate quality, growth temperature and cooling rate.

Chemical vapor deposition on copper substrates results in well-defined and uniform graphene films [112-114]. The basic process resembles CVD on nickel but

differs in the underlying reaction. Carbon dissolves poorly in copper, however the catalytic decomposition activity of the noble metal towards hydrocarbons is fairly high. State of the art processes are based on catalytic decomposition of methane yielding hydrogen and surface-adsorbed carbon. Due to the low interfacial energy between copper and graphene, the resulting films can be transferred to other substrates. The graphene films show wrinkles which result from the different thermal expansion coefficients of copper and graphene.

Due to the controllable uniformity and thickness of the films, CVD synthesized graphene is mainly used for electronic applications including field effect transistors, photovoltaic cells, thin conductive films and so forth.

2.6.4 CHEMICALLY CONVERTED GRAPHENE OXIDE

2.6.4.1 GRAPHITE OXIDE

Graphite oxide synthesis is based on three major routes, Brodie's method, Hummer's method and Staudenmaier's method. Brodie used fuming nitric acid and potassium chlorate as oxidation agents to oxidize graphite^[15].

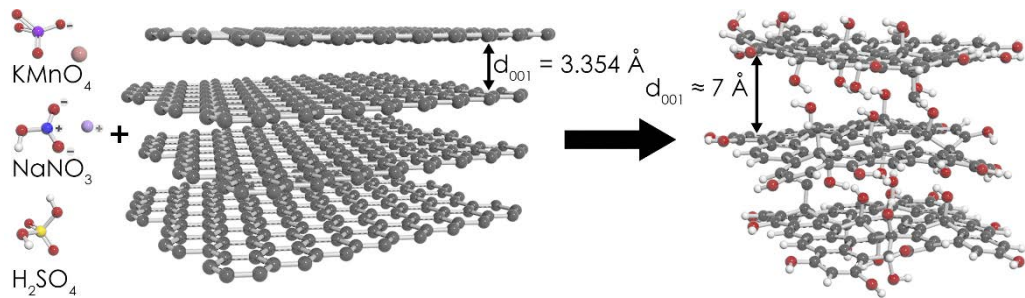


Figure 2.12: Oxidation of graphite to graphite oxide according to Hummer's method

The active species are the nitrosyl cation of nitric acid and active oxygen generated by the chlorate. The resulting graphite oxide is yellow in color which indicates a high degree of oxidation and degradation of the aromatic π -system. Graphite oxide synthesis according to Staudenmaier is performed using potassium permanganate, nitric acid and sulfuric acid ^[16]. The major difference to Brodie's method is the formation of dimanganese heptoxide (Mn_2O_7) from $KMnO_4$ and sulfuric acid. This agent selectively oxidizes unsaturated aliphatic double bonds rather than aromatic bonds. The nitric acid acts both as oxidizing agent for graphite and to restore sulfuric acid thus enables a more controlled reaction. Graphite oxide produced via Hummer's method retains a fairly high degree of the aromatic network ^[17]. The synthesis requires sulfuric acid, sodium nitrate and potassium permanganate. The reaction is similar to Staudenmaier's method. The brown to dark brown color of the graphite oxide for a partially intact π -system. Several structure proposals regarding the graphite oxide were made ^[115-117]. Lerf and Klinowski proposed that the basal planes of highly oxidized graphite oxide are covered with hydroxyl and epoxy functionalities while the edges are predominantly covered with higher oxides including carboxyl and carbonyl groups ^[118]. Hence, graphite oxide allows selective functionalization of edges and basal planes which is a highly desirable for tailoring self-organizing materials. Research on the course of the reaction revealed that hydroxyl functionalities are formed in the early stages of the reaction while carbonyl and carboxyl groups form in the later stages of the reaction ^[119, 120]. This allows a limited control over the product. However, the nature of the final product still depends on graphite source and the specific reaction parameters.

2.6.4.2 GRAPHENE OXIDE

Due to its high hydrophilicity graphite oxide is easily dispersed in water and polar organic solvents yielding single layer graphene oxide. Aqueous graphene oxide dispersions offer ecological advantages over solvent-borne systems. Exfoliation is predominantly performed via ultrasonic treatment and, to minor extent, via thermal exfoliation between 300 and 500 °C [121]. Ultrasonic exfoliation is typically preferred since graphene oxide is thermally unstable. The resulting yellow to brown colored dispersions exhibit concentrations up to 7 mg/ml [122]. The concentration threshold depends on the average flake diameter and the degree of oxidation. Both diameter and degree of oxidation depend on individual educt – and process-related parameters including graphite source, oxidation method and duration of oxidation. Due to this huge set of parameters there is no precise definition of graphite oxide and graphene oxide. The more or less high degree of oxidation renders graphene oxide electrically insulating. Despite the partially corrupted carbon network Young's moduli of GO sheets range between 290 and 470 GPa [123-125]. The values are highly sensitive to degree of oxidation and decrease monotonically with increasing sp^3 to sp^2 carbon ratio and OH/O ratio. In conjunction with the high functionality the mechanical stability makes graphene oxide an ideal material for processing of polymer nanocomposites. Polymer matrices include epoxy resins, polyurethanes, polyamides, polyimides, poly(methyl methacrylate), poly(lactic acid), poly(vinyl alcohol) and various others (table 2.3). Depending on the polymer matrix graphene oxide has to be chemically modified to enable cross-linking reactions. Incorporation of GO usually results in enhanced mechanical properties. Mechanical properties GO polymer composites are limited by a concentration threshold beyond which the properties of the compound start to decrease. This value is highly dependent on the distinct nature of the used GO. Average thresholds range between 0.1 and 1 wt%.

Table 2.3: Graphene oxide - polymer composites; Abbr.: APTES: (3-Aminopropyl)triethoxysilane, GPTES: (Glycidyloxypropyl)triethoxysilane, PI: Polyimide, PVA: Poly(vinylalcohol), PLA: Poly(lactic acid), PMMA: Poly(methyl methacrylate)

Matrix	GO functionalization	Comments	Ref.
Epoxy	n/a	Tensile modulus increased by 12 % Flexural strength increased by 23 %	[126]
	APTES/GPTES	Young's modulus increased by 32 % Tensile strength increased by 16 %	[127]
PI	n/a	In situ polymerization Modulus increased by 25 %	[128]
PUR	2-(methacryloyloxy)-ethyl-phosphorychloride	Tensile strength increased by up to 75.4% Modulus increased by up to 31 %	[129]
PVA	PVA, grafted	Tensile strength increased by up to 88 % Modulus increased by up to 150%	[130]
PLA	PLA, grafted	Flexural strength increased by 114.3 % Tensile strength increased by 105.7 %	[131]
PMMA	n/a	Modulus increased by 20 %	[132]

Above the threshold GO re-agglomerates. In close accordance to pristine graphene polymer composites, re-agglomeration causes decrease of GO-matrix interface and introduction of slipping planes. Results have to be discussed individually since graphene oxide source, synthesis method, and functionalization are very diverse. The basic mechanical properties of the polymer matrices have to be considered as well.

Graphene oxide holds far more potential than polymer reinforcement ^[133]. The amphiphilic character enables graphene oxide to act as dispersing agent for other carbon materials. Examples include graphite, carbon nanotubes and various π -conjugated materials like organic semiconductors and conducting polymers ^[134]. Whether GO may be a suitable candidate for synthesis of aqueous graphene dispersions was discussed as well. Another intriguing topic are graphene oxide liquid crystal phases. Liquid crystalline phenomena depend on particle diameter and concentration. Xu and Gao reported nematic phases consisting of 2.1 μm large flakes at concentrations above 5 mg/ml. The isotropic-nematic phase transition occurred at concentration as low as 0.25 mg/ml ^[135].

2.6.4.3 REDUCED GRAPHENE OXIDE

Reduction of graphene oxide yields reduced graphene oxide (rGO). rGO closely resembles pristine graphene. However, complete removal of oxide functionalities remains a challenge. Further rGO sheets are likely to possess crystal defects which originate from the oxidation process as well [136, 137]. The key advantage of rGO over other graphene samples is the possible functionalization prior to reduction. Chemical functionalization opens up a huge scope for conductive polymer-nanocomposites, supercapacitors and other graphene related applications [154-156]. Reduction of graphene oxide is performed via several methods including chemical reduction, thermal reduction, electrochemical reduction, photothermal [138] and photochemical [139, 140] reduction (figure 2.13). Chemical reduction methods mainly rely on hydrazine and sodium boron hydride. Hydrazine monohydrate and hydrazine derivatives are effective reduction agents and can be used in aqueous media. Side reaction yielding C-N bonds cannot be excluded. Resulting rGO partially aggregates to graphitic structures owing to the fact that around 94% of oxygen moieties are eliminated. Re-aggregation is usually prevented by adding polymeric stabilizers, either by covalent functionalization of the graphene oxide precursor or via non-covalent functionalization [14, 141-143]. Sodium boron hydride is a powerful reduction agent resulting in highly conductive rGO sheets. In contrast to hydrazine the reaction does not yield C-N bonds as unwanted byproduct [143]. Further reduction agents include hydroxylamine, sodium hydrosulfite, p-phenylene diamine and aluminum/hydrochloric acid [144-147]. Ecologically advantageous approaches were taken using e.g. L-ascorbic acid, alcohol vapors, L-cystein and L-glutathione [148-151]. Depending on the desired application every reduction agent presents specific advantages and disadvantages. Thermal reduction is a very effective reduction method for graphene oxide [152, 153].

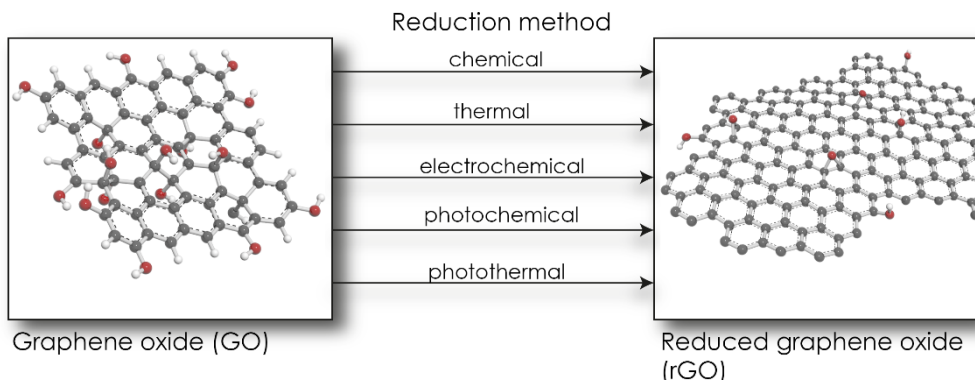


Figure 2.13: Reduction methods leading to reduced graphene oxide

In this process the sample is heated to temperatures between 450 and 1100 °C in argon or hydrogen atmosphere. Under these conditions oxide moieties are removed in form of carbon monoxide, carbon dioxide and water. Reduction performance increases with increasing temperature. The reaction proceeds via a radical mechanism consisting of several substeps. The resulting graphene sheets exhibit high mechanical stability and electric conductivity. The major disadvantage of this method is the partial destruction of the rGO sheets which limits the maximum reduction temperature. The importance of electrochemical reduction manifests itself in the production of electrochemically reduced graphene oxide thin films. Electrodeposition of graphene is a versatile tool for production of transparent conductive films, supercapacitors and so forth (chapter 2.4). During the deposition process the negatively charged graphene oxide migrates to the anode (Cu, Ni, Al, stainless steel, p-type Si), is reduced and forms a dense film of rGO. The reduction efficiency is inferior to chemical and thermal reduction. Higher reduction efficiency was achieved by extended cyclic voltammetry. The resulting rGO shows superior electrical properties compared to chemical reduction.

2.6.5 PRISTINE GRAPHENE DISPERSIONS

2.6.5.1 SOLVENT-BORNE GRAPHENE DISPERSIONS

Ultrasonic exfoliation of graphite can be performed in a variety of solvents including N-methyl pyrrolidone (NMP), N,N-dimethyl acetamide (DMA), γ-butyrolactone (GBA) and 1,3-dimethyl-2-imidazolidone (DMEU)^[157, 158]

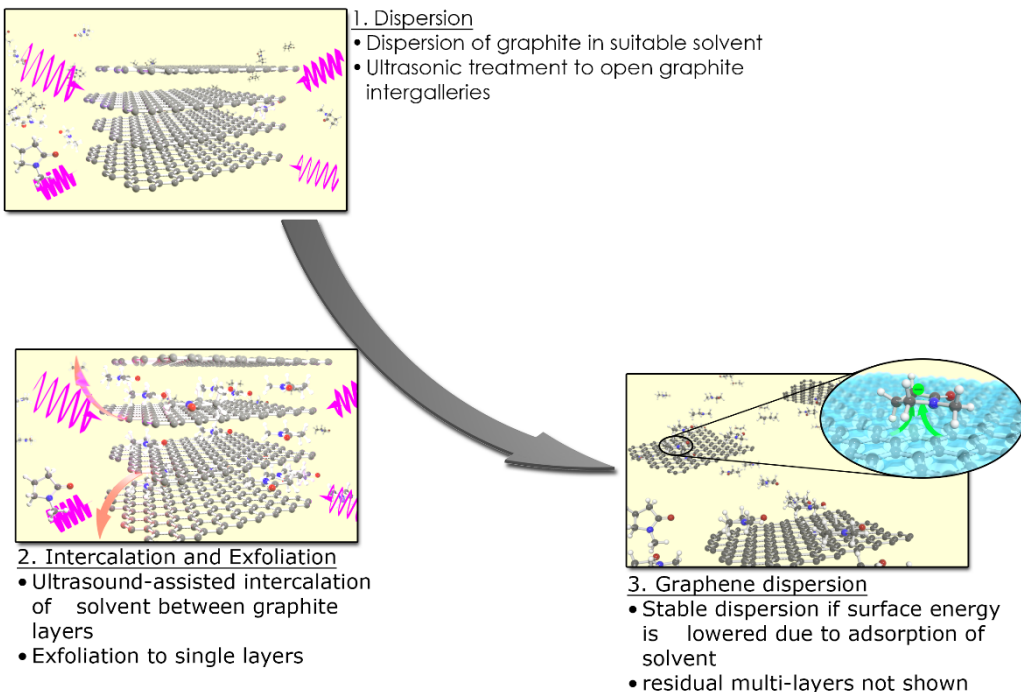


Figure 2.14: Ultrasound-assisted exfoliation of graphite in organic solvents to single layer graphene dispersions; pictures relate to exfoliation in NMP; inset depicts charge-transfer between graphene and NMP accounting for measured negative zeta potentials

The resulting graphene dispersions contain high-quality single layer and multi-layer graphene in concentrations up to 0.01 mg/ml. Thermodynamical studies revealed that successful exfoliation and simultaneous prevention of re-agglomeration depends on solvent surface energies. Literature values of graphite surface energies range between 55 and 90 mJ/m² and are a direct measure of the interlayer forces between stacked sheets. Use of solvents with surface energies

between 35 mJm^{-2} and 46 mJm^{-2} yields the best results regarding degree of exfoliation and concentration.

Khan et al. published two consecutive papers on graphene dispersions based on NMP [159, 160]. Threshold concentrations amount to 1 mg/ml after 460 hours of exfoliation. Modifications of the process increase the yield up to 26-38 mg/ml. Barwick et al. proposed an ultrasonic pre-treatment in water or NMP for several hours to overcome the extreme time required to reach the threshold concentration [161]. The resulting graphite powders showed low structural ordering and could easily be redispersed in NMP. The pre-treated powders allow fast ultrasonic processing (one minute) which yields graphene dispersions in concentrations around 1 mg/ml. The dispersions' stability depends on charge-transfer interactions [162]. Several solvent-borne dispersions have been investigated with regard to zeta potential. Graphene in NMP shows a negative zeta potential around -40 mV which alone would be sufficient to yield stable dispersions. A comparative calculation of the LUMO and HOMO energies of NMP yields values of -1.86 eV and -6.8 eV respectively⁷. The values provide evidence for charge-transfer between graphene acting as donor and NMP acting as acceptor. Graphene in NMP dispersions are suitable for several applications including conductive and reinforced polymer composite films. However, due to the high boiling point of the solvent and the strong intermolecular interaction, around 7 % NMP reside even in dried powder. In addition to high-boiling solvents, low boiling solvents were successfully utilized to yield stable graphene dispersions [163]. Based on the thermodynamic requirements described above several solvents were identified as suitable dispersing agents for graphene. O'Neill et al. investigated the dispersing capabilities of acetone, chloroform and isopropanol. These solvents show good dispersing properties yielding

⁷ Calculations were performed using the DMol3 package, B3LYP functional with TS DFT-D correction, DNP+ basis set; solvation model: COSMO, $\epsilon = 32.2$ (NMP)

dispersions with concentrations up to 0.5 mg/ml. Due to the low boiling point these dispersions can be processed via spray-application.

2.6.5.2 AQUEOUS GRAPHENE DISPERSIONS

Aqueous graphene dispersions combine the advantages of solvent-borne dispersions with ecological benefits. Due to the hydrophobicity of graphite, stabilizers have to be employed to prevent immediate re-agglomeration. Exfoliation is conducted via ultrasonic treatment. Common dispersing agents include surfactants and low molecular weight polymers. Guardia et al. investigated the stabilization capabilities of several ionic and non-ionic surfactants ^[164]. Comparably high graphite concentrations (100 g/L) were used to increase the overall graphene yield. Depending on the specific surfactant there is an upper threshold above which graphene yield decreases. Best results were obtained using the non-ionic surfactants Tween 80 (Polyoxyethylen(20)-sorbitan-monooleate) and Pluronic® P123 (Triblock copolymer, HO(CH₂CH₂O)₂₀(CH₂CH(CH₃)O)₇₀-(CH₂CH₂O)₂₀H). The results indicate that entropic stabilization is the dominant mechanism. Further information about the interaction mechanism was not provided. Further they pointed out that all investigated surfactants were used above their critical micelle concentration. There is no explanations why some dispersants exhibit graphene concentration thresholds and others did not. The effectiveness of stabilizing depends on various interaction mechanisms. Ionic- π interactions and π -stacking interactions are frequently encountered

Table 2.4: Aqueous Graphene Dispersions

Stabilizer	c _{Graphene} , max [mg/ml]	Average dimensions (height/diameter)	Interaction mechanism	Ref.
2, 3, 6, 7, 10, 11-hexakis(10-carboxydecyloxy) triphenylene	0.56	h = 2.5 nm d = 800 nm	π-stacking	[165]
Pluronic® P123	0.90	h = 1 - 3 nm d = 50 - 600 nm	n/a	[166]
Sodium-1-pyrenesulfonate	1	h = 2 - 4 graphene layers d = 2 - 2.8 μm	π-stacking	[167]
CTAB	n/a	h = 1.18 nm d = 1 - 2 μm	Cation-π	[168]
SDBS	0.05	h = 1 - 1.5 nm d = 150 - 1000 nm	n/a	[169]
Cellulose Nanocrystals (CNC)	1.08	h = 0.9 nm d = several hundred nm	n/a	[170]
Polyvinylpyrrolidone	0.1	h = 0.7 - 0.9 nm d = up to several μm	n/a	[171]
TCNQ	0.02	h = 2 - 3 layers d = several hundred nm	π-stacking	[172]

Pyrene derivatives yield highly concentrated aqueous graphene dispersions [167]. The resulting concentration strongly depends on the attached functional group which renders the pyrene group either electron-rich or electron-accepting. Apart from classical stabilizing agents, Carrasco et al. were able to produce aqueous graphene dispersions using cellulose nanocrystals [170]. The resulting graphene sheets possessed very large diameter/height aspect ratios. However, the results are inconclusive to some extent. The large dimensioned CNC (199 nm in diameter, 11 nm in height) did not show up in the presented AFM and TEM images. Hence, close adherence between CNC and the graphene surface has to be excluded. Further, the authors deduced electrostatic stabilization due to sulfate groups inherent to CNC. The actual stabilization mechanism more likely relies on CNC protective colloids.

The limited research on aqueous graphene dispersions reflects the difficulties encountered in finding suitable dispersing agents for graphene. The low chemical versatility of the material itself limits the possible candidates. Aqueous graphene dispersions preserve the physical and chemical properties of the carbon

material. Hence, further research has to be conducted to further establish this field in scientific and especially industrial research.

2.7 INTERACTION MECHANISMS IN GRAPHENE COMPOSITE SCIENCE

2.7.1 π -STACKING INTERACTIONS

Due to weak interactions between aromatic systems, porphyrine solutions aggregate with time [174, 175]. Computational and experimental studies provide evidence for offset stacking of the aromatic systems [193, 176]. The aromatic molecules are described by a quadrupole moment, hence the face-to-face stacking (FTF) of aromatic systems leads to a repulsive force between the perpendicular π -systems. One way to circumvent this unfavorable situation leads to face-to-edge (FTE) geometries. FTE stacking has indeed been observed in several systems including the well-studied benzene dimer. Face-to-face stacking results in an energetically equally favorable configuration. The offset stacking of two molecules results in interaction between the partial negative charge of one π -system with the partial positive charge of the respective other σ -backbone. The repulsive force between the π -electrons, also known as π - π interaction is minimized in FTE and FTF configurations. In parts of scientific literature the term π - π interaction is mistakenly used as the driving force for graphene-adsorbate interactions. On the contrary, π - π interactions are responsible for repulsion between aromatic systems while π - σ cause attraction between them. The interaction energy can be altered by electron-withdrawing or pushing substituents. However, it was argued that the interaction between the substituents themselves and the aromatic surface are usually more dominant than the electron-withdrawing or -donating character [177]. In the same study it was concluded that the term aromatic π -stacking is a misconception as the interaction does not necessarily require aromaticity.

2.7.2 ION-Π INTERACTIONS

Anion- π and especially cation- π interactions play an important role in graphene science. Both types are frequently encountered in graphene doping experiments and modified graphene dispersions. In contrast to π -stacking interactions, ion- π interactions occur between the π -system of an aromatic molecule and either negatively or positively charged ions or molecules. Based on the quadrupole picture, electron-poor aromatics tend to interact with anions while electron-rich interact primarily with cations. Results of these interactions include facilitated electron-transfer from one to the other, hence CT. As for graphene the resulting chemical doping may be advantageous for electronic applications. Pristine graphene is an electron-rich aromatic system, hence cation- π interactions are observed frequently. Anion- π interactions are primarily observed in back-gate tuned graphene. A suitable back-gate voltage causes decrease of electron charge carriers thereby rendering graphene electron-poor. This effect is made use of in single-molecule gas adsorption measurements.

2.7.3 CHARGE-TRANSFER INTERACTIONS

Charge-transfer are frequently encountered in graphene composites. Whether the effect is the actual driving force for the total interaction or a mere consequence of aromatic and/or ionic interactions is still under discussion. Charge-transfer complexation occurs if the LUMO of an acceptor molecule is energetically lower than the HOMO of the donor. If so, electrons are shifted from one molecule to the other rendering the donor positively charged and the acceptor negatively charged. A different description is based on donor- and acceptor numbers (DN, AN). The concept was first introduced by Gutman in 1976 [178, 179]. Although

these numbers were defined for a specific purpose⁸ there is close correlation to the density of states picture. CT interactions are desirable processes in graphene composites. Depending on the respective adsorbate, the underlying graphene sheet is rendered either n-doped or p-doped. The effect can thereby decrease the electrical resistivity of the system. Evidence for CT complexation can be derived from Raman and UV-VIS spectra. The Raman G and G' band of graphene are highly susceptible to changes in the electronic nature of the graphene π -system. Hence, both p- and n-doping results in shifting of these peaks (cp. chapter 2.5.1). Charge-transfer further results in characteristic features in UV-VIS spectra. Due to the interaction the specific bands show a bathochromic effect. The magnitude of the effect strongly depends on donor- and acceptor properties. Further, several spectra show high-intensity charge-transfer bands associated with $S_0 \rightarrow S_1$ transitions.

⁸ DN: “[...] negative value of ΔH for the interaction of the electron pair donor solvent with $SbCl_5$ in a very dilute solution of 1,2-dichloroethane.” [173]

DN: “[...] $\Delta N = 100$ the normalized NMR chemical shift of ^{31}P in the adduct of $SbCl_5$ with triethylphosphine oxide dissolved in 1,2-dichloroethane.” [173]

2.8 GRAPHENE THIN FILMS

2.8.1 LAYER-BY-LAYER ASSEMBLY OF FUNCTIONAL GRAPHENE (LBL)

Layer-by-layer assembly (LBL) is a versatile technique for manufacture of graphene thin-films. LBL allows close control over layer thickness and morphology. In contrast to Langmuir-Blodgett (LB) and electrodeposited (ED) films the method requires two species of opposite charge. Graphene oxide and reduced graphene oxide possess negative surface charge. Hence, GO and rGO are often used without further modification. Positive charge is commonly introduced by amine-functionalization. However, depending on the desired application of the final films several other types of functionalization are in use. LBL assembly using pristine graphene dispersions generally requires chemical modification to induce surface charge. Film assembly is either conducted as homo-assembly using two types of charged graphene sheets or as hetero-assembly using charged graphene sheets and a variety of oppositely charged particles. The main applications of LBL films include TCFs, supercapacitors and biosensing. Table 2.5 provides an overview. LBL assembly of aqueous rGO dispersions offers a high degree of versatility. Prior to reduction, graphene oxide is modified with the desired functional species. Hong et al. utilized layer-by-layer assembly of polyallylamine and poly(styrene-sulfonate) to synthesize graphene layers [192]. Following the deposition, the LBL film is annealed at temperatures around 1000 °C which results in uniform graphene sheets. Metallic dopants enhance the process as they have shown to catalyze graphitization reactions. The resulting graphene flakes were several hundred nanometers in diameter and showed very low sheet resistance around $10^{-6} \Omega/\text{sq}$. The final film thickness is determined by the LBL film thickness, hence can be controlled accurately. LBL is mainly based on dip-coating. The duration of the process

depends on several parameters including the structure and charge of the dispersed particles and the surface charge of the respective substrate.

Table 2.5: Published layer-by-layer assemblies of graphene

+ species	- species	Substrate	Application/Goals	Ref.
Graphene/Polyelectrolyte-functionalized ionic liquid	Prussian Blue nano particles	n/a	H ₂ O ₂ detection via EC-SPR	[180]
Graphene/Polyallylamine hydrochloride	CdS quantum dots	FTO	n/a	[181]
rGO/Ethylenediamine	rGO	Quartz	TCFs	[182]
rGO/Ethylenediamine	rGO	Quartz, Si	OLED	[183]
QP4VP-co-PCN (Azo-polyelectrolyte)	rGO	Quartz, ITO	EDLC	[184]
Polyvinyl alcohol	rGO	Quartz	Comparison LBL/VAF	[185]
Graphene/pyr-PDMAEA	Graphene/pyr-PAA	ITO	pH sensitive phase behavior	[186]
Graphene/PAAm	Graphene/PAA	Quartz	Film morphology control	[187]
PEI	rGO/pyr-PAA	Quartz	Enzyme-based glucose and maltose sensing	[188]
Graphene/IS-IL	Pt nanoparticles	ITO	Electrocatalytic oxygen reduction	[189]
PANI	rGO/sulfonic acid	ITO	Flexible transparent electrodes	[190]
CdSE nanoparticles	rGO/pyr-PAA	ITO	Photoelectrochemical biosensors	[191]

The required duration to achieve deposition saturation can be determined via quartz crystal microbalance. Liu et al. found that twenty minutes is sufficient for graphene systems to yield densely packed films [193]. However, this value is highly dependent on the actual system. Optimum deposition time has to be determined individually for a given set of parameters. The majority of literature values range between 5 and 30 minutes. The relatively high deposition time of the dip process stands in close relation to the underlying transport processes. The transport of particles from the bulk dispersion to the substrate is subdivided into three regions. Since the electrostatic attraction between the surface and the particles is very short ranged, motion of particles in the bulk phase away from the surface is exclusively determined by diffusive transport and electrostatic repulsion between particles. In vicinity to the substrate, these mechanisms are

superimposed by electrostatic attraction. The third region begins in direct vicinity to the substrate.

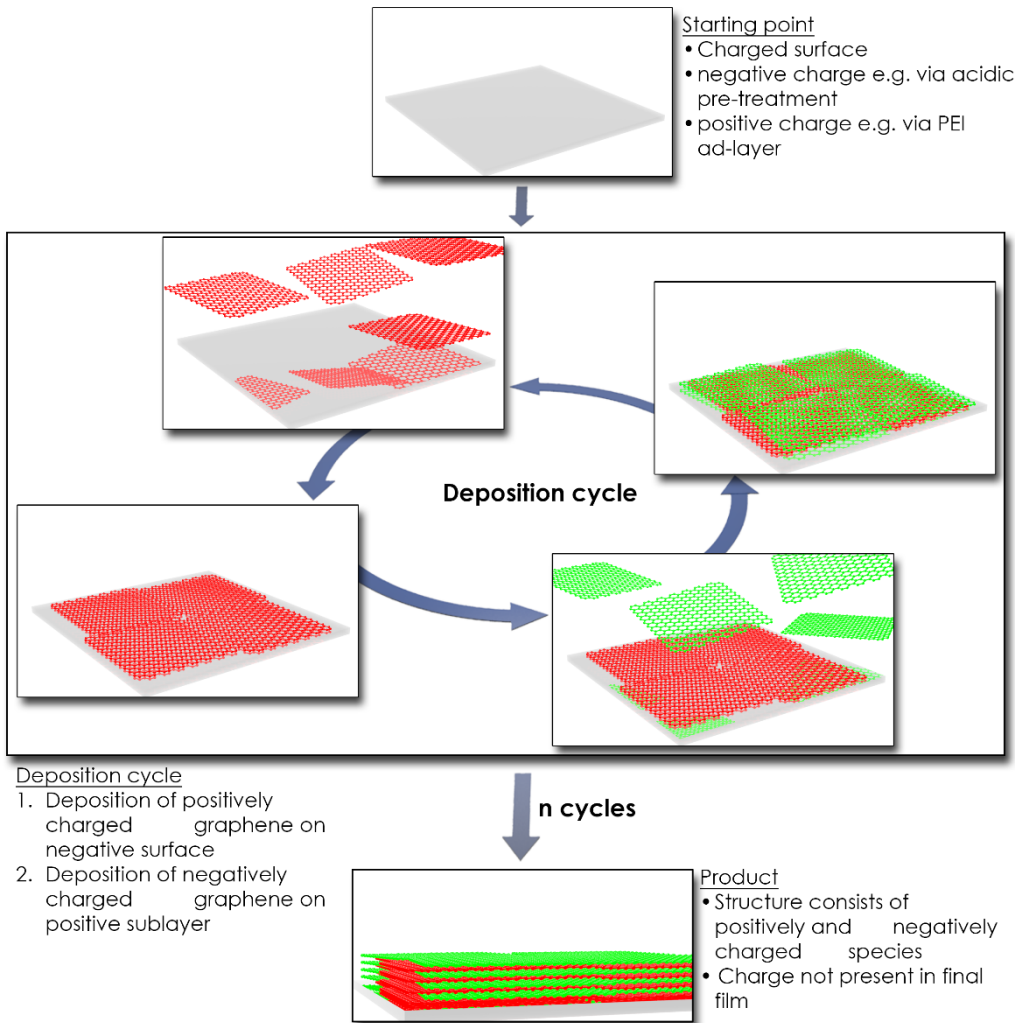


Figure 2.15: Layer-by-layer assembly of positively (red) and negatively (green) charged graphene sheets

Due to charge compensation this diffusion or depletion layer is governed by diffusive transport only. The depletion layer thickness is the primary influence on the overall process duration. Apart from the dip-coating process, Mulhearn et al. investigated LBL assembly of silica nanoparticles using spray application [194]. Spray application has several advantages over dip deposition

including avoidance of cross-contamination and significantly lower process durations. In contrast to dip deposition, all diffusive processes are now at least partially replaced by convective transport. Despite the shorter deposition time, the resulting films showed comparable or even higher quality. There are no studies about spray applied graphene LBL films. LBL offers several advantages over other processes including close control over film thickness, easy multi-component assembly and the wide choice of substrates. On the other hand, due to the high set of parameters there is no exact guideline on deposition conditions. Factors like dispersion pH, substrate charge and deposition time have to be optimized for each LBL experiment.

2.8.2 ELECTRODEPOSITION OF FUNCTIONALIZED GRAPHENE (ED)

Electrodeposition (ED) is an efficient method for graphene thin film production. Compared to LB and LBL films, the method is very fast and less susceptible to dispersion impurities. Graphene-based ED films can be obtained from graphene oxide, reduced graphene oxide and functionalized pristine graphene. ED film thickness depends on several parameters including deposition time, deposition voltage, dispersion conductivity and the experimental setup.

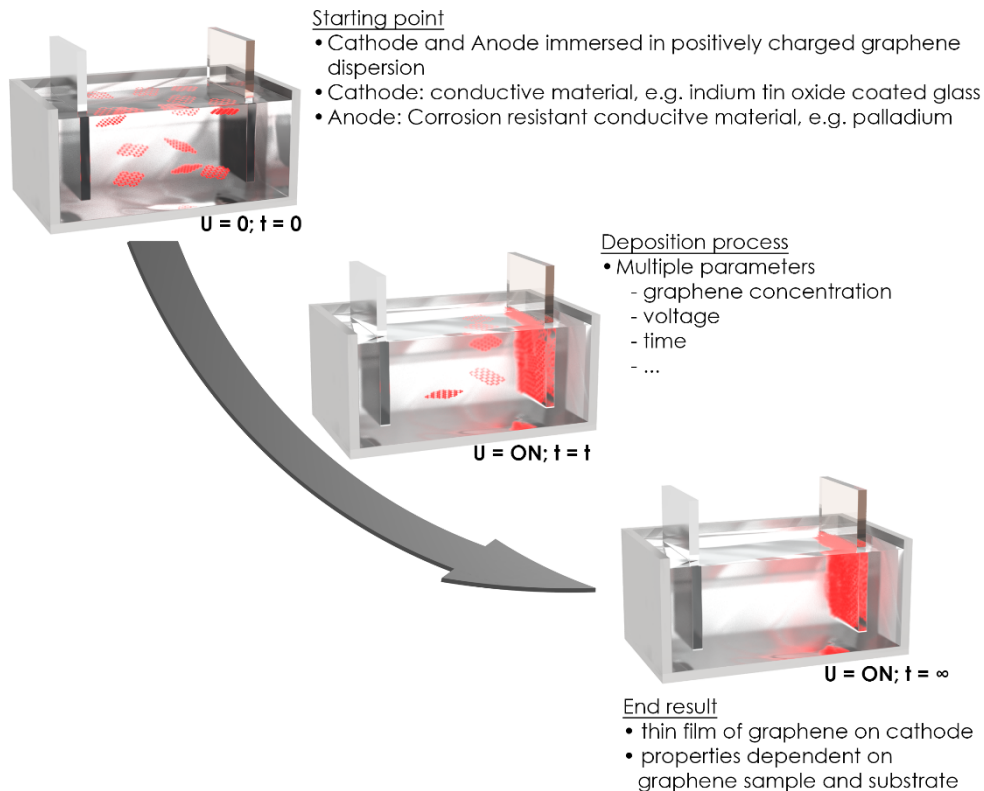


Figure 2.16: Process illustration of C-ED of charged graphene dispersions

Electrodeposition consists of two mechanisms, electrophoresis and electroosmosis. Electrophoresis dominates the process in the bulk dispersion while electroosmosis occurs in immediate vicinity to the substrate. During electrophoresis an external electric field exerts an electric force on a charged particle in the bulk phase. The particle is drawn to the oppositely charged

electrode. The diffuse layer surrounding this particle exerts a retardation force in the opposite direction. The frictional force points in the same direction as the retardation force. The process is commonly described by the electrophoretic mobility.

$$u_E = \frac{V_E}{E} = \frac{2\epsilon\zeta}{3\eta} \cdot f(\kappa a) \quad (2.21)$$

Equation 2.21 was originally proposed by Henry ^[195] and is based on the work of Hückel and Smoluchowski ^[196, 197]. The mobility of a charge particle depends on its zeta potential, the dielectric constant and viscosity of the medium and the Henry factor $f(\kappa a)$. The Henry factor depends on the Debye length of the electric double layer κ . In aqueous media, where $\kappa \ll a$ this factor approximately 1.5 whereas in common organic solvents, where $\kappa \gg a$ it approximates 1. O'Brian and White concentrated on the complex transient range between the two extreme values ^[198, 199].

Electroosmosis describes the movement of liquid relative to a stationary charge. Electroosmosis primarily affects the structure and morphology of ED films and accounts for two processes. The first process is solvent removal from the deposited film. The deposited particles' counter ions are forced away from the substrate and drag solvent molecules with them. The motion of solvent molecules within the film also occurs towards the substrate. This second process influences aggregation or separation of deposited particles. Direction and magnitude of the motion depend on particle zeta potential and direction of the electric field in the bulk dispersion. Modeling of these processes is based on the Navier-Stokes equation, the continuity equation for laminar fluid flow and Laplace's equation. A simplified approximation to the problem was proposed by Helmholtz and Smoluchowski for an electric field perpendicular to the electrode.

$$v_x = -\frac{\epsilon_0 \epsilon \zeta}{\eta} E_x \quad (2.22)$$

Several models of varying sophistication have been proposed for estimating the kinetics of ED. The earliest model was proposed by Hamaker in 1930 (equation 2.23) and is applicable for very short deposition time. The Hamaker equation does not consider non-linear effects [200]. The deposited mass depends on the concentration of suspended particles (c_s), the electrophoretic mobility (μ), the electrode surface area (S), the electric field strength (E) and the deposition time.

$$\frac{dm}{dt} = f \cdot c_s \cdot \mu \cdot S \cdot E \quad (2.23)$$

The “sticking” parameter f describes how much of the deposited material remains deposited and does not diffuse out of the film. As a rule of thumb, f becomes 1 if the zeta potential of the dispersed particles is fairly high ($\zeta \geq 20$ mV). Several other kinetic models have been proposed to include non-linear effects like e.g. decreasing concentration of suspended particles with time, highly concentrated suspensions and variation of electric field with time. González-Cuenca et al. developed a model for plate-plate geometry for constant voltage deposition [201]. The model includes decreasing particle concentration during the deposition. However, diffusion processes and local changes in the electric field as well as changes in particle charge near the respective electrode are neglected. Accordingly, the growth rate is a function of particle velocity and volumetric fractions of particles in suspension and in the deposit.

$$\frac{d\delta}{dt} = -V_s \frac{\phi_s}{\phi_d - \phi_s} \quad (2.24)$$

The solution of the differential equation and implying dilute suspensions ($f_d \gg f_s$) yields an expression of the film thickness as function of time [203].

$$\delta = \frac{C_{s,0} V}{S \cdot C_d} \left(1 - e^{-\frac{f_d \mu S E}{V} t} \right) \quad (2.25)$$

There is no general model for describing electrodeposition. Deviations from linear behavior have to be discussed separately.

Anodic electrodeposition is mainly conducted using graphene oxide and reduced graphene oxide (table 2.6). A-ED of aqueous dispersions requires corrosion-resistant substrates like stainless steel or noble metals. Insulating substrates such as glass can be coated by attaching a suitable back-electrode^[202]. However, the thick insulating layer requires a high deposition voltage which accelerates water electrolysis as well. Deposition of pristine graphene dispersions is mainly conducted by cathodic electrodeposition (C-ED). The required positive charge is introduced, e.g. by adsorption of metal ions or cationic molecules (table 2.7).

Table 2.6: Graphene thin films by anodic electrodeposition

Graphene type	Substrate	Deposition conditions		Suspension medium	Film properties	Application	Ref.
		U [V]	t				
rGO	FTO	3	60 s	Water	n/a	DSSC	[204]
rGO	SS	3	15 min	Water	$\sigma = 5.51 \cdot 10^5 \text{ Sm}^{-1}$	Electrical Devices	[205]
GO	SS	10	1-10 min	Water	$\sigma = 1.43 \cdot 10^4 \text{ Sm}^{-1}$	In-situ reduction to TCFs	[206]
Graphene/CNT	ITO/PET	1-5	30 s	NMP	$R_s = 330 \Omega \text{sq}^{-1}$	TCFs	[207]

Table 2.7: Graphene thin films by cathodic electrodeposition

Graphene type	Substrate	Deposition conditions		Suspension medium	Film properties	Application	Ref.
		U [V]	t				
GO/Al(NO ₃) ₃	n++ Si	20	5-15 min	Ethanol	$E_{on} = 7.2 \text{ V} \mu\text{m}^{-1}$ @ 100nA · cm ⁻²	FET	[208]
Graphene / Bronsted acids	PEDOT	-1.2 (CV)	10 min	Acetonitrile	$C_s = 109.4 \text{ Fg}^{-1}$ (HCl)	TCFs	[209]
Graphene / CTAB	Au/Glass	6	1-10 min	Water	$\sigma = 1 \cdot 10^5 \text{ Sm}^{-1}$	TCFs	[210]
Graphene / methyl violet	SS	20-50	2 min	Water	$C_s = 130 \text{ Fg}^{-1}$	EC SCs	[211]
Graphene / Mg(NO ₃) ₂	ITO/Glass	100-160	1 min	Isopropanol	$E_{on} = 2.3 \text{ V} \mu\text{m}^{-1}$ @ 10 μA · cm ⁻²	FET	[212]

2.8 HEXAMETHOXYMETHYL MELAMINE – PROPERTIES AND APPLICATIONS

This chapter introduces the triazine derivative N,N,N',N',N'',N'' -hexa(methoxymethyl)-2,4,6-triamino-1,3,5-triazine, also known as hexamethoxy-methyl melamine or HMMM (figure 2.17).

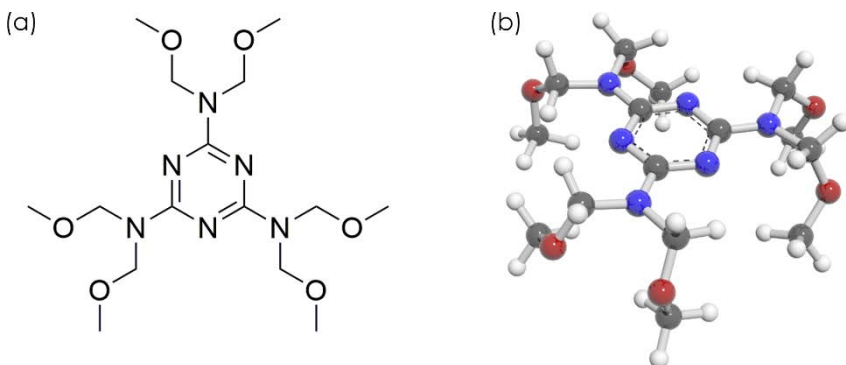


Figure 2.17: (a) Lewis formula of HMMM and (b) 3D model of HMMM; 3D model adopted from calculated structure

HMMM is widely used as a cross-linking agent in polymer science. Polyesters, alkyd resins, acrylates and urethanes comprise the majority of co-reacted polymers [219-224]. Applications include automotive, coil and intumescent coatings as well as lithographic resists.

HMMM is highly reactive and self-condenses to a certain degree. Commercial resins contain high amounts of condensates. Chromatographic studies revealed amounts of 23% dimers and 15% trimers and higher oligomers [225]. Confocal Raman microscopy studies on polyester-HMMM systems further indicated that the self-condensation causes significant amounts of cluster formation in the final coating [226, 227]. The considerable impact of the reaction on the final coating performance resulted in several studies of the mechanistic and kinetic details of both co- and self-condensation [228-232]. The acid catalyzed condensation is based on a unimolecular nucleophilic substitution (SN_1) mechanism. Details on the mechanism were provided by time-resolved FTIR and NMR studies. The latter

showed that cationic intermediates are formed during the reaction. The mechanism and kinetics of the self-condensation are complex. The rate of self-condensation in aqueous environment strongly depends on proton and HMMM concentration. HMMM rapidly self-condenses to colloidal agglomerates at acidic pH ≥ 1.22 . The high stability at pH values below 1.22 results from protonation of the triazine ring. This deactivates the available methoxy groups. The resulting dimethylene ether bridge between either one HMMM and a polyol or two HMMM is able to form hydrogen bridges to adjacent methoxy groups thereby activating them for further condensation. This behavior has major impact on the resulting structure of the self-condensed HMMM since it favors double-dimethylene ether bridges between two HMMM molecules.

Controlled self-condensation provides the basis for synthesis of aqueous nano particle dispersions (MP) [233]. The positively charged particles with zeta potentials around +20 mV exhibit hydrodynamic diameters around 100 nm. Introduction of MP into polymeric systems has major impact on the mechanical properties. Hardness is increased while elasticity of the films is retained. MP dispersions are not stable in basic environment.

Available data on HMMM relates to macroscopic rather than microscopic properties (table 2.9). The molecule consists of an aromatic 1,3,5-triazine ring with three dimethoxymethyl-amino groups attached to the carbon ring atoms. The electron withdrawing character of the functional groups renders the aromatic ring partially electron deficient. In aqueous environment HMMM reacts basic. The actual site of protonation depends on the pH value. In comparison to the methoxy groups, protonation of ring nitrogen occurs at considerably lower pH values [232].

Table 2.8: Macroscopic physical properties of hexamethoxymethyl melamine resins^[234]

Property	Value
Melting Point	28-33 °C
Boiling Point	448.20 °C
Vapor Pressure	$1.06 \cdot 10^{-8}$ mm Hg (25 °C)
Partition coefficient	Log(Kow) = 1.61
Water solubility	69.5 g/L (20 °C)
Photodegradation	Reaction with OH radical; $k = 323.5521 \cdot 10^{-12}$ cm ³ /N·s
Hydrolysis	pH 4, 25 °C: 3.3 h pH 7, 25 °C: 67 d pH 9, 25 °C: > 365d

Data on the molecular or crystal structure of HMMM is not available. The functionalization of the triazine ring results in non-equivalent bond lengths and varying angles throughout the aromatic center and the adjacent substituents. The resulting space group is C₁. Crystal structure data of other triazine derivatives is available and can be used to correlate HMMM X-ray diffraction data.

Table 2.9: Crystallographic data of selected triazine compounds

Substance	Monomer structure	Space group	Unit cell constants	Ref.
2,4,6-Triamino-1,3,5-triazine		P2 ₁ /a (monoclinic) N = 4	a = 10.606 b = 7.495 c = 7.295 β = 112.26°	[235]
2,4,6-Triamino-1,3,5-triazine (under high pressure)		P-1 (triclinic) N = 2	a = 6.94 b = 6.47 c = 9.84 α = 99.52° β = 91.07° γ = 111.12°	[236]
2,4,6-Trimethoxy-1,3,5-triazine		Pnma (orthorhombic) N = 5	a = 8.474 b = 6.719 c = 14.409	[237]
2,4,6-Tris(3,5-dimethyl-1H-pyrazol-1-yl)-1,3,5-triazine		Pna2 ₁ (orthorhombic) N = 4	a = 7.1840 b = 12.5079 c = 19.9527	[238]

2.9 EMULSIONS AND MICROEMULSIONS

Emulsions and microemulsions are binary phases consisting of two immiscible fluids. Common examples for emulsions are oil in water (O/W) and milk. In contrast to emulsions microemulsions are seldom observed in nature as the high surface area is energetically unfavorable. The difference between emulsions and microemulsions originates from the underlying droplet diameters. Emulsions are generally considered to possess diameters greater than 1 μm while the term microemulsion refers to droplet sizes between 1 and 100 nm. Intermediate diameters are sometimes referred to as miniemulsions (Table 2.11). However, the terms emulsion and miniemulsion are used quite loosely.

Table 2.10: Distinction between binary liquid systems by droplet diameter

Designation	Droplet diameter range
Emulsion	> 1 μm
Miniemulsion	100 nm – 1 μm
Microemulsion	< 1 nm

Emulsions require stabilizer molecules to prevent associations of droplets and phase separation. The stability of a binary fluid systems is described by the Gibbs free enthalpy.

$$\Delta G = \gamma \Delta A - T \Delta S \quad (2.26)$$

For two immiscible fluids the surface work term is quite high. The resulting process is called Ostwald ripening. The underlying theory was investigated by Lifshitz and Wagner, however exceeds the scope of this book [239, 240]. Ageing of an oil in water emulsion causes smaller droplets to shrink and larger ones to grow. This behavior is caused by the hydrophobic effect. As the droplet diameters increase the system gains entropic energy from fewer oriented water molecules around the nonpolar phase.

Microemulsions typically require an additional co-emulsifier. The extremely small droplets cause two changes in the system. On the one hand, the system gains entropic energy by dividing all large droplets into many smaller ones. On the other hand, the surface work increases as the resulting surface increases proportional to r^3 . This effect exceeds the entropic gain, hence the surface energy has to be lowered significantly. The co-stabilizer is included in equation 2.26 via

$$\gamma_{O/W} = \gamma_{O/W}^0 - \int_0^{c_S} \Gamma_S RT d(\ln c_S) - \int_0^{c_{CS}} \Gamma_{CS} RT d(\ln c_{CS}) \quad (2.27)$$

where S denotes surfactant and CS co-surfactant. Γ is the surface excess. By choosing suitable co-surfactants, interfacial tensions as low as 10^{-4} mNm⁻¹ can be realized. Since co-surfactant and surfactant must not interact with each other the choice is somewhat limited.

Chapter III

PHASE BEHAVIOR OF AQUEOUS HEXAMETHOXYMETHYL MELAMINE SYSTEMS

3.1 INTRODUCTION

Hexamethoxymethyl melamine (HMMM) is a widely used cross-linking agent in waterborne polymer systems. Despite its widespread use there is little information about microscopic properties and the phase behavior of aqueous HMMM mixtures. Triazine derivatives show strong adsorptive behavior towards graphene. Preliminary test using HMMM as a stabilizing agent for graphene indicated that stable graphene-HMMM composite dispersions are obtained at low HMMM concentrations between 1 and 10 g/L. Higher concentrations resulted in precipitation of graphite sediments. In contrast, syntheses of HMMM nano particle dispersions (MP) are only possible using concentrations above 10 g/L at elevated temperatures. The minimal reaction temperature is specified by the turbidity of the mixture. The goal of this study is the characterization of the phase behavior of aqueous HMMM systems. The results will provide the basis for the synthesis of MP and graphene composite dispersions.

3.2 EXPERIMENTAL

3.2.1 PREPARATION OF HMMM SYSTEMS

Aqueous HMMM samples were prepared in concentrations ranging from 10 to 400 g/L (Maprenal MF900/95w, Ineos Melamines, 95 % in water, <0.75 % formaldehyde). Samples are denoted as Phase_{concentration}, e.g. ME₄₀₀ for a microemulsion phase at 400 g/L HMMM. Material loss due to filtration is not accounted for. The resulting clear to turbid mixtures were filtered (0.45 µm syringe filter, cellulose-acetate membrane, Minisart) to remove large aggregates and dust. For the duration of the experiments the clear HMMM systems were stored in airtight vials at room temperature. The concentrations were controlled gravimetrically and, depending on the theoretical concentrations, indicated a decrease of 2.5 % to 11 % after filtration. Deviations from theoretical values originate from removal of large aggregates.

3.2.2 ANALYTICAL STUDIES

Measurements of pH values were conducted as function of time (SevenMulti S40, InLab Expert Pro electrode, Mettler-Toledo). Dynamic light scattering measurements (ZetaSizer Nano ZS, 633 nm, CONTIN algorithm, Malvern Instruments) were conducted immediately after sample preparation and subsequently in specific time intervals. Measurements of freshly prepared and aged systems (800 h) were performed at temperatures between 25 °C and 80 °C to characterize the phase inversion.

3.3 RESULTS

3.3.1 ESTIMATION OF HLB VALUE AND HANSEN SOLUBILITY PARAMETERS

The hydrophilic-lipophilic balance (HLB) is a straightforward tool for the characterization of the solubility behavior of non-ionic surfactants in water. The HLB is calculated via

$$HLB = 20 \cdot \frac{M_h}{M_g} \quad (3.1)$$

where M_h is the molecular weight of the hydrophilic parts of the molecule (in this case 180 g/mol; $6 \cdot O + 6 \cdot N$) and M_g is the overall molecular mass ($M_{HMMM} = 390.44$ g/mol, idealized value, not accounting for pre-condensation)^[241]. Evaluation yields a HLB value of 9.22 which is indicative of an oil in water (O/W) emulsifier. Since by definition the HLB value is primarily applicable to linear non-ionic surfactants this result is confirmed by calculating the solubility parameter (cohesive energy density, “Hansen parameters”) difference of HMMM in water.

The difference in Hansen solubility parameters is calculated via^[242]

$$\Delta\delta = \sqrt{[\delta_D(S) - \delta_D(P)]^2 + [\delta_P(S) - \delta_P(P)]^2 + [\delta_H(S) - \delta_H(P)]^2} \quad (3.2)$$

Inserting the respective values for water and hexamethoxymethyl melamine (table 3.1^[238]) yields $\Delta\delta = 6.1 \text{ J}^{1/2}\text{cm}^{3/2}$ which is just above the threshold value of $6 \text{ J}^{1/2}\text{cm}^{3/2}$ for complete solubility of two substances.

Table 3.1: Hansen solubility parameters of water and hexamethoxymethyl melamine^[243]

Substance	$\delta_D \left[\text{J}^{1/2}\text{cm}^{3/2} \right]$	$\delta_P \left[\text{J}^{1/2}\text{cm}^{3/2} \right]$	$\delta_H \left[\text{J}^{1/2}\text{cm}^{3/2} \right]$
Water	14.3	16.3	42.6
Hexamethoxymethyl melamine	20.4	8.5	10.6

The results suggest that HMMM is poorly soluble in water and instead is expected to form HMMM in water (H/W) emulsions.

3.3.2 PHASE BEHAVIOR AS FUNCTION OF TIME AND HMMM CONCENTRATION

The phase behavior of HMMM in water was investigated at concentrations between 10 and 367 g/L. Depending on the specific concentration, HMMM forms either emulsion droplets (E), microemulsion droplets (ME) or both (EME) simultaneously. The phase diagrams (figure 3.1) were calculated from relative light scattering intensities.

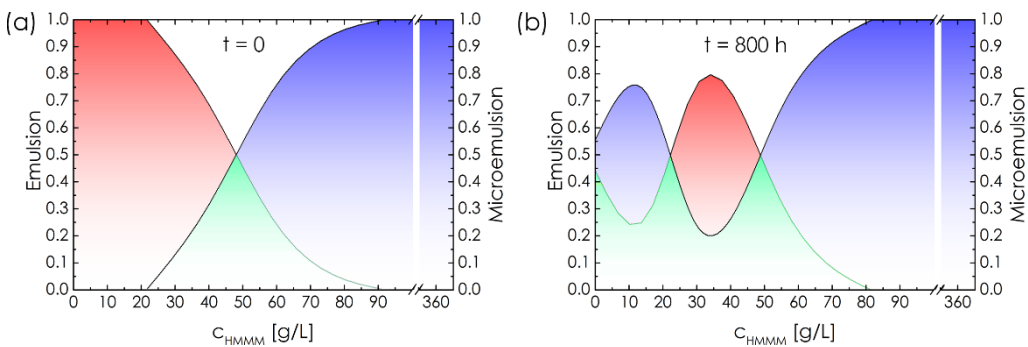


Figure 3.1: Phase diagrams of (a) freshly prepared EME and (b) aged EME

Freshly prepared mixtures exhibit stable emulsion droplets between 10 and 30 g/L HMMM. At concentrations below 10 g/L the systems undergo Ostwald ripening which results in rapid precipitation. Above 30 g/L HMMM forms emulsion and microemulsion droplets. Emulsion droplets persist up to 90 g/L. At concentrations above 90 g/L the system solely consists of microemulsion droplets. Droplet diameter measurements of freshly prepared EME systems emphasize the dependence on HMMM concentration (figure 3.2d). Both E and ME diameters increase linearly with c_{HMMM} . Ageing changes the phase diagrams. Sole emulsion droplets are no longer observable. Further, the range in which emulsion droplets are present reduces. After 800 hours the EME system extends from 10 to 63 g/L. In order to characterize the occurring changes in the systems, time-resolved pH and DLS measurements were conducted. Starting at slightly acidic pH values all samples exhibit an asymptotic increase of pH value with time. The final pH value depends on HMMM concentration and increases

with decreasing HMMM concentration. Compared to low concentrations higher concentrations show less difference in pH value. The initial acidity originates from methanol and formaldehyde present in the bulk phase. Although formaldehyde does not react acidic the reaction between formaldehyde and water yields methylene glycol which possesses some acid strength. HMMM reacts slightly basic and causes the alkaline pH value of low-concentrated samples. The increase of pH over time indicates that methanol and methylene glycol disappear from the bulk phase during ageing of the systems.

Time-resolved measurements of emulsion and microemulsion droplet diameters were conducted for 800 hours to gain further insight into the ageing process. The microemulsion diameter of ME₃₀ to ME₂₀₀ remains almost constant over time. In contrast, ME₃₀₀ and ME₄₀₀ droplet diameters decrease. During the first 50 hours the diameters of E₁₀ to E₅₀ decrease slightly as well. Further ageing of E₅₀ results in steady increase in average diameter accompanied by broader size distributions (not shown). The increase in droplet diameter of sample E₃₀ is slower. Both effects are indicative of Ostwald ripening.

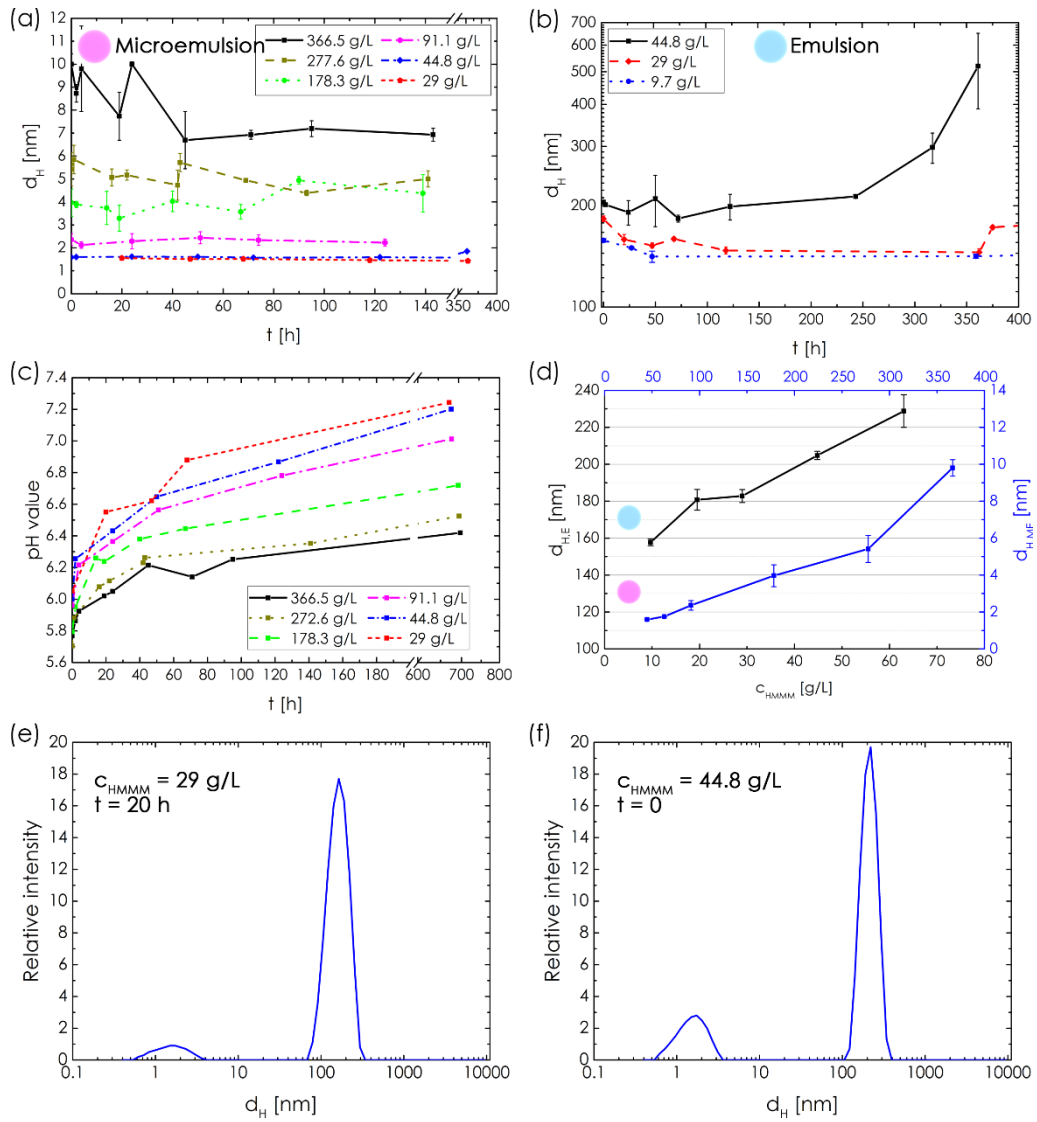


Figure 3.2: (a) ME droplet diameter as function of time; (b) E droplet diameter as function of time; (c) pH value as function of time; (d) E and ME droplet diameters as function of HMMM concentration

To sum up, the pH value of aqueous HMMM systems steadily increases with time. Secondly, the ratio of microemulsion to emulsion increases with time. Thirdly, the microemulsion and emulsion droplet diameters decrease. Based on these findings the following ageing mechanism is proposed. Methanol and methylene glycol act as surfactant and co-surfactant which are necessary for

microemulsion droplets. Depending on HMMM concentration the molecules either form new microemulsion droplets from emulsion droplets or split present microemulsion droplets which accounts for the decreasing diameter. The formation of ME droplets from E droplets accounts for the increasing ME/E ratio and the decreasing emulsion diameters. Further, due to the effective removal of both methanol and methylene glycol the pH value of the bulk phase increases.

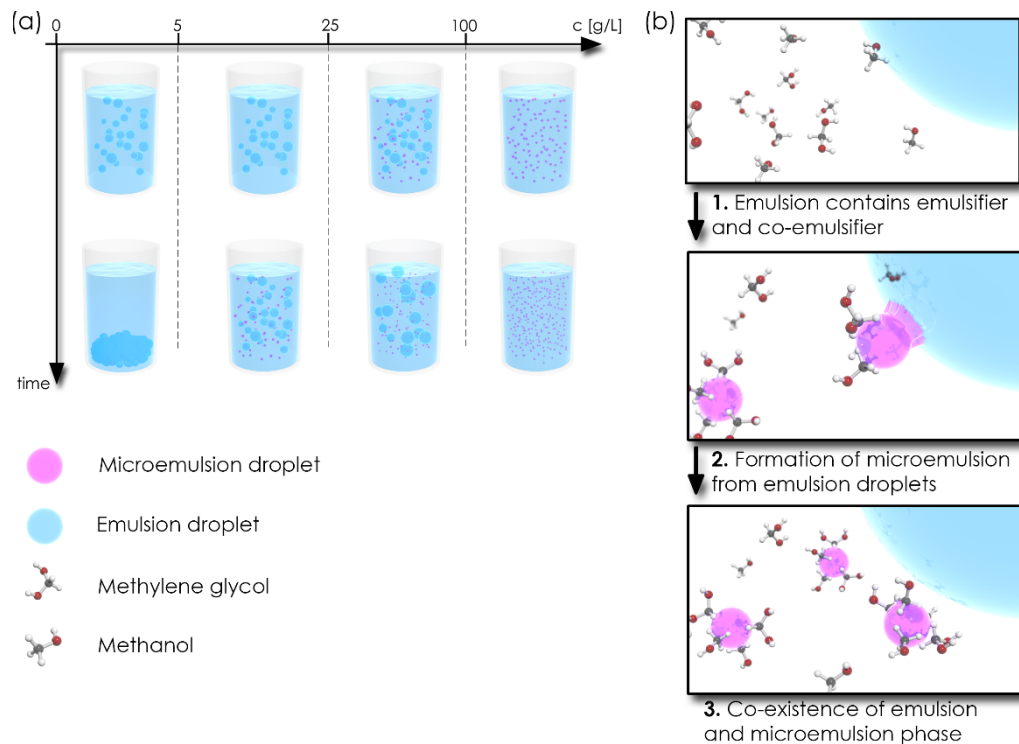


Figure 3.3: (a) Concentration and time-dependent phase behavior of aqueous HMMM systems; (b) Mechanism of HMMM microemulsion formation

3.3.3 HMMM PHASE INVERSION

The onset of turbidity during heating of aqueous HMMM systems originates from a phase inversion leading to water in HMMM (W/H) emulsions.

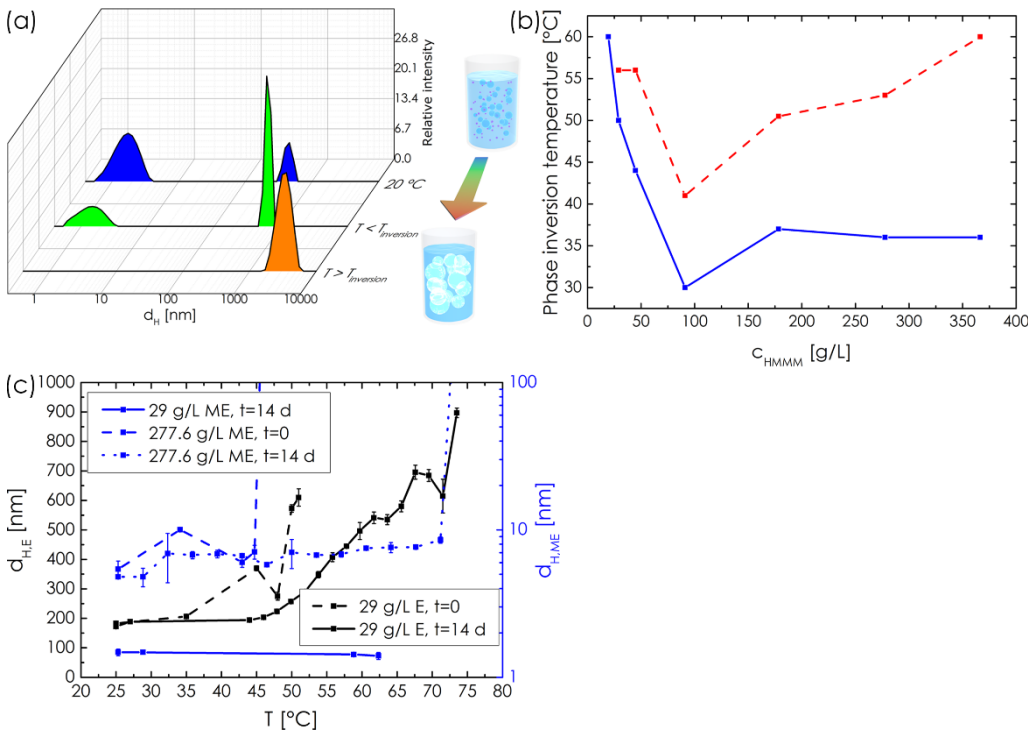


Figure 3.4: (a) Development of HMMM droplet diameter upon temperature increase; (b) Phase inversion temperature as function of HMMM concentration; (c) Emulsion and microemulsion droplet size as function of temperature

The W/H emulsion consists of micrometer-sized water droplets (figure 3.5). The phase inversion is not observed at HMMM concentrations below 10 g/L. Whether this behavior relates to concentration or thermodynamics remains unknown. The process is completely reversible. Multiple experiments showed that crossing the phase inversion temperature (T_{PI}) multiple times is possible without impairing the integrity of EME. However, due to the energy input, the ageing of the systems is accelerated. As an example, a freshly prepared emulsion (30 g/L) shows no microemulsion droplets. Crossing the phase inversion

temperature and returning to room temperature afterwards causes immediate formation of the microemulsion phase which otherwise would not have been observed for hours. In order to investigate the dependence of T_{PI} on HMMM concentration, hydrodynamic diameters of freshly prepared and aged systems were determined as function of temperature. The results show that T_{PI} is highly dependent on c_{HMMM} . The phase inversion temperature of freshly prepared EME decreases with increasing c_{HMMM} . Formation of an inverse emulsion phase is highly dependent on the amount of HMMM present since above T_{PI} HMMM acts as continuous phase. Around 100 g/L T_{PI} exhibits a minimum value. Above 100 g/L there is solely thermodynamically stable ME phase present which explains the increase in T_{PI} . The phase inversion temperature of aged EME is greatly increased compared to fresh EME. This effect is attributed to the higher ME/E ratio and the higher stability of ME. The opposite occurs at low concentrations at which the aged EME become less stable over time.

3.4 SUMMARY AND CONCLUSIONS

Hexamethoxymethyl melamine exhibits a complex phase behavior which depends on HMMM concentration, ageing and temperature. Phase diagrams of freshly prepared and aged emulsion-microemulsion systems (EME) were developed. Up to 30 g/L, freshly prepared aqueous HMMM mixtures consist of emulsion droplets with diameters around 200 nm. Between 30 and 100 g/L emulsion and microemulsion coexist. Beyond 100 g/L the system consists solely of microemulsion droplets. Upon ageing, there is a strong tendency towards formation of microemulsion droplets. The required surfactants for this process are methanol and methylene glycol. With time the EME range changes from 30 to 100 g/L to 10 to 60 g/L. In this process both the average emulsion and microemulsion droplet diameters decrease as HMMM migrates from emulsion to microemulsion droplets.

EME systems exhibit a reversible phase inversion to water in HMMM (W/H) emulsions. The average droplet diameter increases to several microns. The phase inversion temperature is highly dependent on HMMM concentration and shows a minimum just below 100 g/L. Ageing of EME generally increases the inversion temperature due to the higher stability of microemulsion droplets.

The key findings of this study provide an explanation for the conditions required for graphene stabilization and HMMM nanoparticle synthesis. Graphene stabilization requires HMMM emulsions whereas MP synthesis requires a ternary system consisting of emulsion and microemulsion droplets.

Chapter IV

AQUEOUS HEXAMETHOXYMETHYL MELAMINE NANO PARTICLE DISPERSIONS

4.1 INTRODUCTION

Reactions between HMMM and OH functional polymers with HMMM are elementary to many fields of applied polymer science. Besides the acid-catalyzed co-condensation the triazine derivative self-condensates to a significant degree. The amount of self-condensation can be controlled e.g. by varying the systems' pH values or by implementation of substituents other than methoxy groups. The kinetics of the co-condensation reaction is well known. In contrast, there is limited information about the mechanism and kinetics of the self-condensation. The self-condensation of HMMM can be used to synthesize aqueous nano particle dispersions (MP). HMMM nano particles possess a positive surface charge and variable diameters. The rigid particles show an anisotropic shape. MP can be used to mechanically enhance polymeric matrices. Preliminary tests showed that MP dispersions can be used to stabilize graphene in water. The composite dispersions are stable for several weeks. This chapter deals with the HMMM nano particle dispersion (MP) synthesis. Based on a mechanistic and kinetic analysis a complete scheme of the synthesis is provided.

4.2 EXPERIMENTAL

4.2.1 SYNTHESIS AND KINETIC STUDIES

HMMM nano particle dispersions were synthesized in concentrations between 10 and 100 g/L. In a typical procedure, hexamethoxymethyl melamine (Maprenal MF900w/95, Ineos Melamines) was mixed with water resulting in a turbid system containing emulsion and microemulsion droplets (EME). Following filtration, the now transparent EME was heated to the desired reaction temperature. Particle syntheses were conducted at four temperatures, 60, 70, 80 and 90 °C. Reaching the EME phase inversion temperature, T_{PI} , causes clouding of the mixture. The reaction was initiated by adding specific amounts of hydrochloric acid (Sigma-Aldrich, 37 %). The syntheses were conducted using at least three different amounts of HCl for each temperature and HMMM concentration. During the reaction the pH value was monitored continuously. A constant pH value for the duration of one minute marks the end of the reaction. Depending on concentration of HMMM and hydrochloric acid the product shows very light blue to milky blue color.

4.2.2 ANALYTICAL STUDIES

Kinetic studies were performed by monitoring the mixtures' pH value (SevenMulti S40, Inlab Expert Pro electrode, Mettler-Toledo) over time. The interval between each data point was ten seconds. HMMM nano particle dispersions were characterized in terms of particle size, charge and structure. Zeta potential and dynamic light scattering measurements (ZetaSizer Nano ZS, 633nm Malvern Instruments) were preformed immediately after the dispersions had cooled to down room temperature. Structural analyses via X-ray diffraction (Bruker D5005, Cu-K α 0.154 nm) were conducted in transmission geometry at

angles between 3 and 110 ° 2Θ . For this purpose the dispersions were enclosed in self-crafted fluid cells (PET).

Morphological studies via atomic force microscopy (AFM, Bruker Dimension Icon, Nanoscope V controller, peak force tapping mode) and scanning electron microscopy (SEM, Zeiss Neon 40, U = 3kV, d = 5 mm) were conducted on spray applied samples. Silicon wafers were used as substrates. FTIR spectroscopy (Bruker Alpha P, λ = 633 nm) at wavenumbers between 400 and 4000 cm^{-1} provided further insight into particle structure and surface chemistry.

4.3 RESULTS

MP synthesis depends on the three variables reaction temperature, HMMM concentration and concentration of acid catalyst. All parameters affect different aspects of the reaction. Preliminary tests showed that reaching EME phase inversion temperature (T_{PI}) is crucial for successful synthesis. Increasing temperature above T_{PI} results in a higher reaction rate. Figure 4.1 illustrates the dependence on HMMM and acid concentration. Successful synthesis mandates the use of HMMM in concentrations between 10 and 55 g/L. Due to the necessity of EME phase inversion lower values prevent the reaction. Concentrations above 55 g/L result in partial precipitation of MP in form of agglomerates. Variation of catalyst concentration between specific concentrations $C_{H^+,1}$ and $C_{H^+,2}$ enables particle size control.

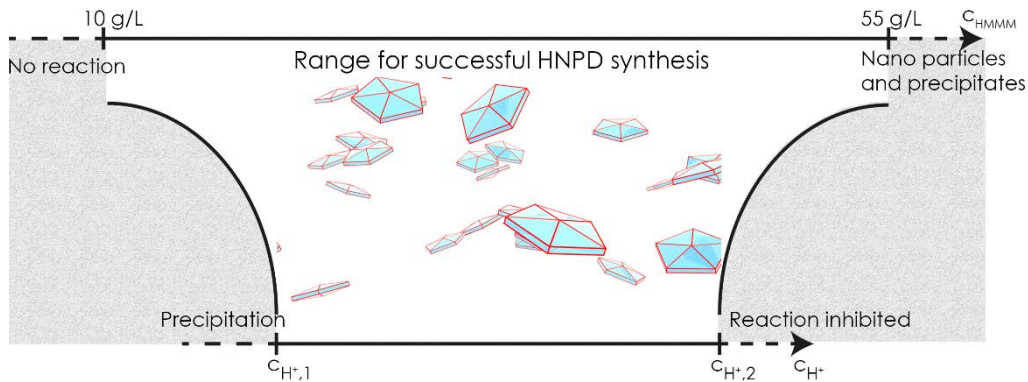


Figure 4.1: Concentration limits of HMMM and proton concentration for successful nano particle synthesis

Insufficient amounts of catalyst result in instability and precipitation while excess amounts inhibit the reaction due to reduced reactivity of HMMM methoxy groups. The second effect is caused by protonation of the triazine ring and formation of stable reaction intermediates. The MP synthesis is divided into two phases. EME phase inversion comprises phase 1. Subsequent initiation by addition of acid catalyst marks the beginning of phase 2 which further includes

particle growth. The progression of phase 1 was tracked via temperature-dependent DLS measurements. Phase 2 was monitored via time-dependent DLS and pH measurements.

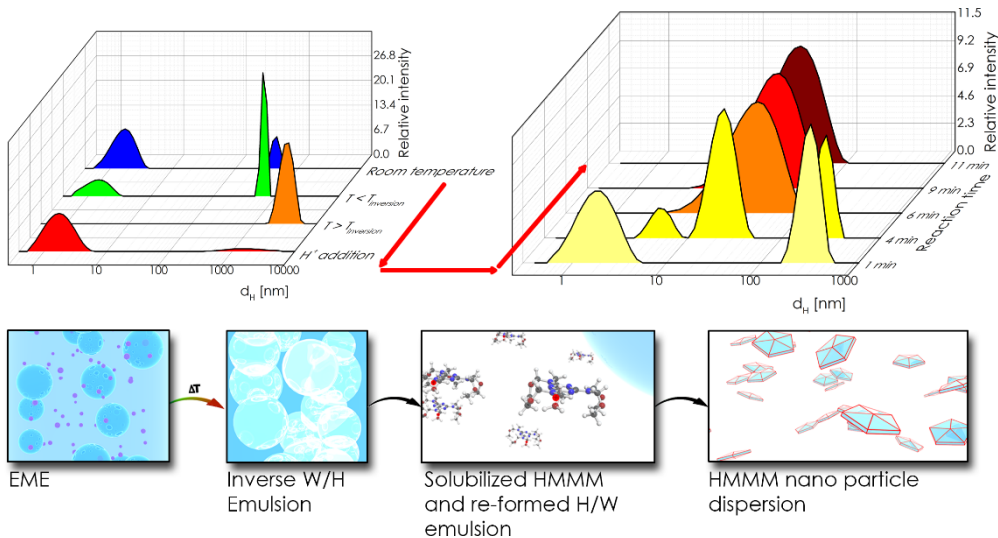


Figure 4.2: Temperature and time-resolved hydrodynamic diameters as means to monitor the HMMM nano particle reaction

Figure 4.2 exhibits an exemplary course of the reaction leading to particles with diameters around 40-50 nm. Heating of EME results in phase inversion which yields water in HMMM (W/H) emulsions. At room temperature EME consists of microemulsion droplets around 2 nm and emulsion droplets around 400 nm. Increasing temperature causes a shift from microemulsion to emulsion droplets. This ultimately leads to micrometer sized W/H emulsion droplets after crossing T_{PI} . Subsequent initiation results in immediate solubilization of large parts of the W/M emulsion. The few remaining droplets exhibit diameters around 1-2 μm and are reorganized H/W emulsion droplets. RCH_2OCH_3 protonation sets in immediately after addition of the acid. Shortly after the initiation there are two species present, the hydrolyzed HMMM and the remaining H/W emulsion. After four minutes the dispersion already contains particles with diameters around 10 to 30 nm. The H/W emulsion phase decreases continuously. Particle growth

progresses until the H/W emulsion is depleted. After 6 minutes the dispersion contains particles with diameters of 40-50 nm.

A kinetic analysis of the reaction provides information about phase 2. The reaction mechanism is complex and consists of several sub-steps (figure 4.3).

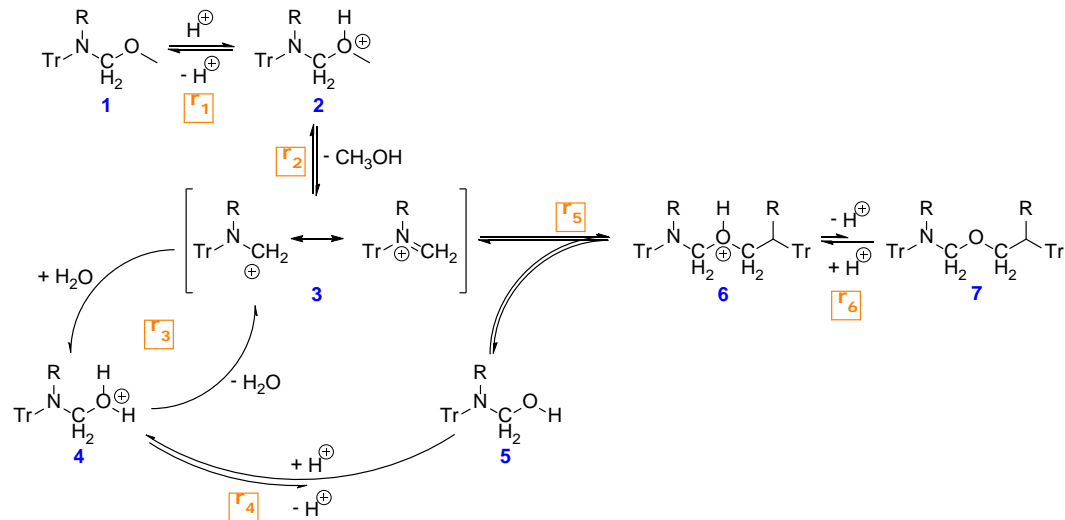
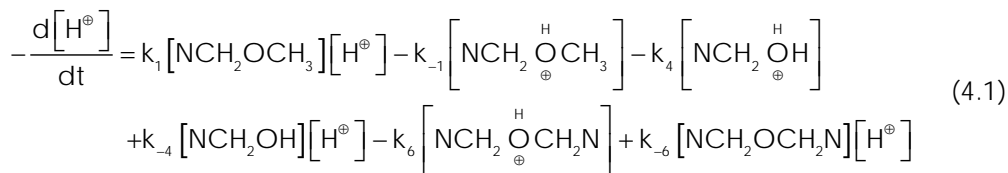


Figure 4.3: Reaction mechanism of HMMM self-condensation

The reaction starts by protonation of RCH_2OCH_3 (1) and subsequent elimination of methanol. The formation of intermediate 3 is the rate determining step of the reaction. Intermediate 3 reacts with water yielding 4. Since the reaction is carried out at low pH values, the equilibrium between 4 and 5 is strongly shifted to 4. The increasing pH value due to continuous protonation of 1 causes an equilibrium shift from 4 to 5. Reaction between 5 and 3 is the final step yielding 6. The low pH value and the formation of intramolecular hydrogen bridges result in an equilibrium that is strongly shifted to 6. The remaining positive charge is the origin of the surface charge of MP.

Kinetic modeling of the initial stage of the reaction ($f \leq 5\%$) requires several simplifications. Because of the high temperature and the fact that the reaction is

carried out in an open system, methanol is expected to evaporate instantly. Commercial HMMM resins usually contain 23 % dimers, 15% trimers and higher oligomers. Based on these values, an average molar mass of 573 g/mol and an average functionality of 5.6 are calculated. It is further assumed that all functional groups are equally reactive and that reactivity is not impaired by previous condensation. The overall reaction rate (equation 4.1) depends on several intermediate concentrations and cannot be solved analytically.



The initial reaction rates are determined by fitting a polynomial (equation 4.2) to the measured $C_{H^{\oplus}}$ vs. time curves (figure 4.4a) [244].

$$C_{H^{\oplus}} = C_{H^{\oplus},0} + \underbrace{\left(\frac{dc_{H^{\oplus}}}{dt} \right)_0}_{\text{initial rate}} t + \left(\frac{d^2c_{H^{\oplus}}}{dt^2} \right)_0 t^2 + \dots \left(\frac{d^n c_{H^{\oplus}}}{dt^n} \right)_0 t^n \quad (4.2)$$

Double logarithmical plotting of initial rates as function of initial proton concentration yields effective rate constants for constant $ROCH_3$ concentrations and the reaction order of proton concentration (equation 4.3).

$$\log r_0 = \log k_{\text{eff}} + a \cdot \log C_{H^{\oplus},0}^n \quad (4.3)$$

$$k_{\text{eff}} = k \cdot C_{ROCH_3,0}^m \quad (4.4)$$

Calculation of the actual rate constants was done according to equation 4.4. The reaction is first order in proton concentration. The Arrhenius plot yields an activation energy of $E_A = (136 \pm 35)$ kJ/mol. Activation energies of HMMM polyol condensations range between 60 kJ/mol (poly-acrylics, polyesters) and 170 kJ/mol (alkyd resins). The rate determining step in the case of self-

condensation is the same as in co-condensation. The similarity of the values explains HMMM cluster formation in organic coatings.

Proton conversion and conversion rate are used to describe the later part of the reaction ($f \geq 5\%$) (figure 4.5). The initial proton concentration is held constant at $C_{H^+,0} = 0.0015 \pm 0.0003 \text{ mol} \cdot \text{L}^{-1}$.

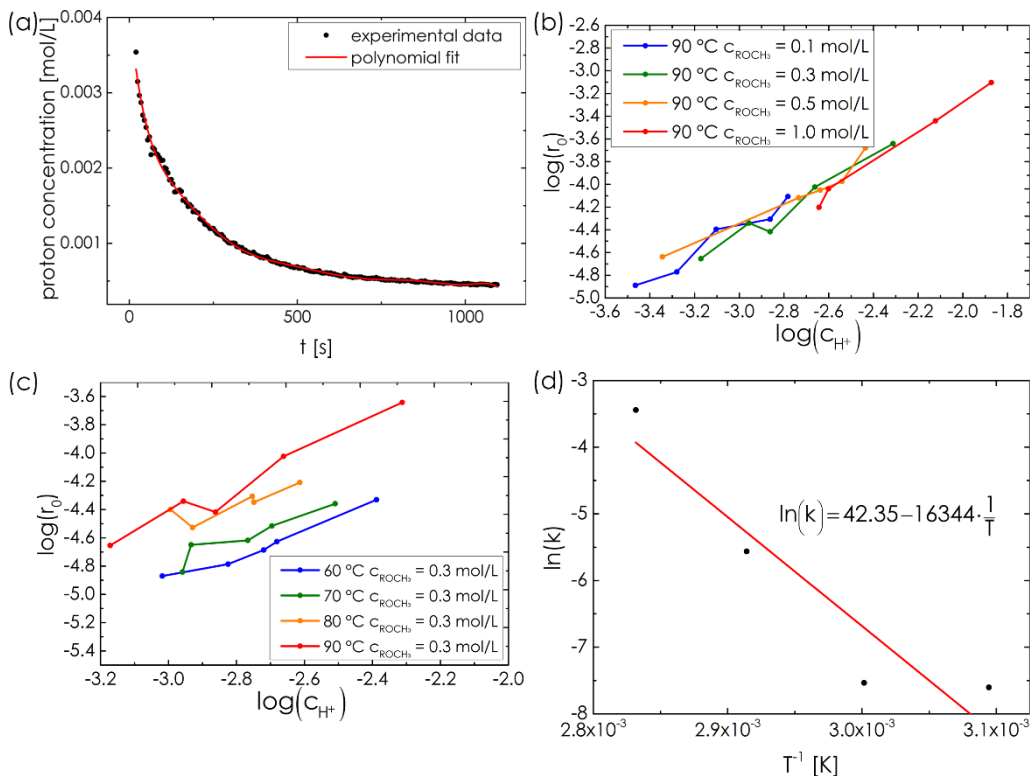


Figure 4.4: (a) Exemplary polynomial fit ($C_{CH_2OCH_3} = 0.3$); (b) Initial rate as function of initial proton concentration, constant temperature; (c) Initial rate as function of initial proton concentration, constant initial CH_2OCH_3 concentration; (d) Arrhenius plot

Conversion as function of time ($f(t)$) shows that the reaction temperature does not influence the maximum conversion (f_{\max}). This excludes dynamic interactions between MP charge carriers and water. In contrast, f_{\max} decreases as HMMM concentration increases. Constant initial acid concentration implies a constant number of reaction centers. Higher monomer concentrations thus results in larger particles. Since the dissociation equilibrium only governs the

particle surface, the reduced relative surface due to larger particles causes the decreasing total proton conversion. Conversion rate as function of conversion, $(df/dt)(f)$ depends on HMMM concentration and temperature. Intermediate HMMM concentrations ($c_{\text{RCH}_2\text{OCH}_3} = 0.3 \text{ mol/L}$, $c_{\text{HM}} = 30 \text{ g/L}$) result in the highest conversion rate. Lower concentrations slow down the reaction since it is first order in ROCH_3 concentration.

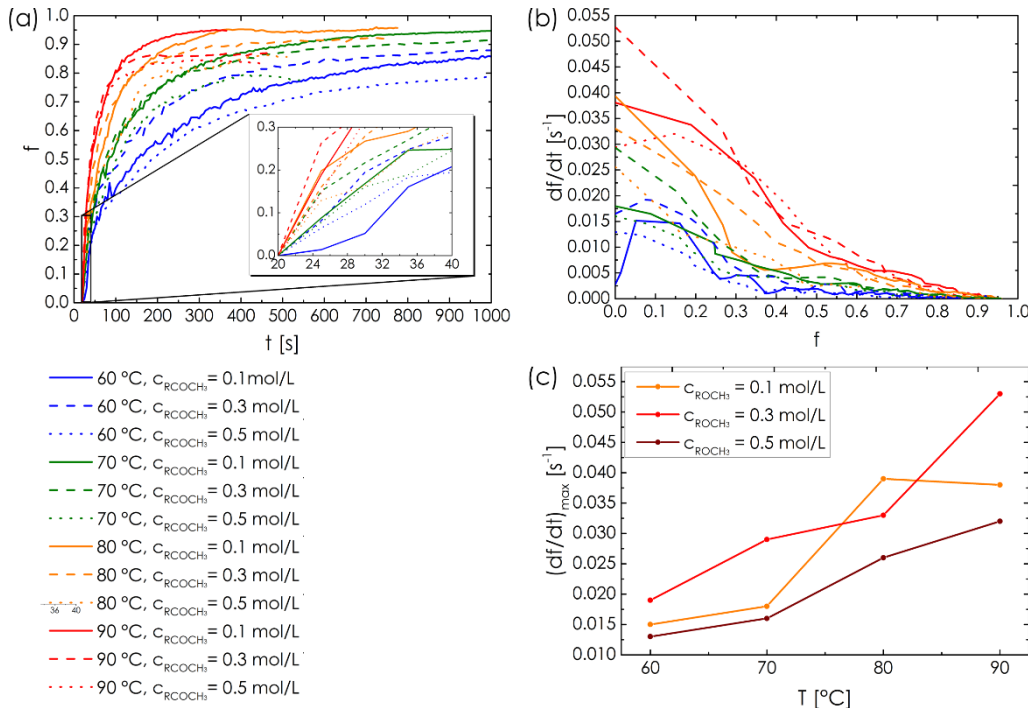


Figure 4.5: (a) Proton conversion as function of time; (b) Proton conversion rate as function of conversion; (c) maximum conversion rate as function of reaction temperature

The decreasing rate at RCH_2OCH_3 concentrations above 0.3 mol/L is attributed to diffusion processes and slower solubilization of the W/H emulsion. Temperature increase has major impact on the maximum conversion rate (figure 4.5c). The delay to reach $(df/dt)_{\text{max}}$ observed in some cases is attributed to diffusion processes as well. Taking all results into account, the most efficient reaction conditions were observed at intermediate HMMM concentrations and temperatures above 70°C. Zeta potential measurements were conducted to gain

information about MP charge and stability. Zeta potentials of stable dispersions are of magnitude +25 mV and higher. Long-term stability is compromised by significantly altering the pH value in either direction. On the one hand, addition of acids causes further condensation between nanoparticles resulting in fast precipitation. On the other hand, addition of bases destabilizes the dispersions due to lack of electrostatic repulsion. The measured potentials are not related to the various parameters and are randomly distributed around +25 mV.

Table 4.1: HMMM ring vibrations before and after particle synthesis [245, 246]

Vibration	HMMM	MP	Shift
Ring breath	869	-	-
Ring N i-ph. radial vibration	958	974	16
Semi str.	1185	1199	14
Semi str.	1332	1349	15
Semi str.	1387	-	-
Quad. str.	1438	-	-

FTIR and X-ray diffraction measurements provide insight into the particles' structure (figure 4.7). Infrared spectra of HMMM and MP consist of several sum peaks. However, the spectra contain qualitative information about ROCH_3 conversion and MP structure.

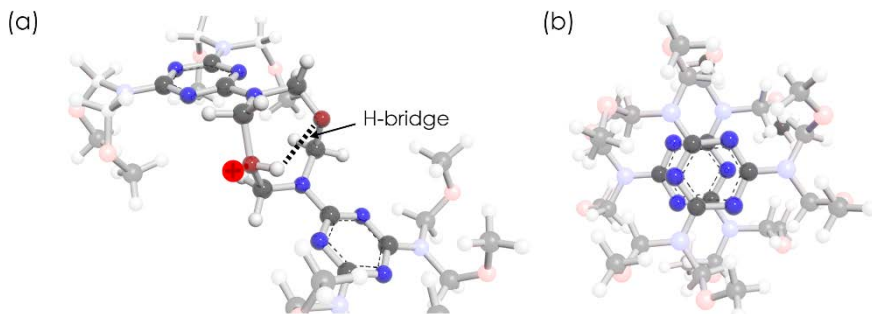


Figure 4.6: (a) Double dimethylene ether bridge between two MP molecules; (b) top view of two MP molecules

Isolated HMMM - CH_3 peaks are found at 2985 cm^{-1} and 2823 cm^{-1} . MP in comparison shows numerous peaks associated to CH_2 vibrations at 2965 cm^{-1} , 2905 cm^{-1} and between 1600 cm^{-1} and 1300 cm^{-1} but lacks CH_3 peaks which indicates a high conversion of methoxy groups during the reaction. Further, numerous triazine ring vibrations are observed (table 4.1). All major ring vibrations shift to higher wavenumbers which results from stacking of HMMM aromatic rings in MP. The missing bands at 869 cm^{-1} , 1387 cm^{-1} and 1438 cm^{-1} confirm aromatic interactions. Triazine rings are known to exhibit aromatic π -stacking interactions leading to offset stacking of the aromatic rings. In contrast to HMMM, MP shows high amounts of hydrogen bonds. The relative intensity of the OH stretching vibration in HMMM around 3300 cm^{-1} is accompanied by a peak shift of 60 cm^{-1} to lower wavenumbers in MP. A similar shift is observed at for the C-O-C vibrations at 974 cm^{-1} (HMMM: 1020 cm^{-1}). This leads to the conclusion that hydrogen bonding occurs between adjacent dimethylene ether bridges. X-ray diffraction patterns of EME and MP show HMMM d_{010} , d_{100} and d_{001} peaks at 22.5 , 34.5 and $28 \text{ }^{\circ}\Theta$ (figure 4.7b). The d_{001} peak originates from stacking of HMMM molecules and is significantly more intense in MP than in EME. This result supports that stacking of aromatic triazine centers is a major structural feature of MP.

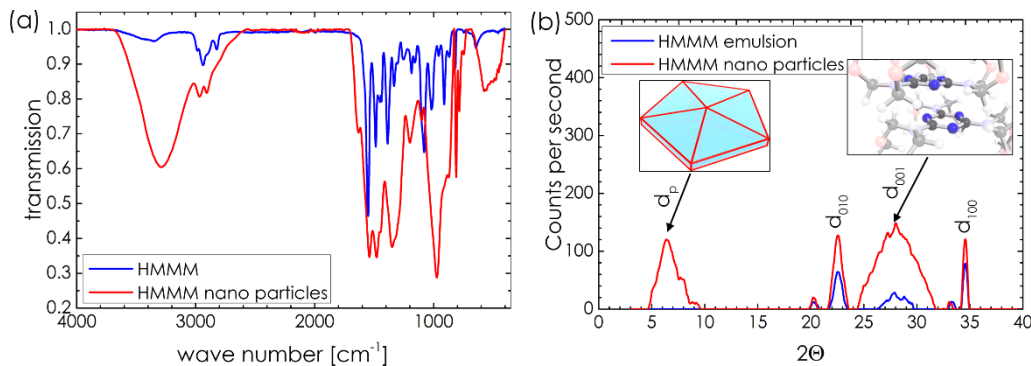


Figure 4.7: (a) FTIR and (b) XRD spectra of HMMM and MP

The crystallite size is calculated using the Scherrer equation. On the basis of d_{001} an approximate crystallite size of 4 nm was calculated. Further, MP shows a broad peak at $6.4^\circ 2\Theta$. Calculation on the basis of the d_p peak results in diameters around 8 nm which is in agreement with the primary particle size of the nano particles. Both determined crystallite sizes underline the particle anisotropy. Characterization of particle size and morphology was performed via dynamic light scattering, atomic force microscopy and scanning electron microscopy (figure 4.8). Hydrodynamic diameters are a function of initial proton concentration. Increasing $C_{H^+,0}$ results in decreasing particle diameters. Particle diameters around 5-10 nm are obtained at high proton concentrations. This is in agreement with the diameters calculated from the XRD patterns. Particles with diameters around 250 nm can be synthesized by adding minimal amounts of catalyst. The MP particle size can be controlled between 10 and 200 nm. The measured values are in close correlation with AFM and SEM results. Both techniques provide additional information about particle height and anisotropy.

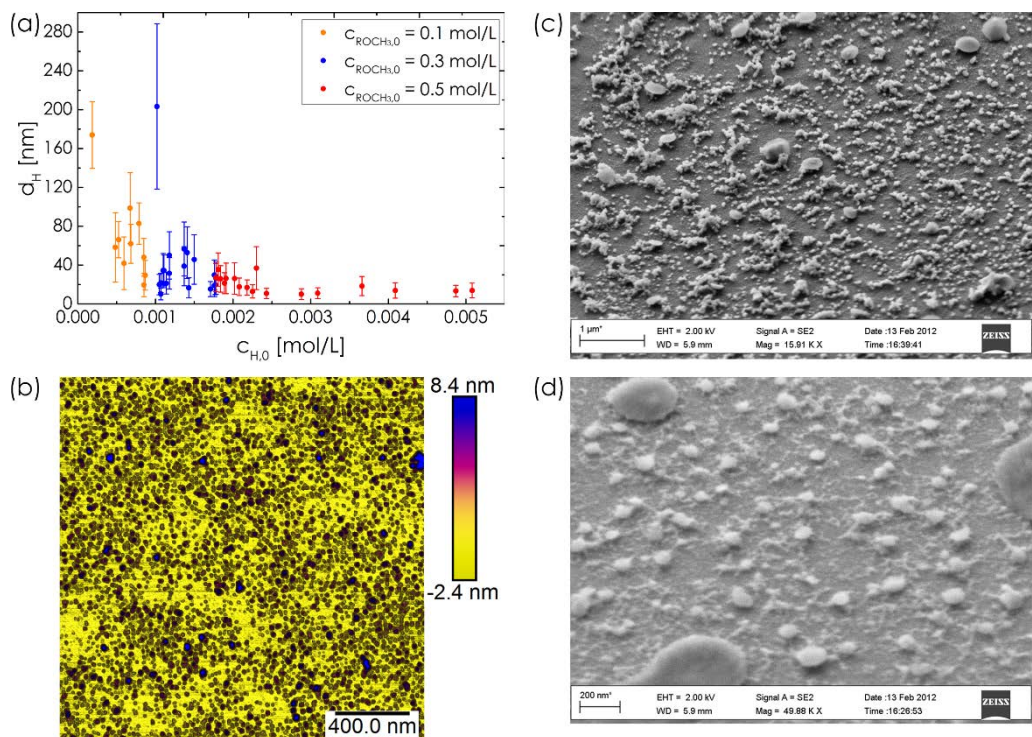


Figure 4.8: (a) Hydrodynamic diameter as function of initial proton concentration; (b) AFM image of MP spray coated on Si wafer; (c) and (d) SEM images of MP on Si wafer at different magnification

The exemplary AFM image shows particles with lateral dimensions of (20.22 ± 11.11) nm and height of (3.25 ± 1.94) nm. The calculated diameter/height aspect ratio amounts to 6. Aspect ratio increases with increasing particle diameter. SEM images reveal almost disc-like particles with diameters up to 200 nm. To sum up, morphological studies via AFM and SEM confirm that primary growth during particle synthesis occurs predominantly in lateral dimensions.

4.4 SUMMARY AND CONCLUSION

HMMM nano particle dispersions were successfully synthesized in concentrations up to 55 g/L. Temperature and time dependent DLS measurements were used to track the reaction which consists of two phases, emulsion-microemulsion (EME) phase inversion and particle growth.

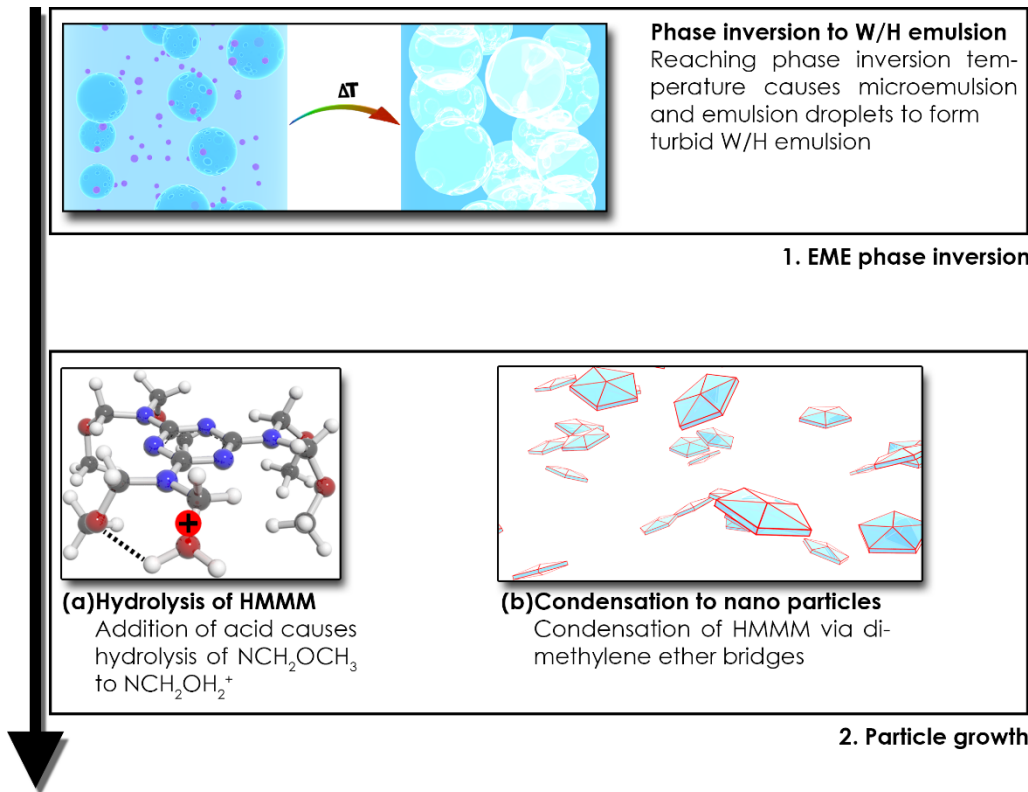


Figure 4.9: Illustrative mechanism of MP synthesis covering EME phase inversion, solubilization of HMMM and particle growth

Particle growth includes initiation by protonation of RCH_2OCH_3 groups and propagation. HMMM molecules are connected via dimethylene ether bridges. By monitoring the pH value as function of time a kinetic and mechanistic model of the reaction was developed. The reaction is first order in proton concentration and possesses an activation energy of $E_A = (136 \pm 35) \text{ kJ/mol}$. This value is

comparable to HMMM co-condensation. By choosing suitable acid catalyst concentrations the particle diameters can be controlled between 5 and 250 nm. The diameter/height aspect ratio of MP increases with increasing particle diameter. MP are positively charged and possess zeta potentials up to +40 mV. It was shown, that ternary hydrogen bonds between adjacent dimethylene ether bridges are the primary charge carriers. Spectroscopic and X-ray diffraction measurements provided evidence for partial crystallinity. The crystalline structure originates from stacked triazine rings in MP.

Chapter V

CHEMICAL DOPING IN AQUEOUS GRAPHENE-HMMM COMPOSITE DISPERSIONS

5.1 INTRODUCTION

Triazine and its derivatives show strong molecular interaction with graphene. The main interaction mechanism is a charge transfer from graphene to the triazine ring. The adsorption energy increases with increasing capability of stabilizing additional charge in the triazine ring. HMMM possesses three tertiary amino groups and C1 symmetry. Both factors render the HMMM center partially electron deficient. Synthesis of graphene-HMMM composites requires weak interaction between individual HMMM molecules in the bulk phase. Above 10 to 30 g/L, HMMM forms microemulsion droplets which are thermodynamically stable. Below 10 g/L HMMM forms emulsion droplets only. Ultrasonic treatment of graphite in HMMM emulsions causes a fine distribution of HMMM throughout the suspension. The solved HMMM molecules interact with graphene which yields stable composite dispersions. The goal of this study is the synthesis and characterization of aqueous graphene-HMMM ($G\text{-}M^\ominus$) dispersions. Various analytical techniques are employed to characterize the morphology and the interaction mechanism of the nano composites.

5.2 EXPERIMENTAL

5.2.1 GRAPHENE-HMMM COMPOSITE SYNTHESIS

Graphene-HMMM were synthesized by means of ultrasonic exfoliation of graphite in HMMM emulsions. HMMM emulsions were prepared in concentrations up to 8 g/L. This range excludes the possibility of microemulsion droplets. In a typical procedure HMMM (Maprenal MF900w/95, INEOS Melamines) was mixed with water resulting in a slightly turbid emulsion. Following filtration (0.2 µm syringe filter, cellulose-acetate membrane, Minisart), graphite (10 mesh, Alfa Aesar) is suspended in the now transparent emulsions. The suspensions were ultrasonically treated for up to 5 hours (Sonocool, Bandelin, 45 W, 35 kHz). The reaction vessels were moved around every 30 minutes to increase exfoliation efficiency.

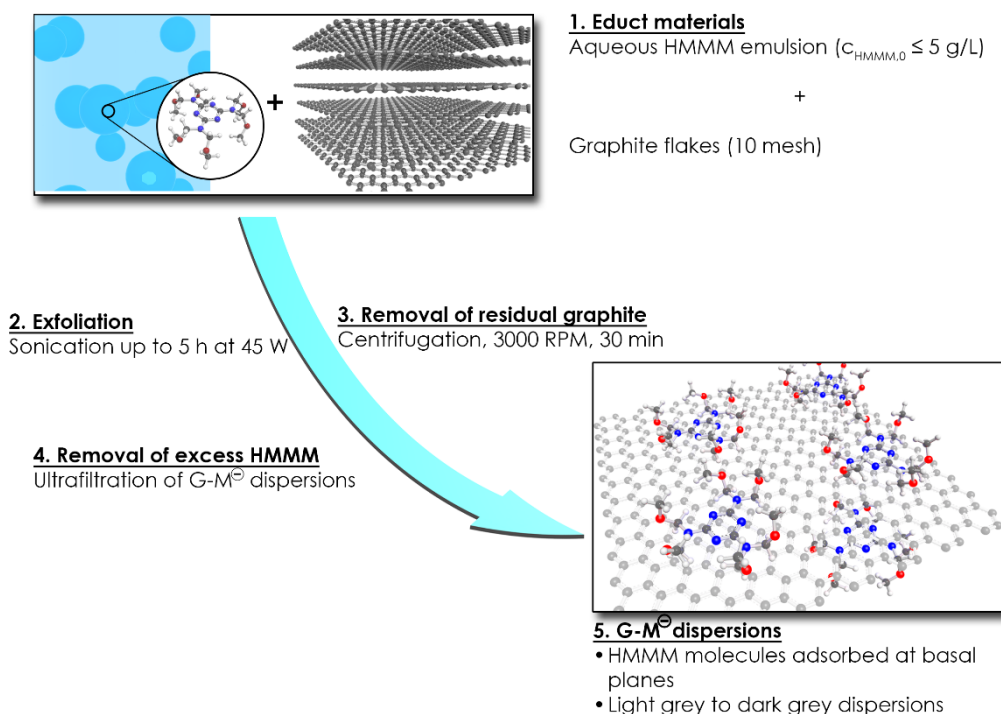


Figure 5.1: Ultrasonic exfoliation of graphite yielding G-M^\ominus

Residual graphite flakes were successively removed by mild centrifugation at 3000 rpm. Excess HMMM was subsequently removed by ultrafiltration. Depending on the concentration of dispersed graphene, the dispersions' color varied between light grey and black.

5.2.2 ANALYTICAL STUDIES

G-M^\ominus dispersions were characterized in terms of particle size, charge and structure via dynamic light scattering, zeta potential measurements (ZetaSizer Nano ZS, 633 nm, CONTIN algorithm, Malvern Instruments). Isoelectric titrations at pH values between 2 and 11 provide information about particle charge and stability. XRD measurements (Bruker D5005, Cu-K α 0.154 nm) were conducted in transmission geometry using self-crafted fluid cells at angles between 3 and 110 °2 Θ . Atomic force microscopy (Bruker Dimension Icon, Nanoscope V Controller, Peak Force Tapping mode) and scanning electron microscopy (Zeiss Neon 40, U = 3kV, d = 5 mm) experiments reveal particle dimensions and morphologies. Samples were prepared by spray coating G-M^\ominus onto silicon wafer substrates. Raman spectroscopy (Renishaw InVia, 2.33eV) provides information about graphene quality, degree of exfoliation and electronic properties. UV-VIS spectra were recorded between 220 and 700 nm (Evolution 600, Thermo Scientific, Wolfram and Deuterium lamp) to get insight into the particles' chemistry and the interaction mechanism. Further, UV-VIS was employed to determine the graphene content of the dispersions. In addition, FTIR spectra (Bruker Alpha P, λ = 633 nm) provide additional information about the particles' structure.

5.2.3 COMPUTATIONAL STUDIES

Density functional theory calculations were performed to gain insight into the structure and electronic states of HMMM. Geometric optimizations, electrostatic potentials and energy profiles were calculated using the Becke 3-parameter Lee-Yang-Parr (B3LYP) hybrid functional with a DNP+ basis set. A TS DFT-D correction was applied.

Adsorption calculations of HMMM on graphene provide information about the specific heat of adsorption and allow predictions about both composite structure and molecular compatibility. Adsorption calculations were performed on a graphene supercell (50 Å x 50 Å x 30 Å) using up to ten HMMM monomers. 10000 steps comprised each of the 10 heating cycles. The universal forcefield was used.

5.3 RESULTS

In order to gain insight into the exfoliation kinetics, G-M^\ominus dispersions were prepared in five different graphite/HMMM ratios. The exfoliation process was tracked via time-dependent UV-VIS measurements (660 nm) for up to five hours (figure 5.2a). Graphene concentrations were calculated using an extinction coefficient of $1390 \text{ Lg}^{-1}\text{m}^{-1}$ ^[169]. Both graphite and HMMM concentration have major influence on the exfoliation rate and the maximum graphene yield. Increasing HMMM concentration results in increasing graphene content. However, use of 0.2 g/L HMMM causes an asymptotic behavior due to depletion of stabilizer in presence of excess graphite. Higher concentrations result in an almost linear increase of graphene concentration with time. Excess graphite content (50 g/L) increases the exfoliation rate during the first hour and causes a higher degree of exfoliation. To determine the upper threshold of stable graphene content highly concentrated G-M^\ominus dispersions (up to 0.26 mg/ml graphene) were prepared by solvent extraction. The maximum concentration of single-layer graphene in G-M^\ominus was determined in a dilution series (figure 5.2b). The absorption remains constant until sufficient water is added for redispersion of flocculated sheets. The steep decrease after crossing the flocculation threshold shows nearly linear behavior. Dispersions containing graphene in concentrations above 0.043 mg/ml contain increasing amounts of flocculates and agglomerates which can be redispersed by adding additional water.

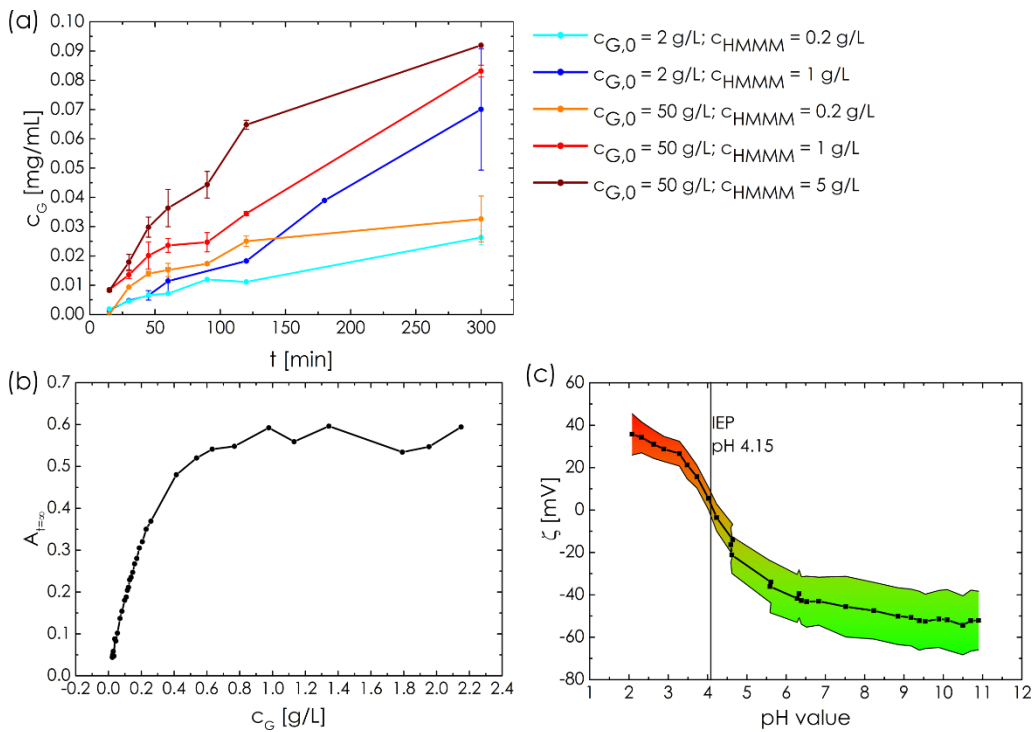


Figure 5.2: (a) Exfoliation kinetics of $G\text{-}M^\Theta$, inset shows UV-VIS spectra of graphite and $G\text{-}M^\Theta$; (b) dilution series of $G\text{-}M^\Theta$; (c) Isoelectric titration of $G\text{-}M^\Theta$ between pH 2 and 11

Isoelectric titrations between pH 2 and 11 yield information about particle charge and stability (figure 5.2c). Freshly prepared $G\text{-}M^\Theta$ dispersions exhibit pH values around 6.5 and show a negative zeta potential around -40 mV. The isoelectric point is at pH 4.2. The zeta potential decreases down to -60 mV with increasing pH value. The negative surface charge originates from HMMM adsorbed to graphene despite the fact that neither HMMM nor graphene possess functional groups capable of negative charge. The origin is a charge transfer-complex between graphene and HMMM (see below). Charge inversion beyond the IEP is possible to a certain extent. Positively charged $G\text{-}M^\Theta$ is stable between pH 3 and 3.5. The positive charge originates from protonation of HMMM methoxy groups. In this pH range, the negative charge of the triazine ring is masked by the positive charge of the protonated methoxy groups. Experimental data indicates that pH values below 3 result in rapid precipitation. Reasons for this

behavior are condensation reactions between adsorbed HMMM molecules and neutralization of the negative charge. In addition protonation of ring nitrogen may occur at very low pH values. Since there is no entropic stabilization the surface charge is a major contribution to the overall stability of the system.

In order to gain further insight into the adsorption mechanism, computational studies were performed to provide information on microscopic structure and electronic properties of HMMM (figure 5.3).

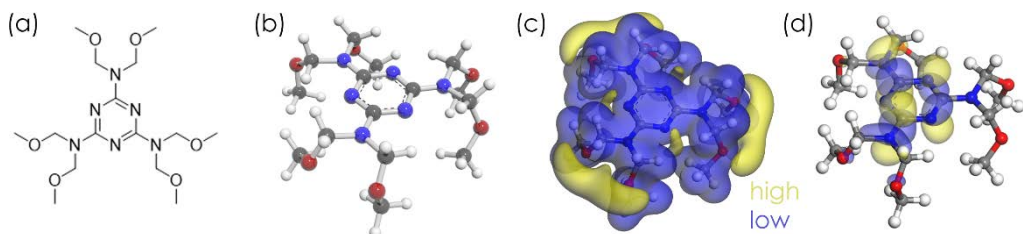


Figure 5.3: (a) Lewis structure of HMMM; (b) 3D representation of HMMM; (c) electrostatic potential map; (d) LUMO map

Adsorption simulations further indicated a negative differential adsorption energy of around -110 kcal/mol. In conjunction with structural properties obtained these calculation further provided a theoretical structural model for $G-M^{\ominus}$

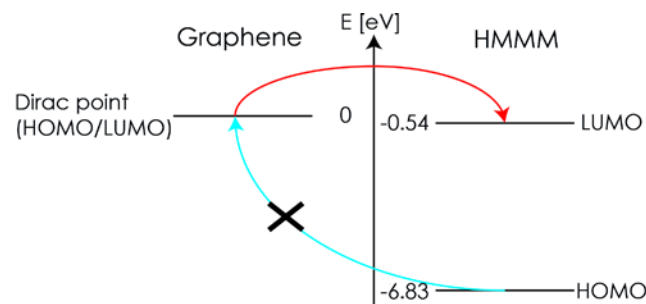


Figure 5.4: Energy diagram of graphene and HMMM

(cp. figure 5.8). The electron-withdrawing substituents of HMMM result in a partially electron-deficient triazine ring. Calculations were preformed within the density functional theory and result in LUMO and HOMO values at -0.54 eV and -6.83 eV, respectively. Based on these values and the observed negative zeta potentials, charge transfer between graphene and the LUMO of HMMM evidently contributes to the overall stability of the composite. The transfer of electrons from graphene to HMMM renders the graphene sheets p-doped. The

second major contribution arises from form a guest-host complexation due to aromatic π -stacking interactions. Both interaction mechanism have major impact on the electronic structure of graphene which is evident from spectroscopic analyses. FTIR spectra of HMMM and G-M $^\ominus$ show a high degree of similarity (figure 5.5b). The spectra consist of various HMMM ring vibrations and signals associated with C-O-C and C-N vibrational modes (table 5.1) [240, 241].

Table 5.1: FTIR bands of HMMM and G-M $^\ominus$; Abbreviations: oop: out of plane; sext.: sextant; quad: quadrant; str.: stretch; i-ph/o-ph: in/out of phase; semi: semi-circle; contr.: contraction

Vibration	$\bar{\nu}_{\text{HMMM}} [\text{cm}^{-1}]$	$\bar{\nu}_{\text{G-HMMM}} [\text{cm}^{-1}]$	$\Delta\bar{\nu} [\text{cm}^{-1}]$
Sext. oop bend	816	813	-3
C-O-C i-ph. str. + sext. oop bend	911	907	-4
Semi str. + exo C-N str. + (NCH ₂) ₂ i-ph. str.	1017	1005	-12
C-O-C o-ph. str.	1081	1075	-6
Quad str. + CNC o-ph. str.	1255	1248	-7
Semi str. + exo C-N contr.	1386	1380	-6
Quad str. + exo C-N contr.	1550	1545	-5

The triazine ring vibrations at 816 cm $^{-1}$, 911 cm $^{-1}$, 1017 cm $^{-1}$, 1255 cm $^{-1}$, 1386 cm $^{-1}$ and 1550 cm $^{-1}$ are red-shifted in G-M $^\ominus$ which is attributed to softening of the triazine core caused by electron transfer from graphene to HMMM. The increase in total electron density has influence on HMMM functional groups as well. While C-N vibrations cannot be distinguished from ring vibrations, the C-O-C out of phase stretching vibration of the electron withdrawing methoxy groups at 1081 cm $^{-1}$ is isolated and exhibits a measureable red-shift due to the overall increased electron density. The UV-VIS spectrum of HMMM consists primarily of C=N, NR₂ and ROR n- π^* n- σ^* and π - π^* transitions (figure 5a). Accordingly, the molecule absorbs over a wide range of the UV spectrum. The C=N π - π^* transition comprises the right absorption edge. Graphene usually shows strong C=C π - π^* transitions around 270 nm and more or less intensive absorption over the whole spectrum. G-M $^\ominus$ shows strong hypsochromism

$(\Delta\lambda_{\max} = 28 \text{ nm})$ and hypochromism (80% at 237 nm) with an absorption edge around 260 nm. Both HMMM and graphene transitions are greatly affected. The spectrum is clearly influenced by the CT complexation between graphene and HMMM resulting in the considerable blue-shift. The accompanied hypochromic effect is characteristic for π - σ interactions.

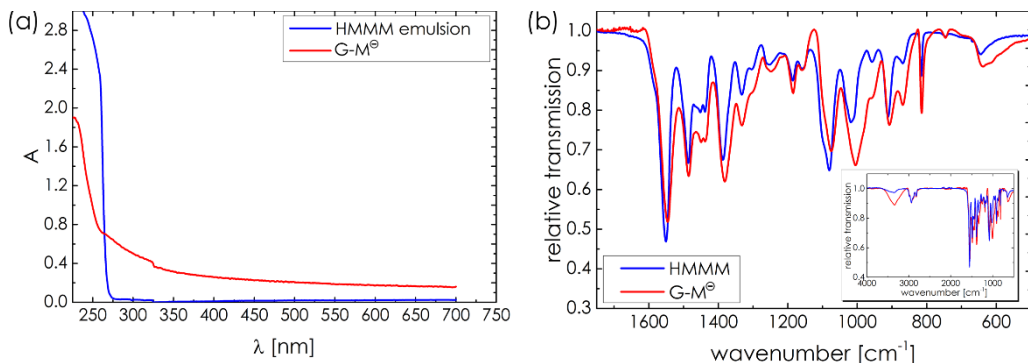


Figure 5.5: (a) UV-VIS spectra of aq. HMMM and G-M^{\ominus} ; (b) FTIR spectra of HMMM and G-M^{\ominus}

Raman spectroscopy was conducted to get information about the degree of exfoliation, the quality of the graphene flakes and the electronic structure of G-M^{\ominus} (figure 5.6). The graphite spectrum shows D and G modes at 1350 cm^{-1} and 1580 cm^{-1} . The D band originates from a second-order process involving one iTO (inplane Transverse Optic) phonon and a defect thus is a measure for crystal lattice defects. The D band is not evaluable owing to the high absorption of HMMM in this range of the spectrum. As stated in the theoretical part the Raman G band originates from a doubly degenerate phonon mode (E_{2g}) at the Brillouin zone center, thus is sensitive to softening of stiffening of the crystal lattice. The second order G' band around 2700 cm^{-1} involves two iTO modes. Both G and G' band are highly sensitive indicators for changes in the electronic structure of carbon materials and provide evidence for degree of graphene exfoliation. The G band is slightly red-shifted (2 cm^{-1}) and its full width at half maximum (FWHM) increases from 16 to 20 cm^{-1} . Both results indicate chemical p-doping of graphene by the electron-accepting triazine ring of HMMM. In order

to evaluate the G' peaks of graphite and G-M[⊖] a multi-lorentzian fit was used. Graphite shows major signals at 2676 cm⁻¹ and 2719 cm⁻¹. The shape is characteristic for the multi-layered structure of graphite. The G' band of G-M[⊖] consists of two major and some smaller signals as well. The signal at 2684 cm⁻¹ is associated with the second-order phonon process of undoped graphene. The strongly blue-shifted band at 2728 cm⁻¹ and the fairly low G'/G peak aspect ratio account for p-doping as well.

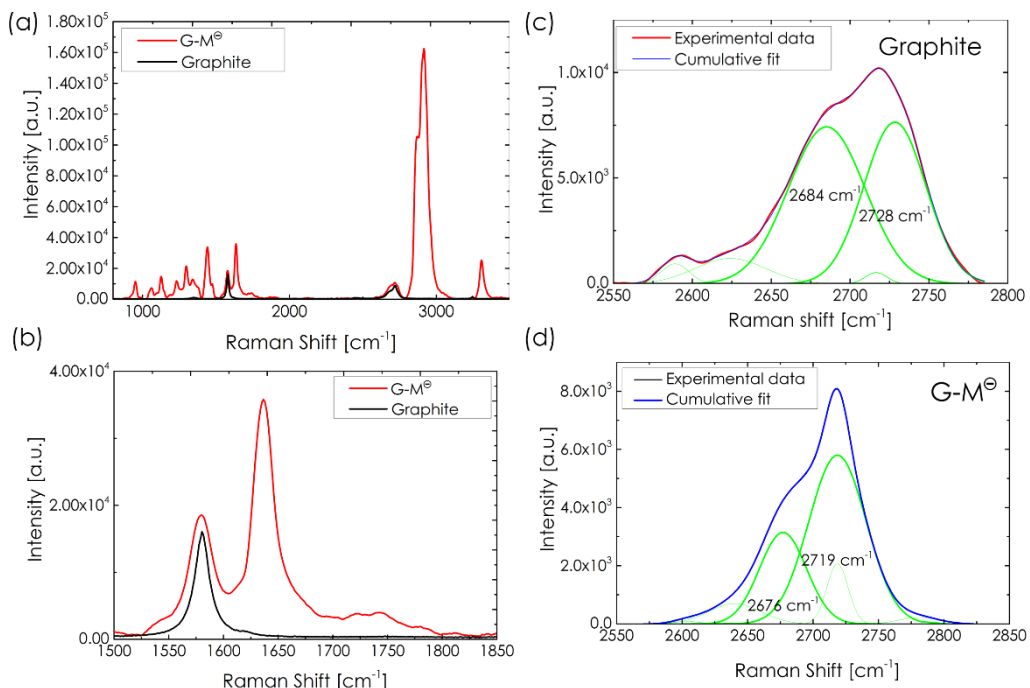


Figure 5.6: Raman spectra of G-M[⊖]; (a) full spectra of G-M[⊖] and graphite; (b) G band; (c) G' band of graphite; (d) G' band of G-M[⊖]

To conclude the spectroscopic results, charge transfer interactions between graphene and HMMM results in p-doping of graphene. Further, the obtained FTIR and UV-VIS spectra substantiate the assumption that π -stacking interactions play an important role as well. XRD patterns of graphite, HMMM emulsions and G-M[⊖] provide further information about degree of exfoliation and structural features (figure 5.7). The graphite spectrum shows discrete d₀₀₂,

d_{010} and d_{100} peaks at 26.48, 42.29 and 77.46 $^{\circ}2\Theta$. The HMMM spectrum shows d_{010} , d_{100} and d_{001} peaks at 22.54, 34.55 and 27.99 $^{\circ}2\Theta$, respectively. $G-M^{\ominus}$ does not exhibit any remaining graphite peaks while the HMMM signals persist.

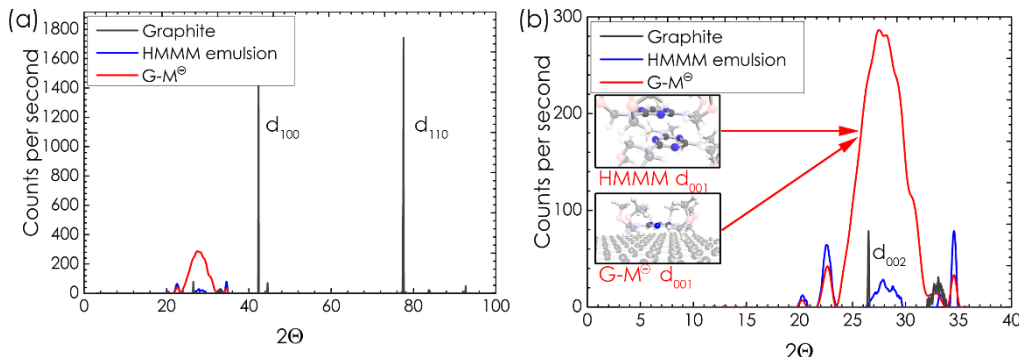


Figure 5.7: (a) XRD spectra of graphite, aqueous HMMM and $G-M^{\ominus}$; (b) magnification of mid-angle range

The large peak around 28 $^{\circ}2\Theta$ includes signals from HMMM d_{001} , $G-M^{\ominus} d_{001}$ and graphene d_{002} . All included signals account for stacking of HMMM and graphene either with each other or the respective other species. XRD spectra were recorded in transmission geometry using a highly concentrated $G-M^{\ominus}$ dispersion. Flocculation and re-agglomeration occur at graphene concentrations exceeding 43 $\mu\text{g}/\text{ml}$. The observed graphene d_{002} peak thus originates from re-stacked $G-M^{\ominus}$. Morphological studies were conducted via dynamic light scattering, atomic force microscopy and scanning electron microscopy (figure 5.8).

$G-M^{\ominus}$ exhibits hydrodynamic diameters between 50 and 900 nm with an average around 300 nm. AFM measurements correlate closely with these values. The cross-section shows a single particle with a diameter of 290 nm and average height of 1.7 nm. The height corresponds to a graphene sheet with HMMM adsorbed to both sides. Despite the post-treatment some extremely large sheets were observed as well (not shown). These sheets are several microns in diameter and could not be removed by filtration (1.2 μm). This result emphasizes the

highly flexible structure of the nano composites. SEM images of vacuum filtered G-M^\ominus films confirm the determined diameters. Calculation of diameter/height aspect ratio yields values up to 600.

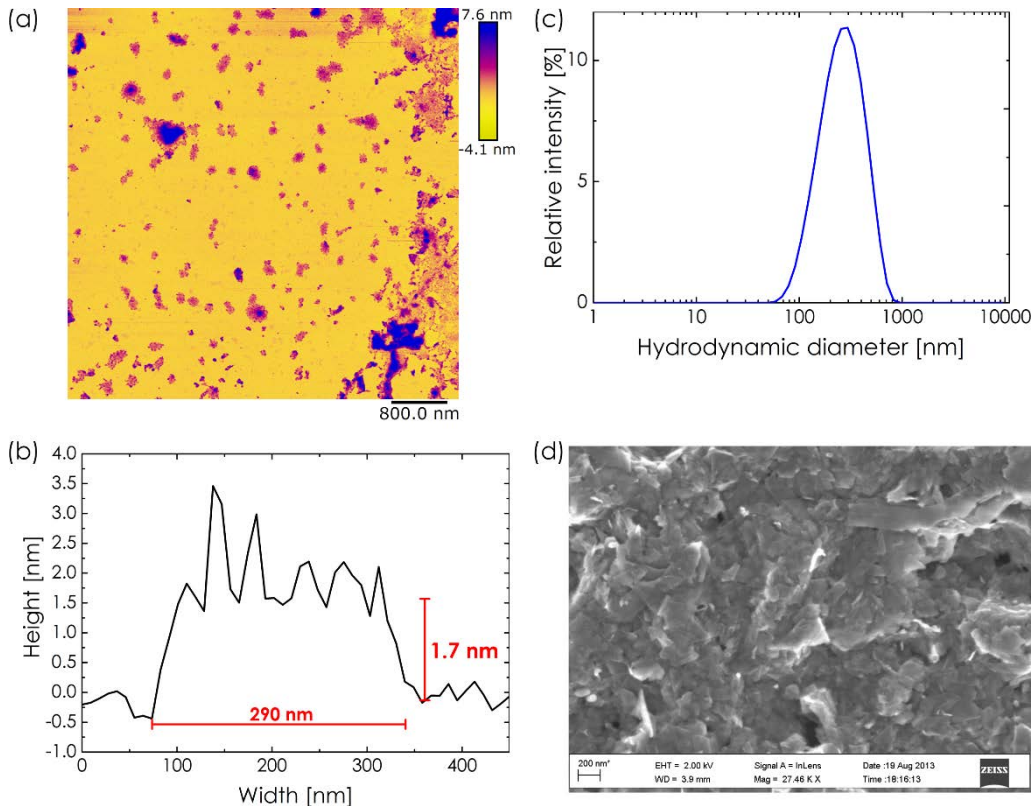


Figure 5.8: (a) AFM image of G-M^\ominus ; (b) cross-section of a single particle; (c) hydrodynamic diameters of G-M^\ominus ; (d) SEM image of vacuum dried G-M^\ominus film

In consideration of all presented results a structural model of G-M^\ominus is developed which includes the underlying stabilization mechanisms (figure 5.9). The electron-accepting triazine core of HMMM adsorbs to graphene's basal planes in an offset face-to-face fashion. Energetic contributions to the high stability of the nano composite arise from π -stacking interactions and charge transfer interactions. The methoxy groups of HMMM point away from the graphene surface and are accessible for protonation. Lowering the dispersions' pH value

causes protonation of the methoxy functions. The positive charge masks the negative charge from the CT which is still present at this point.

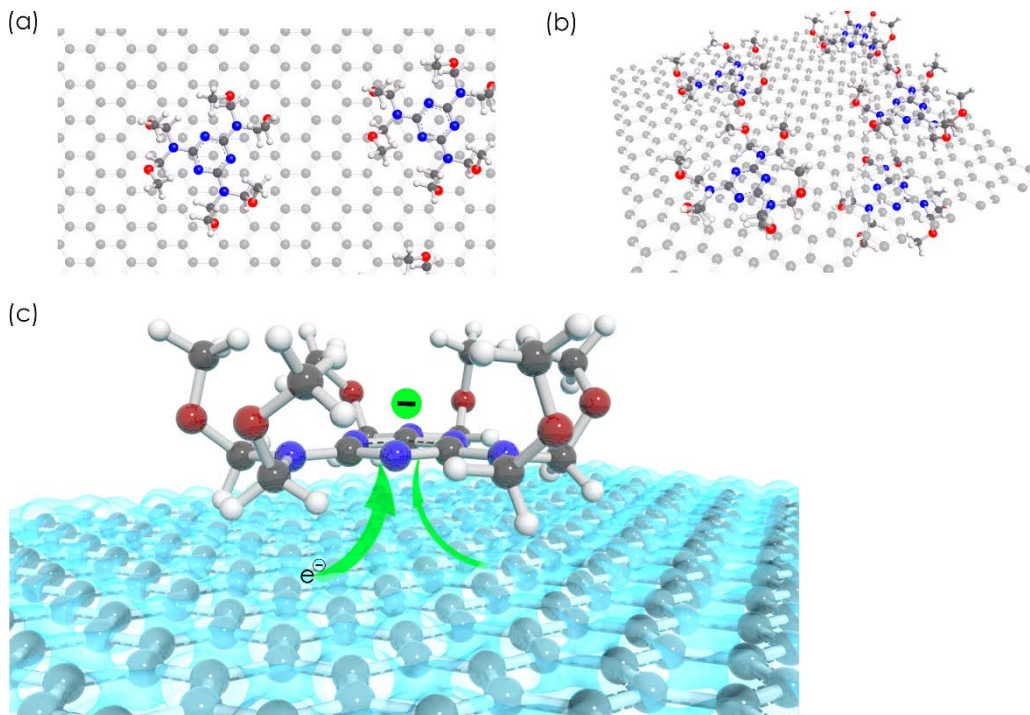


Figure 5.9: (a) Top view and (b) perspective view of $G\text{-}M^\Theta$; (c) Charge transfer from graphene to HMMM resulting in total negative charge of the nano composite

Even lower pH values disrupt the charge transfer and destabilize the system. In addition to HMMM self-condensation reactions protonation of the triazine ring may occur as well which would inhibit both π -stacking interactions and the charge transfer.

5.4 SUMMARY AND CONCLUSION

Aqueous graphene-hexamethoxymethyl melamine dispersions (G-M^\ominus) were successfully synthesized in concentrations of up to 43 $\mu\text{g/ml}$. The composite particles exhibit diameters between 50 and 900 nm and heights around 1.7 nm. The native dispersions are stable for several weeks before slow aggregation occurs. Unaltered G-M^\ominus exhibit negative charge which originates from charge transfer from graphene to adsorbed HMMM. The effect is facilitated by π -stacking interactions. Spectroscopic results provide evidence for the existence of both mechanisms. Computational studies revealed suitable energy levels of HMMM to form charge transfer complexes with graphene. Charge inversion yielding positively charged dispersions is possible around pH 3.5. Lower values cause rapid precipitation of the dispersions. Based on the experimental findings, a structural model of G-M^\ominus was developed. Both the variable surface charge and the p-doped nature of the graphene render the composite particle dispersions excellent candidates for various applications, foremost processing of transparent conductive films (TCFs).

Chapter VI

AQUEOUS GRAPHENE HMMM NANO PARTICLE COMPOSITE DISPERSIONS

6.1 INTRODUCTION

Aqueous graphene composite dispersions are the primary building blocks for applications like graphene thin films or polymer composites. Several compounds are capable to stabilize graphene in water. However, composites consisting of graphene and organic nano particles are rare. HMMM nano particle dispersions (MP) possess several properties which make them suitable for synthesis of aqueous graphene composite dispersions. The particles are positively charged and long-term stable. Secondly, the particles diameter and shape can be adjusted over a wide range. Further, MP possess a highly rigid structure and can improve hardness in polymeric systems while retaining the flexibility. HMMM monomers interact primarily via charge transfer with the graphene surface. The MP surface consists of condensed HMMM but is different from the respective monomers; it is covered with ternary hydrogen bridges which are the origin of the positive charge. The charged groups can interact with the electron-rich graphene surface via cation- π interactions. Preliminary results showed that MP based graphene dispersions (G-MP $^{\oplus}$) are positively charged and long-term stable.

The goal of this study is the synthesis and characterization of G-MP $^{\oplus}$. Emphasis lies on the structure and morphology of the composite nano particle dispersions.

6.2 EXPERIMENTAL

6.2.1 SYNTHESIS OF NANO COMPOSITES

G-MP^\oplus dispersions were synthesized by mild ultrasonic treatment of graphite in aqueous HMMM nano particle dispersions. The initial graphite concentration was chosen to be 50 g/L. Several types of MP with varying particle diameter were used. Preliminary results indicated that MP concentration is not a critical factor in the synthesis hence for structural and morphological studies was adjusted to 25 g/L. In a typical procedure, graphite and MP were mixed at room temperature. Ultrasonic exfoliation was performed under mild conditions (Sonocool, Bandelin, 45 W, 35 kHz) for five hours. The reaction vessels were moved around every 30 minutes to increase efficiency.

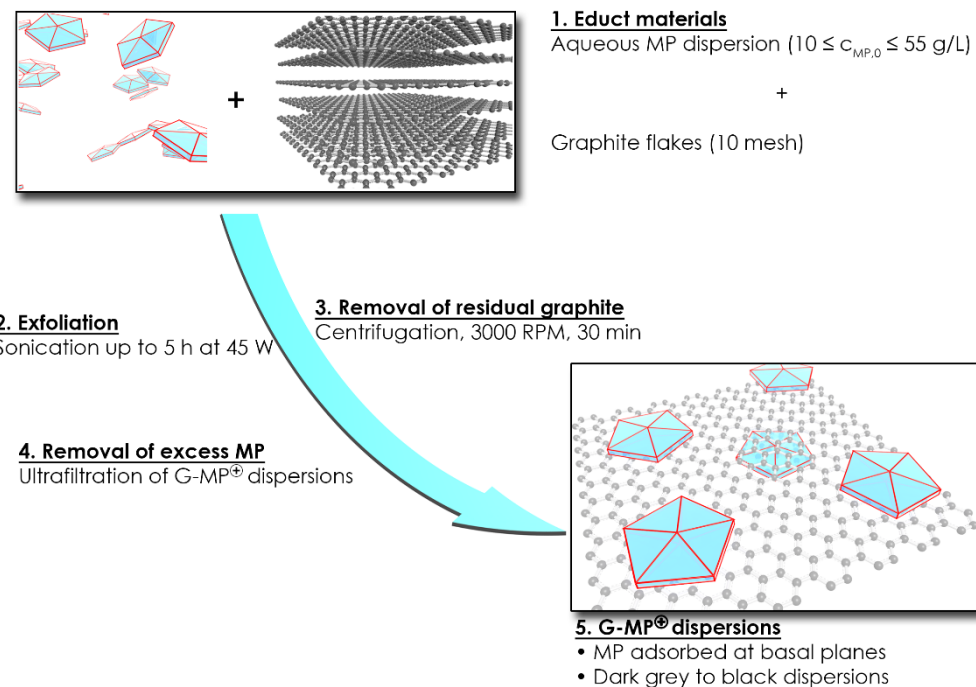


Figure 6.1: Ultrasonic exfoliation of graphite in MP yielding G-MP^\oplus

Successive removal of residual graphite flakes was done via mild centrifugation at 3000 rpm. Excess MP was removed by ultrafiltration. G-MP[⊕] dispersions are dark grey to black in color.

6.2.2 ANALYTICAL STUDIES

Liquid G-MP[⊕] dispersions were characterized in terms of particle size, stability and structure via dynamic light scattering, zeta potential measurements (ZetaSizer Nano ZS, 633 nm, Malvern Instruments). Isoelectric titrations at pH values between 2 and 11 provide information about particle charge and stability. XRD measurements (Bruker D5005, Cu-K_α 0.154 nm) were conducted in transmission geometry using self-crafted fluid cells at angles between 3 and 110 °2θ. Atomic force microscopy (Bruker Dimension Icon, Nanoscope V Controller, Peak Force Tapping mode) and scanning electron microscopy (Zeiss Neon 40, U = 3kV, d = 5 mm) experiments reveal particle dimensions and morphologies. Samples were prepared by spray coating G-MP[⊕] onto silicon wafer substrates. Raman spectroscopy (Renishaw InVia, 2.33eV) provides information about graphene quality, degree of exfoliation and electronic nature. UV-VIS spectra were recorded between 220 and 700 nm. (Evolution 600, Thermo Scientific, Wolfram and Deuterium lamp) to get insight into the hybrid particles' chemistry and interaction mechanism. In addition, FTIR spectra (Bruker Alpha P, λ = 633 nm) provide further information about both subjects.

6.3 RESULTS

G-MP[⊕] nano composites have been characterized with respect to charge, stability, size, structure and morphology. Graphene concentrations were determined by UV-VIS spectroscopy at 660 nm using an absorption coefficient of 1390 Lg⁻¹m⁻¹ and yielded up to 80 µg/mL. The overall concentration of the hybrid material was 20 mg/mL due to high amounts of adsorbed MP. Isoelectric titration measurements show that G-MP[⊕] exhibit an isoelectric point at pH 10.9 (figure 6.2). Up to a pH value of 9 the zeta potential is constant around +45 mV which indicates high stability.

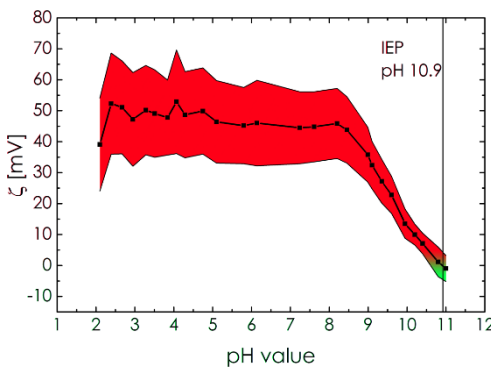


Figure 6.2: Isoelectric titration of G-MP[⊕] between pH 2 and 11

Precipitation at pH values between 2.5 and 9 was not observed. Above pH value 9 the dispersions precipitate rapidly due to decreasing electrostatic repulsion. Charge inverted dispersions above pH 11 destabilize almost immediately. The nature of MP charge carriers causes the instability. The positive surface charge of MP originates from double dimethylene ether bridges of MP. The HMMM molecule itself does not possess functional groups capable of exhibiting negative charge. Charge beyond pH 11 has to originate from adsorption of hydroxide or residual chloride ions. The decrease in zeta potential below pH 2 is accounted for by the increasing conductivity of the dispersion which seizes the electrostatic double layer. Due to the rigidity of MP and the high surface coverage, additional

stabilizing mechanism like entropic stabilization are excluded. Characterization of particle size and morphology is performed via SEM, AFM and DLS (figure 6.4). The average diameter of G-MP^\oplus ranges between 50 nm and 1 μm . Larger flakes were not observed. AFM height measurements reveal an average height of 10-15 nm. Considering MP diameters of 5-10 nm, this corresponds to MP adsorbed to both sides of one graphene sheet. Consequently samples show diameter/height aspect ratios up to 100. The cross-section shows that MP is not adsorbed vicinal to the graphene surface. Due to electrostatic repulsion between individual MP the particles are offset from neighboring particles on the same side and particles adsorbed to the opposite side of a graphene sheet.

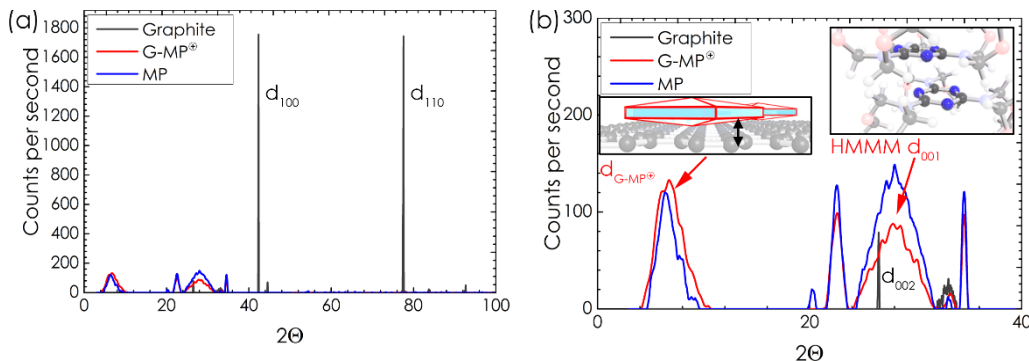


Figure 6.3: XRD patterns of graphite, MP and G-MP^\oplus ; (a) total spectra and (b) magnification of angles 0 to 40 $^{\circ}2\Theta$

XRD patterns of G-MP^\oplus confirm this result (figure 6.3). The graphite spectrum shows sharp d_{002} , d_{100} and d_{110} peaks at 26.48, 42.29 and 77.46 $^{\circ}2\Theta$, respectively. MP shows relatively broad d_{100} , d_{110} and d_{001} peaks at 22.54, 34.55 and 27.99 $^{\circ}2\Theta$. Further, G-MP^\oplus and MP show a characteristic peak at 6.4 $^{\circ}2\Theta$ which is attributed to the particles' dimensions. G-MP^\oplus shows no remaining graphite peaks which leads to the conclusion that graphite is completely exfoliated into graphene sheets.

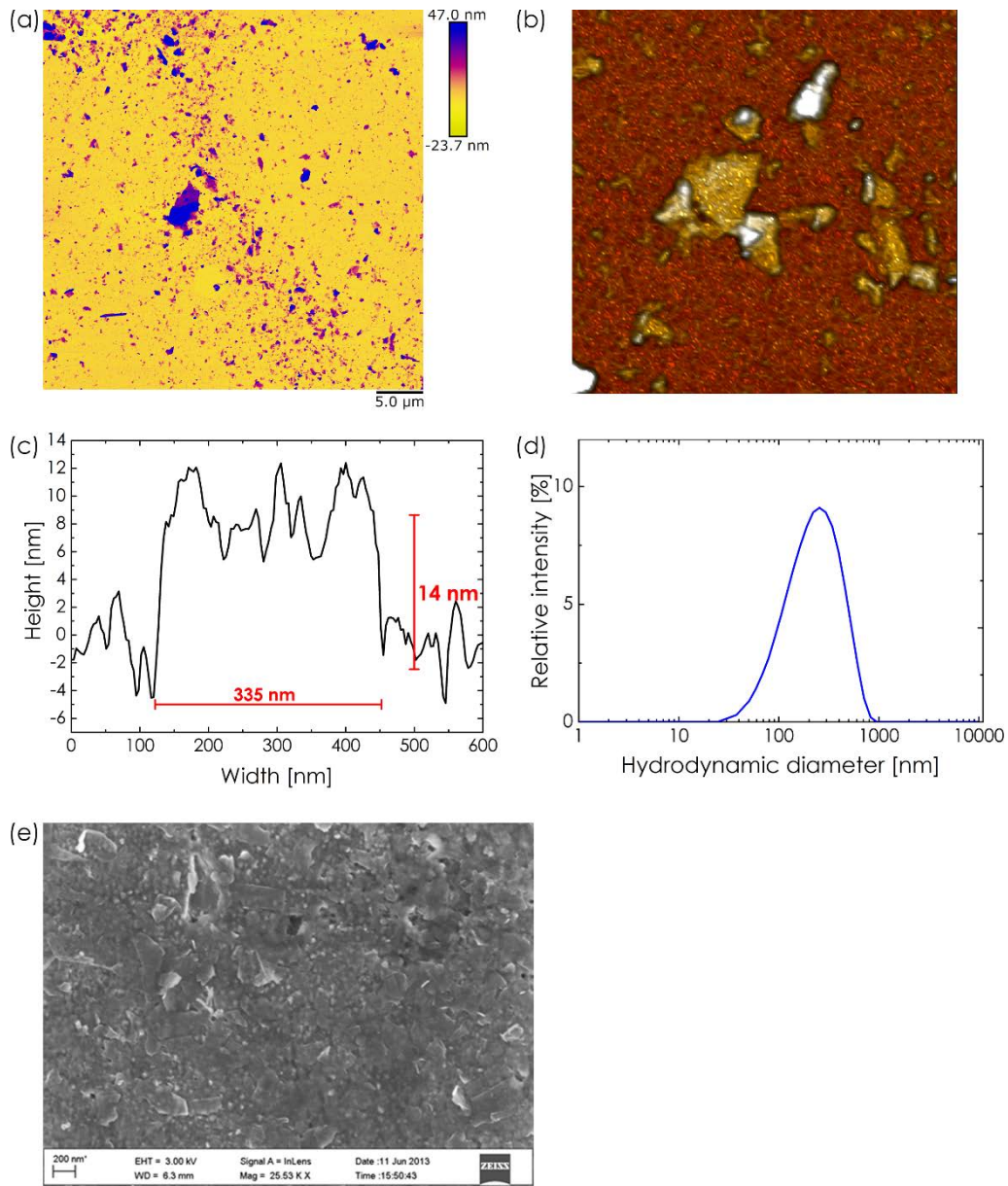


Figure 6.4: (a) AFM image of G-MP[⊕]; (b) AFM image and 3D image showing MP adsorbed to graphene; (c) cross-section of a single particle; (d) hydrodynamic diameters of G-MP[⊕]; (e) SEM image of vacuum dried G-MP[⊕] film

The broad peak around $27.5^\circ 2\Theta$ which could refer to re-stacked graphene even decreases in intensity hence is solely attributed to crystalline HMMM present in MP. The MP d_{010} and d_{001} peaks show less intensity while their angle remains

unchanged. Since there is some change in the MP size peak, it was used as basis for calculation of the crystallite size via the Scherrer equation (equation 6.1).

$$\tau = \frac{K\lambda}{\beta \cos \theta} \quad (6.1)$$

Crystallite domain sizes τ were calculated using a shape factor K of 0.9 and the X-ray wavelength λ of 0.154 nm. The full width at half maximum (FWHM) β and the Bragg angle were determined from the respective peak. The crystallite size difference between G-MP $^\oplus$ and MP is 0.5 nm which corresponds to a single graphene layer. The determined crystallite size (8.5 nm) provides further evidence of offset stacking of MP on graphene. Oppositely adsorbed MP would result in higher values.

Raman measurements provide information about the degree of exfoliation, the quality of the graphene sheets and the electronic nature (figure 6.5c). The graphite G- and D-band at 1566 cm $^{-1}$ and 1350 cm $^{-1}$ interfere with MP signals thus provide little information about disorder in the sp 2 structure. The G-MP $^\oplus$ G' band at 2684 cm $^{-1}$ is isolated and allows some conclusions. The G' band is attributed to second-order iTO (in-plane, Transversal, Optical), phonons near graphene's Dirac point. The single-lorentzian shape of the peak indicates single-layer graphene (SLG). The full width at half maximum (FWHM) of 60 cm $^{-1}$ is higher than expected for SLG. In conjunction with the lower intensity both observations indicate chemical doping of graphene. This is confirmed by spectroscopic evidence for ternary hydrogen bridges between MP and graphene.

UV-VIS and FTIR spectra (figure 6.5) provide information about the stabilization mechanism of G-MP $^\oplus$. Both MP and G-MP $^\oplus$ show strong absorption in the UV region of the spectrum. Characteristic absorption of graphene in the visible range of the spectrum provides information about graphene content. UV-VIS spectra show a blue-shift $\Delta\lambda_{\max} = 5.2$ nm (around 270 nm) in G-MP $^\oplus$ compared to MP. MP oxygen interacts with ternary bound

protons between MP and graphene causing a shift of the $n-\pi^*$ band to lower wavelengths. Aromatic $\pi-\sigma$ interactions in contrast would cause red shifting of the spectrum. These results show that cation- π interactions are stronger than π -stacking. Evidence for charge-transfer interactions was not observed. Further, the spectrum lacks characteristic C=O $n-\pi^*$ bands at 300 nm indicating that graphene was not oxidized during the exfoliation process.

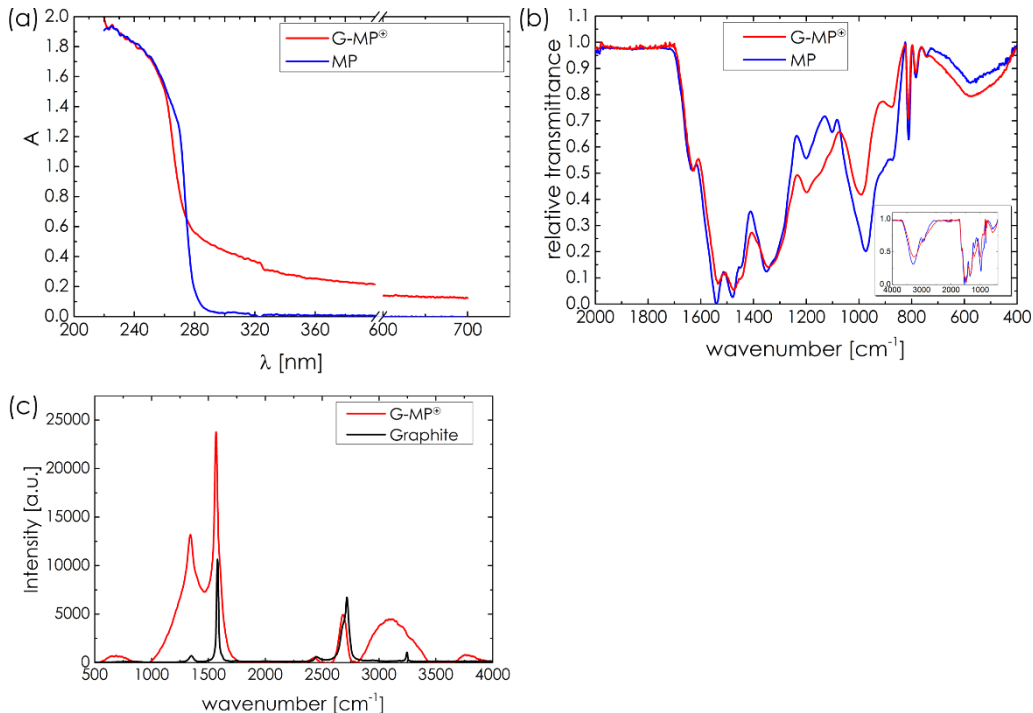


Figure 6.5: (a) UV-VIS spectra of MP and G-MP[⊕]; (b) FTIR spectra of MP and G-MP[⊕], inset shows full spectrum; (c) Raman spectra of graphite and G-MP[⊕]

Infrared spectra of G-MP[⊕] and MP show several vibrational combinations between triazine ring-, CH₂-, C-N and C-O-C vibrations (figure 6.5b, table 6.1). The C-O-C stretching band of MP is found at 973 cm⁻¹. This band is blue-shifted (20 cm⁻¹) in G-MP[⊕]. The shift is caused by formation of a ternary hydrogen bond between the double dimethylene ether bridge of MP and the π -electron system of graphene. Triazine sextant out of plane vibrations at 783 cm⁻¹ and 810 cm⁻¹ as well as ring breathing vibrations at 873 cm⁻¹ show no deviation in G-MP[⊕].

However, semi-circle and quadrant stretching vibrations at 1350.5 cm^{-1} , 1479 cm^{-1} and 1541 cm^{-1} are slightly shifted to lower wavenumbers, which indicates aromatic interactions between the outer shell of MP and graphene basal planes.

Table 6.1: Selected infrared vibrations of MP and G-MP $^\oplus$; Abbreviations: oop: out of plane; sext.: sextant; quad: quadrant; str.: stretch; i-ph/o-ph: in/out of phase; semi: semi-circle; contr.: contraction

Vibration	$\bar{\nu}_{\text{HNPD}} [\text{cm}^{-1}]$	$\bar{\nu}_{\text{Graphene-HNPD}} [\text{cm}^{-1}]$	$\Delta\bar{\nu} [\text{cm}^{-1}]$
Sext. oop bend	783	783	0
Sext. oop bend	810	810	0
Ring breath	873	874	0
C-O-C asym stretch	973	992.5	20
CH ₂ rk. Sym to COC plane + Semi str.	1198.5	1198.5	0
Semi str. + CH ₂ twist+C-O-C sym	1350.5	1342.4	8
Semi str.+exo C-N contr.	1479	1475	4
Quad str. + CH ₂ open + exo C-N contr.	1541	1534	7
Exo C-N inphase stretch	1629	1629	0

Figure 6.6 illustrates the structure and the underlying stabilization mechanisms of G-MP $^\oplus$. Vis-à-vis adsorbed particles are offset due to electrostatic repulsion. The high stability of is explained by the underlying interaction between MP

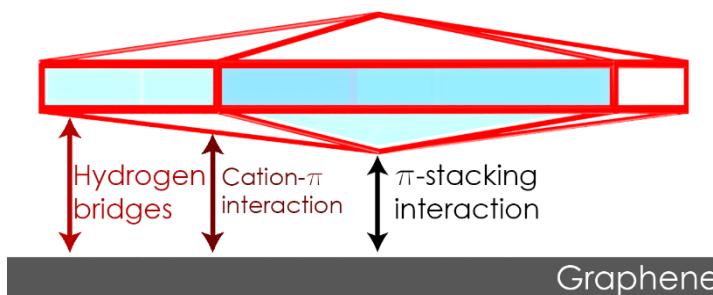


Figure 6.6: Interaction mechanisms in G-MP $^\oplus$

surface and the graphene sheets. Based on the spectroscopic results the stability originates from cation- π interactions, ternary

hydrogen bonds and π -stacking. The magnitude of cation- π interactions and H-bonding depends on the actual distance between the MP surface and graphene.

6.4 SUMMARY AND CONCLUSION

Aqueous non-covalently functionalized graphene-MP hybrid dispersions ($G\text{-}MP^\oplus$) were successfully synthesized by ultrasonic exfoliation. Graphene concentrations up to 0.8 mg/ml were realized. The particles are several hundred nanometers in diameter and a few nanometers in height, resulting in high diameter/height aspect ratios. Particle height primarily depends on MP diameter.

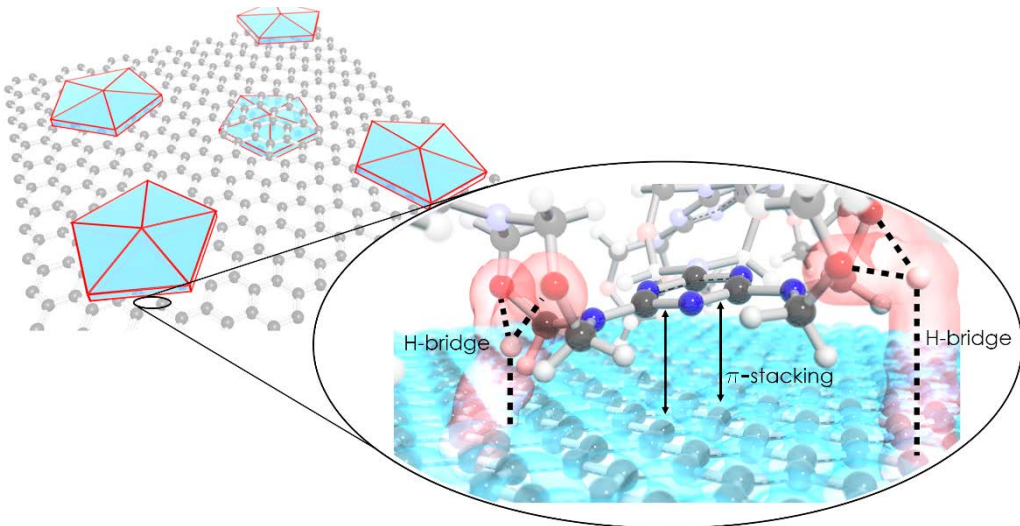


Figure 6.7: Structure of $G\text{-}MP^\oplus$

The dispersions consist of single graphene layers with MP adsorbed to both sides. Intercalated graphite compounds were not detected. $G\text{-}MP^\oplus$ are stable for months and exhibit positive surface charge between pH 2 and 10. Charge inversion is not possible due to the lack of potential negative charge carriers. Inverted dispersions precipitate rapidly. The particles' charge carriers are double dimethylene ether bridges of adsorbed MP. The complex adsorption mechanism consists of cation- π , ternary hydrogen bonds and aromatic π -stacking interactions. Potential applications of $G\text{-}MP^\oplus$ are manufacture transparent conductive films (TCFs) and conductive graphene-polymer composites.

Chapter VII

ELECTRODEPOSITION OF FUNCTIONALIZED GRAPHENE DISPERSIONS

7.1 INTRODUCTION

Electrodeposition (ED) is a versatile method for graphene thin film manufacture. The graphene composites G-MP^{\oplus} and G-M^{\ominus} exhibit the necessary charge for cathodic and anodic electrodeposition. Compared to other techniques ED is a very fast process. The main challenge is controlling the process parameters deposition voltage and deposition time which are the primary parameters for control over film thickness. Further variables include the general experimental setup and the properties of the particle dispersions. In contrast to spherical particles, graphene dispersion contain highly anisotropic particles which influences the deposition kinetics and the appearance of the films. G-MP^{\oplus} is deposited via cathodic electrodeposition (C-ED). The process follows a complex mechanism which leads to intriguing film morphologies. Due to the sandwiched structure of the nano composites the resulting films show interesting electrical properties. This chapter will elaborate the kinetics and the deposition mechanism of G-MP^{\oplus} electrodeposition. The films are characterized regarding surface structure and electrical properties.

7.2 EXPERIMENTAL

7.2.1 ELECTRODEPOSITION EXPERIMENTS

G-MP[⊕] was electrodeposited on ITO coated glass substrates using a palladium counter electrode in plate-to-plate geometry (figure 7.1).

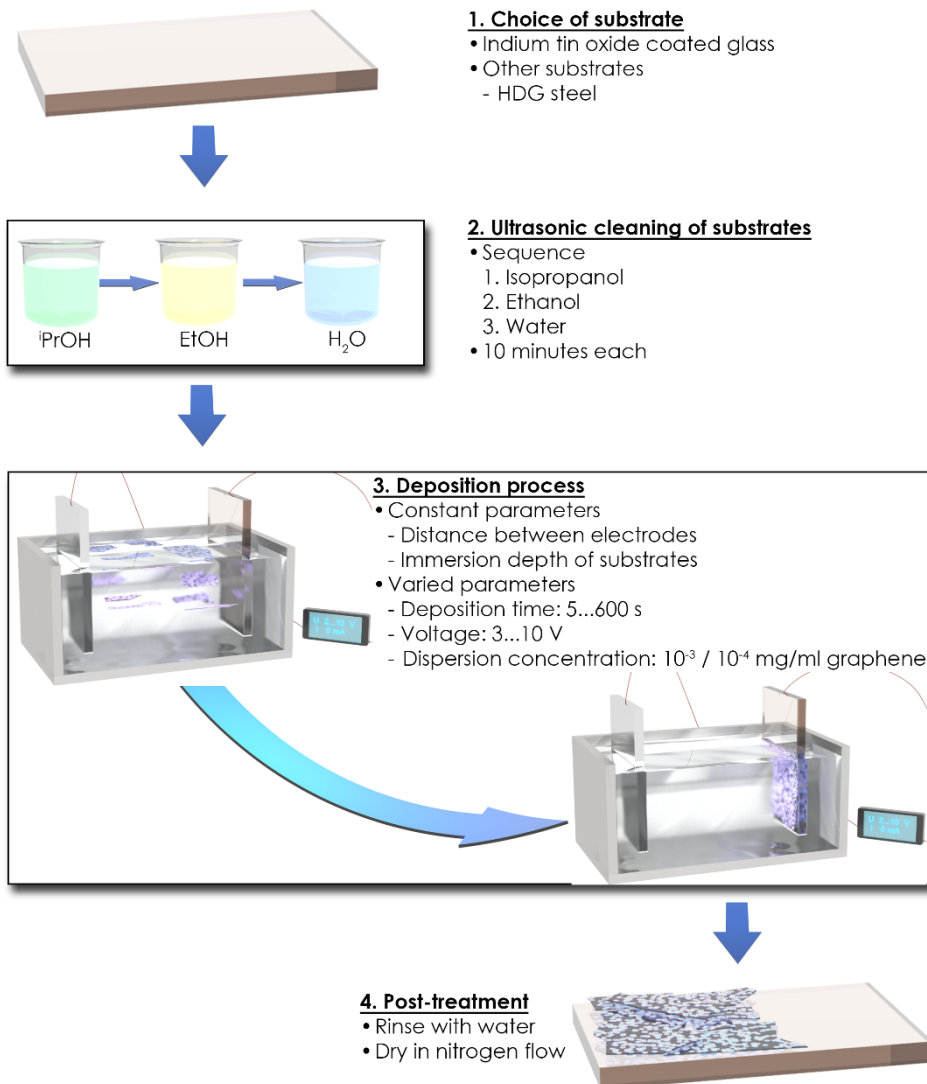


Figure 7.1: Process scheme for C-ED of G-MP[⊕]

The distance between the electrodes was 5 cm. The substrates were cleaned by ultrasonic treatment in a sequence of isopropanol, ethanol and water and were subsequently dried in a nitrogen flow. G-MP[⊕] dispersions were synthesized according to chapter 6. The dispersions were diluted with water to yield two concentrations, $5 \cdot 10^{-4}$ mg/ml and $5 \cdot 10^{-3}$ mg/ml. C-ED experiments were conducted at voltages between 2 and 10 V for 5 to 600 s. Additional experiments to determine the voltage and time limits were conducted as well. To include the three process parameters voltage, time and graphene concentration the obtained films are denoted as *C-ED_U-t-c*, e.g. *C-ED_10-120-10⁻⁴*.

7.2.2 ANALYTICAL STUDIES

The deposition kinetics of G-MP[⊕] was monitored by means of UV-VIS (Evolution 600, Thermo Scientific, wolfram lamp). The transmission values at a wavelength of 600 nm were determined and correlated with SEM thickness measurements (Zeiss Neon 40, U = 3 kV, d = 5 mm). Graphene absorbs electromagnetic radiation over the whole UV-VIS spectrum whereas HMMM and MP only absorb in the UV region of the spectrum. Hence, the amount of deposited graphene is directly proportional to the transmittance at optical wavelengths. Cross-referencing of the samples yielded a correlation factor of $11.58 \pm 1.5 \text{ nm} \cdot \text{T}$.

The morphologies of the resulting films were characterized via AFM (Bruker Dimension Icon, Nanoscope V Controller, Peak Force Tapping mode) and SEM. AFM was primarily conducted to visualize the surface structure of the films. *C-ED_U-5-c* and *C-ED_U-10-c* samples *prima facie* are difficult to interpret since the height difference between individual graphene sheets is extremely low compared to the overall height profile of the images. Several graphical filters have been applied to increase graphene visibility.

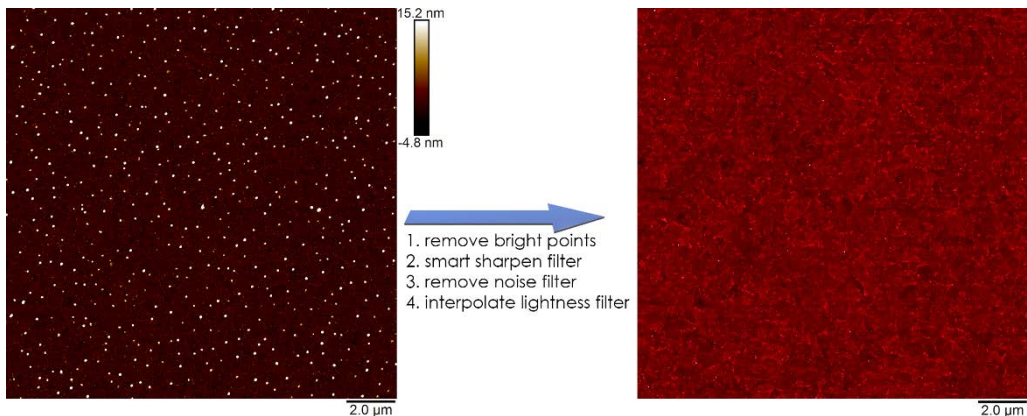


Figure 7.2: AFM image processing to reveal graphene substructure (C-ED_10-5- 10^4)

Additional nanomechanical analyses via AFM (HarmoniXTM) yield information about material differences at the surface. Conductivity measurements of G-MP[⊕] films were performed in four point probe geometry using a current of 1 mA.

7.3 RESULTS

Cathodic electrodeposition (C-ED) of G-MP[⊕] was conducted in constant voltage mode on ITO coated glass substrates. The MP utilized for G-MP[⊕] synthesis was adjusted to contain primary particles with diameters between 5 and 15 nm. Larger MP may hinder graphene percolation in the film which impairs electric properties. The height of G-MP[⊕] has direct influence on the film thickness of the films. Taking the height of graphene and MP primary particles into account, a G-MP[⊕] monolayer already possesses a film thickness between 10 and 30 nm.

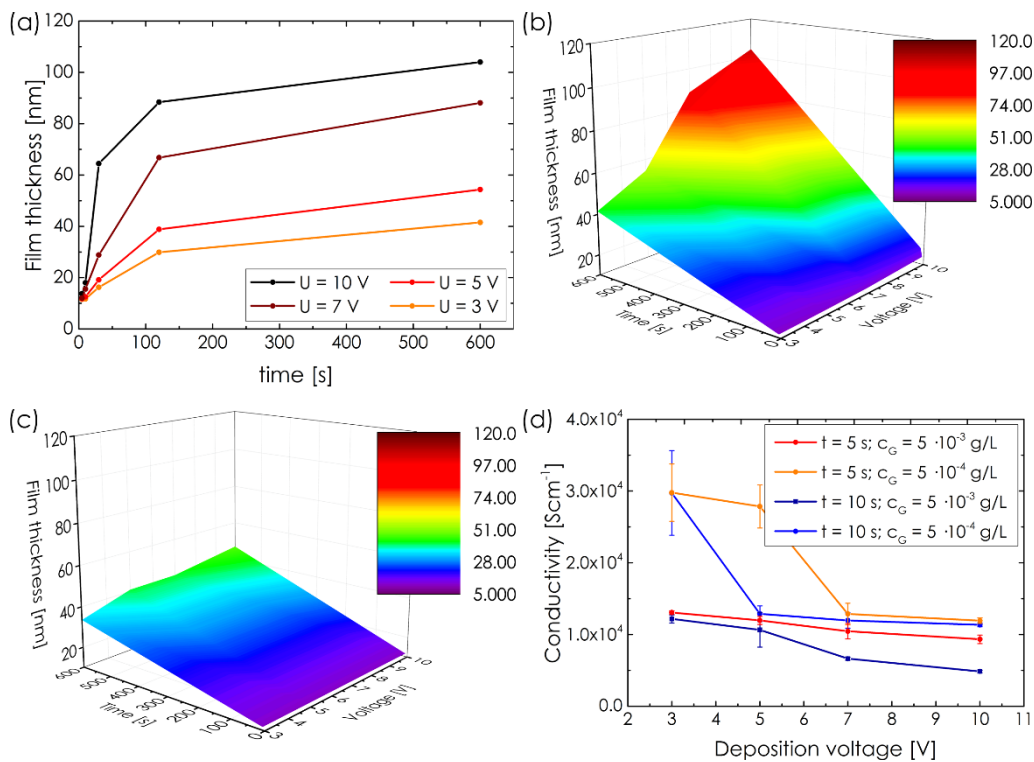


Figure 7.3: (a) Deposition kinetics of C-ED of G-MP[⊕] (C-ED_U-t-10⁻³); (b) Film thickness of C-ED_U-t-10⁻³ as function of time and voltage; (c) Film thickness of C-ED_U-t-10⁻⁴ as function of time and voltage; (d) Electrical conductivities of C-ED_U-5-c and C-ED_U-10-c films

The deposition time and voltage was varied between 5 s to 600 s and 3 V to 10 V, respectively. Lower voltages did not yield fully formed films whereas higher

voltages yielded highly corrupted films with visible ruptures. The influence of excessive deposition time was investigated as well. Preliminary tests were conducted over 1200 seconds, however the film thickness did not increase further.

The deposition kinetics were investigated as function of the three parameters deposition time, deposition voltage and graphene concentration (Figure 7.3a-c). Time-resolved measurements show that during the early stages of the process the film grows linearly. The linear growth stops after a short time and progresses asymptotically towards the maximum film thickness. The maximum film thickness and the initial deposition rate depend on the graphene concentration and the applied voltage. Both increase linearly with the potential. $C\text{-ED}_U\text{-t-}10^{-3}$ samples form a monolayer of $G\text{-MP}^\oplus$ during the first 5 to 10 seconds. Longer deposition time results in multilayer assembly. Monolayer assembly in $C\text{-ED}_U\text{-t-}10^{-4}$ samples progresses significantly more slowly. These samples further exhibit a lower maximum film thickness (50 nm compared to 105 nm of $C\text{-ED}_U\text{-t-}10^{-3}$ samples).

The deposition mechanism was visualized by means of AFM using samples $C\text{-ED}_7\text{-5-}10^{-3}$ to $C\text{-ED}_7\text{-600-}10^{-3}$ (figure 7.5). Up to $C\text{-ED}_7\text{-30-}10^{-3}$ the images show densely packed graphene sheets with more or less MP coverage. Coagulated MP forms small peaks between the graphene sheets. Compared to the rest of the film these peaks do not possess structural order. Nanomechanical analyses showed that, compared to the rest of the films, these peaks exhibit lesser modulus and dissipate more energy. There is only little difference in adhesive properties (figure 7.4). The films morphology changes after 30 seconds. Contrary to samples $C\text{-ED}_7\text{-5-}10^{-3}$ to $C\text{-ED}_7\text{-30-}10^{-3}$ the surface is now covered with patches of varying diameter.

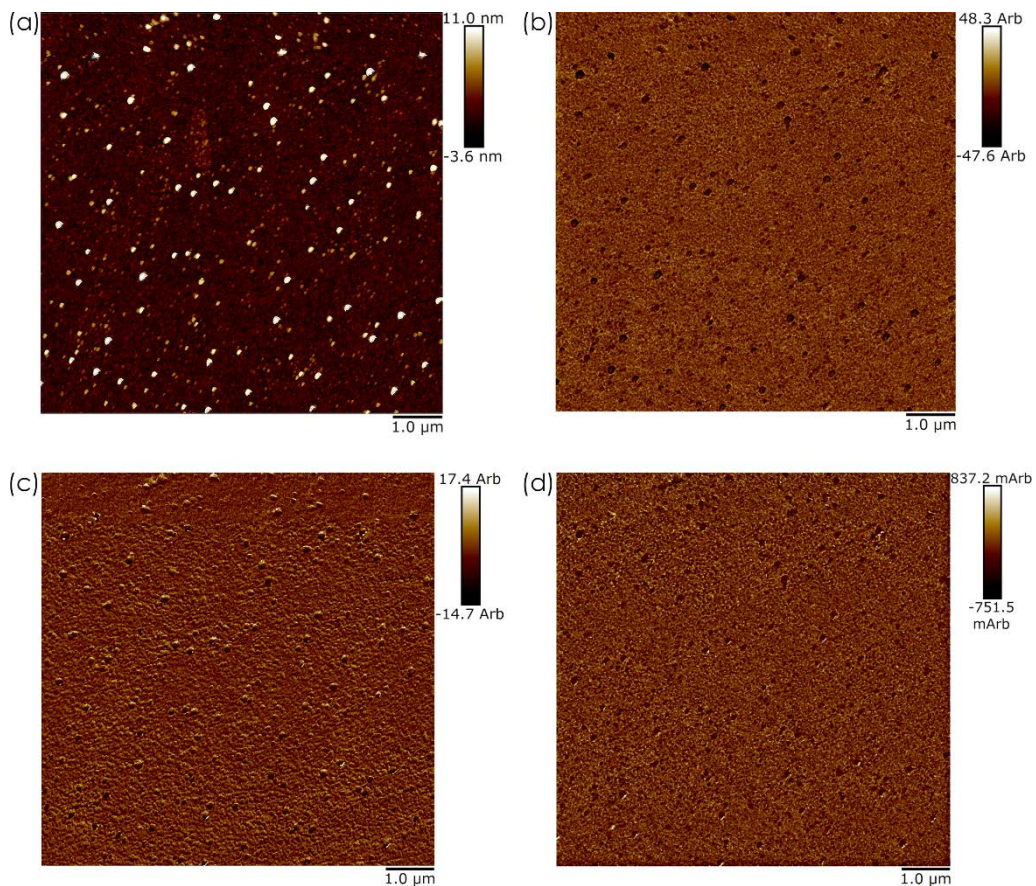


Figure 7.4: Nanomechanical analysis of C-ED_10-10-10⁻³; (a) height profile; (b) DMT modulus map; (c) Dissipation map; (d) Adhesion map

These patches are no longer connected and form separate islands. These islands consist of graphene at the bottom and coagulated MP the surface. The coagulated MP forms a continuous, smooth surface. The structural model is confirmed by the SEM images (figure 7.7). Removal of the upper layer shows that there are several stacked G-MP[⊕] sheets below the surface layer. The underlying graphene sheets are still ordered. The following mechanism is proposed. Due to electroosmotic effects MP constantly migrates to the film surface. The lack of electrostatic repulsion of the now uncharged particles causes MP to coalesce. Due to increasing film tension the surface smoothes and ruptures. The process is amplified by electroosmotic flow parallel to the substrate.

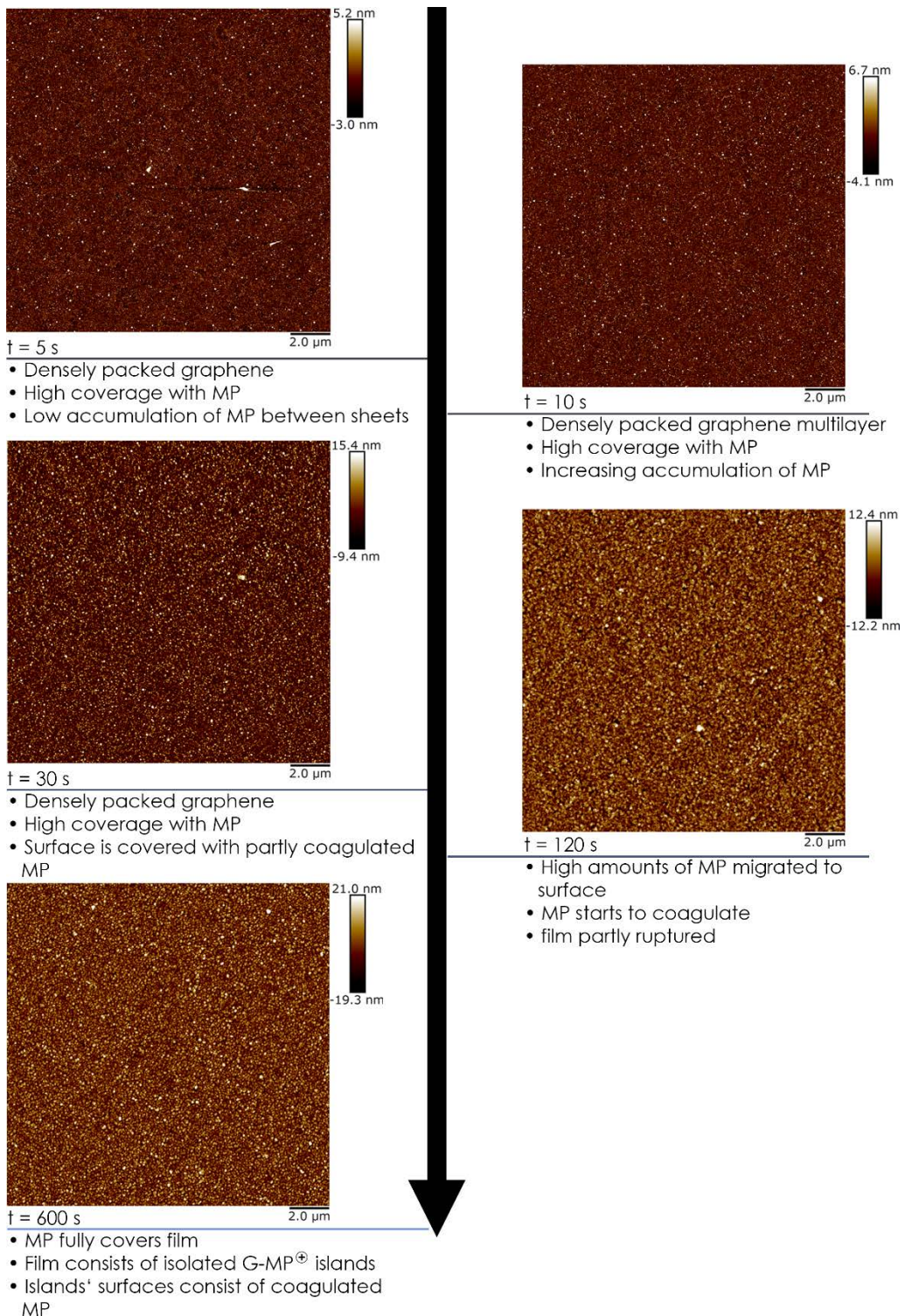


Figure 7.5: Development of film morphology during C-ED of G-MP[⊕] (C-ED_7-t-10⁻³)

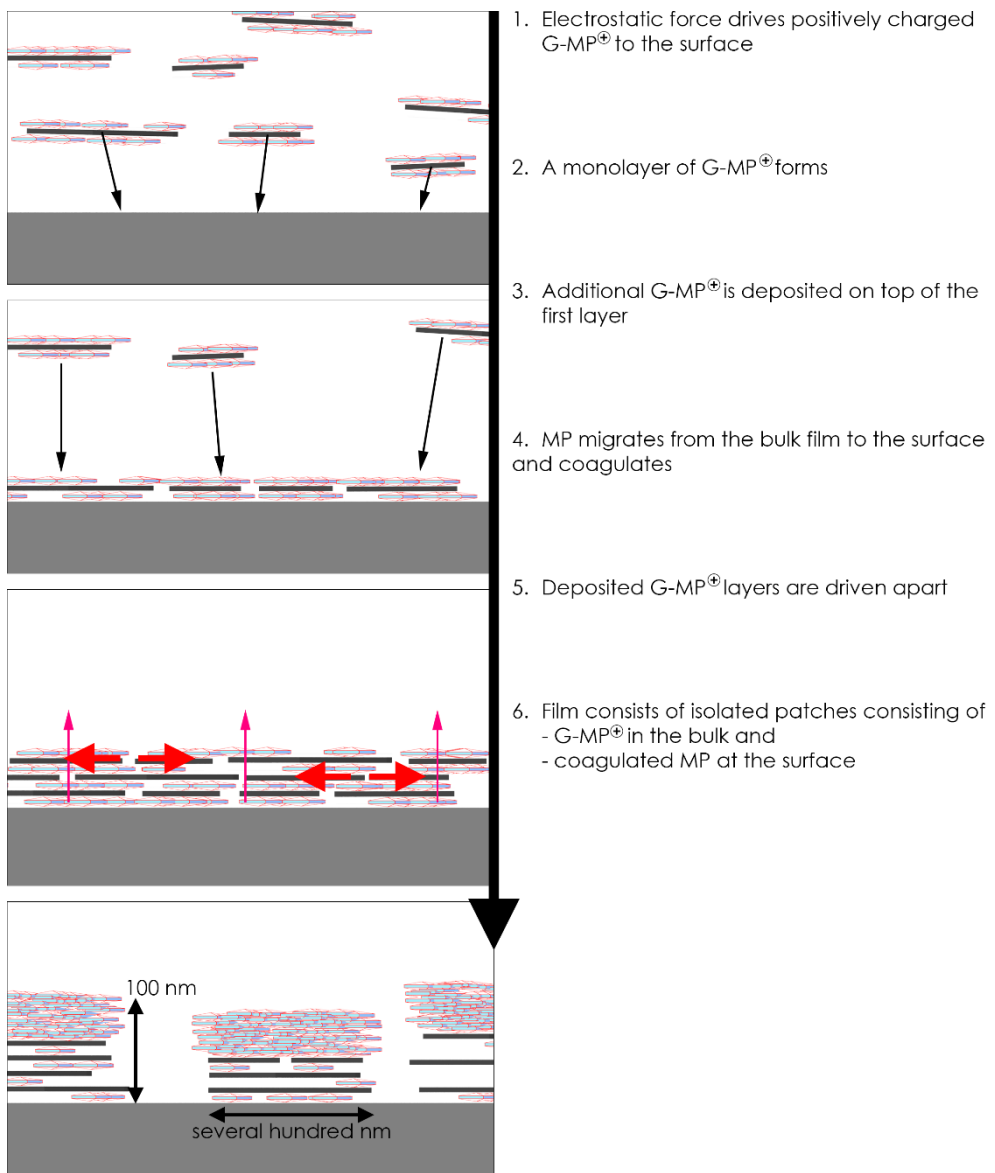


Figure 7.6: Mechanism of G-MP[⊕] deposition

The sheet resistances of *C-ED_U-5-c* and *C-ED_U-10-c* films were determined from four-point-probe measurements. *C-ED_U-120-c* and higher are electrical insulators. The insulating properties originate from the MP top layer and the missing contact between G-MP[⊕] islands (figure 7.6). From the measured voltages, the sheet resistances were calculated via

$$R_s = \frac{\pi}{\ln 2} \left(\frac{U}{I} \right) \quad (7.1)$$

Sheet resistance, film resistivity and conductivity are related via

$$\rho = d \cdot R_s = \frac{1}{\sigma} \quad (7.2)$$

where d is the film thickness. The electrical conductivity of the films decreases with increasing film thickness. $C\text{-}ED\text{-}U\text{-}5\text{-}10^4$ samples possess the highest conductivities ($3 \cdot 10^4 \text{ Scm}^{-1}$). The calculated values are not without error since the G-MP^\oplus layer is treated without considering the internal structure and the ITO sub-layer. A precise treatment would have to include the ITO layer as parallel circuit [205] and the internal structure of G-MP^\oplus as capacitive resistor and a series of parallel circuits. The simplification is justified by the fact that the sheet resistances of $C\text{-}ED\text{-}3\text{-}5\text{-}10^4$ and $C\text{-}ED\text{-}5\text{-}5\text{-}10^4$ are lower than the sheet resistance of the ITO sub-layer.

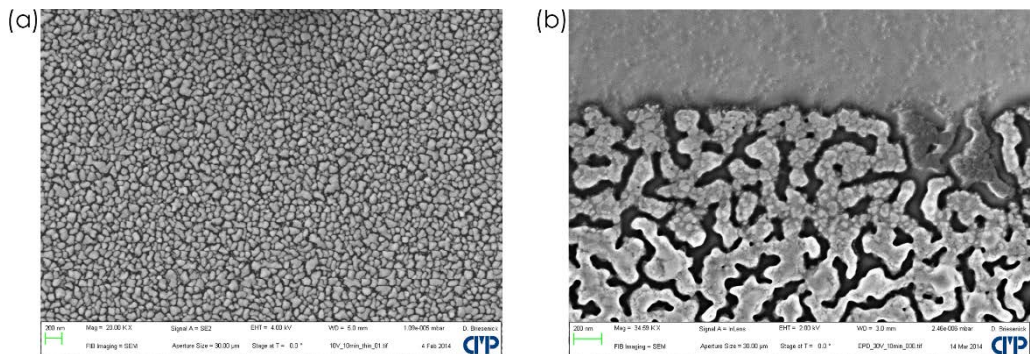


Figure 7.7: SEM images of $C\text{-}ED\text{-}10\text{-}600\text{-}10^3$ films; (a) top view and (b) top view after partial ablation of coagulated MP top layer

7.4 SUMMARY AND CONCLUSION

Aqueous G-MP[⊕] dispersions were successfully electrodeposited on ITO glass substrates.

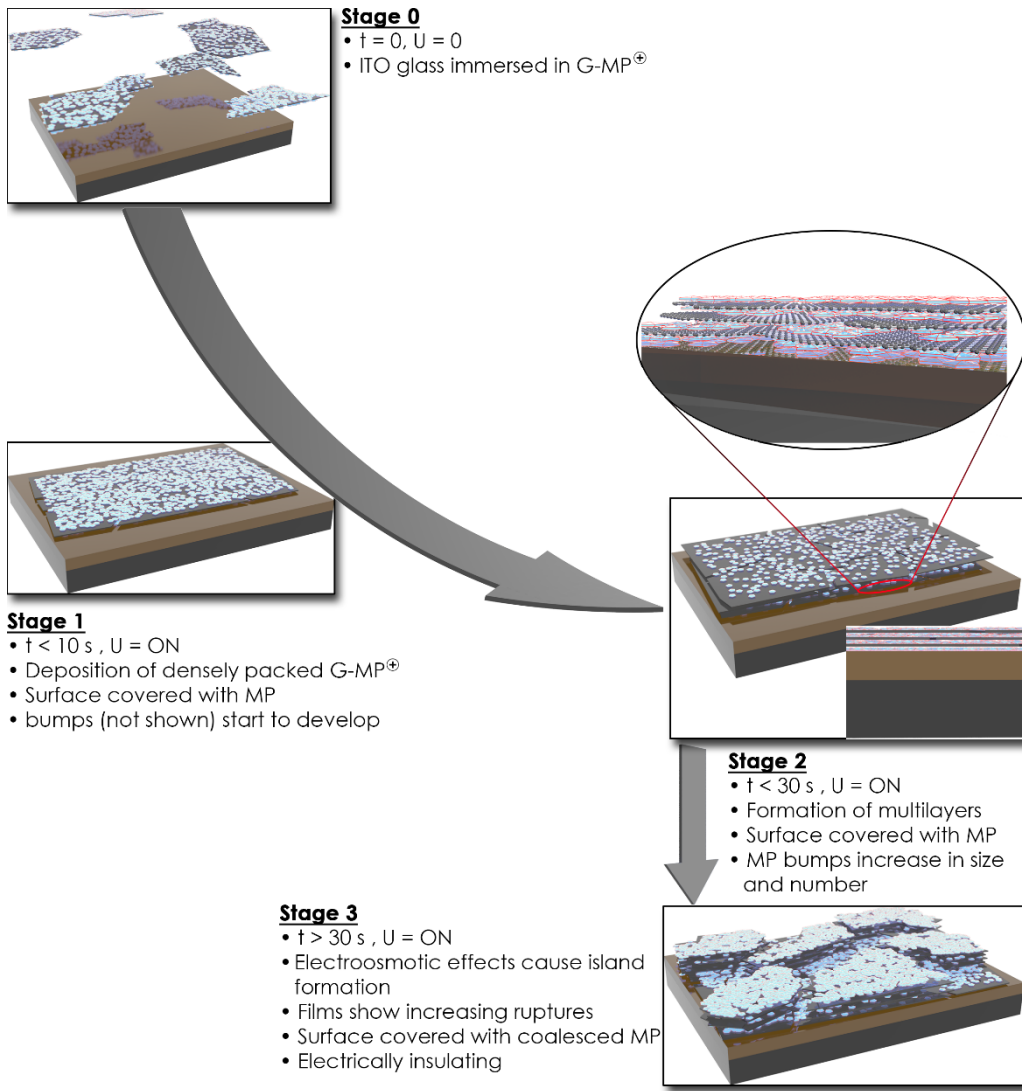


Figure 7.8: Illustration of C-ED of G-MP[⊕]

The deposition kinetics were evaluated by means of time-resolved UV-VIS and AFM measurements. The film thickness can be controlled between 10 and 110 nm. The process depends on deposition voltage, time and concentration of

G-MP[⊕]. C-ED of G-MP[⊕] follows a complex mechanism. During the first 5 to 10 seconds, a densely packed G-MP[⊕] monolayer forms. The average film thickness is 10 to 15 nm. These films are highly conductive. C-ED-3-5-10⁻⁴ films exhibited the highest conductivities ($3 \cdot 10^4$ Scm⁻¹). Subsequent deposition of G-MP[⊕] results in multilayer formation which is accompanied by MP migration to the surface. The electrical conductivity decreases due to the formation of an insulating MP surface layer. The high film tension of the MP layer and electroosmotic effects in electrode vicinity cause the films to rupture after about 120 s. Instead of a continuous G-MP[⊕] layer the film consists of isolated islands. The films are completely insulating.

The high conductivity and the optical transparency of the monolayer films provide the basis for several applications, including electronic devices and conductive polymer sandwich structures.

Chapter VIII

LAYER-BY-LAYER ASSEMBLY OF FUNCTIONALIZED GRAPHENE DISPERSIONS

8.1 INTRODUCTION

Layer-by-layer assembly (LBL) is a versatile method for processing charged graphene dispersions into conductive films. The general LBL process consists of alternately coating the substrate with oppositely charged particle dispersions and thorough rinsing between the deposition steps. The dip process (D-LBL) is highly time-consuming since in close proximity to the substrate the driving force is diffusion of uncharged particles. Spray-application (S-LBL) presents a less time-consuming alternative as the diffusive transport is complemented by convective forces. Regardless of the type of application LBL provides two important advantages over other methods for graphene thin film production. On the one hand, the film thickness can be closely controlled by varying the number of deposition cycles. On the other hand, LBL requires two types of particles which allows a high diversity of the deposited materials.

In this study LBL of the oppositely charged dispersions $G-M^{\ominus}$ and $G-MP^{\oplus}$ was conducted. Negatively charged graphene-HMMM dispersions ($G-M^{\ominus}$) are stable over a wider range of pH values and retain the negative charge at pH values above 6. Graphene-HMMM nano particle composite dispersions ($G-MP^{\oplus}$) are positively charged between pH 2.5 and 11. Both the underlying substrate consisting of previously deposited particles and the dispersed particles have to maintain their initial charge during every deposition step. In proximity to the substrates the occurring pH gradients alter the substrate charge. To prevent charge inversion and the resulting repulsive forces, the actual deposition pH values have to be determined for a given set of particles.

8.2 EXPERIMENTAL

8.2.1 LAYER-BY-LAYER ASSEMBLY EXPERIMENTS

Layer-by-layer assembly of G-M^\ominus and G-MP^\oplus was conducted on pre-treated glass substrates. Before immersion into a mixture of sulfuric acid and nitric acid (V/V 3:1) the glass slides were ultrasonically cleaned in a sequence of 2-propanol, ethanol and water. Preliminary experiments on positively charged, polyethylene imine modified glass substrates were conducted as well but are not laid further emphasis on. In a typical dipping process the substrate is alternately immersed in G-MP^\oplus and G-M^\ominus (D-LBL). The deposition time was 20 minutes for each deposition step. In order to remove non-adherent particles the samples were cleaned by double immersion in water for one minute and dried in a nitrogen flow.

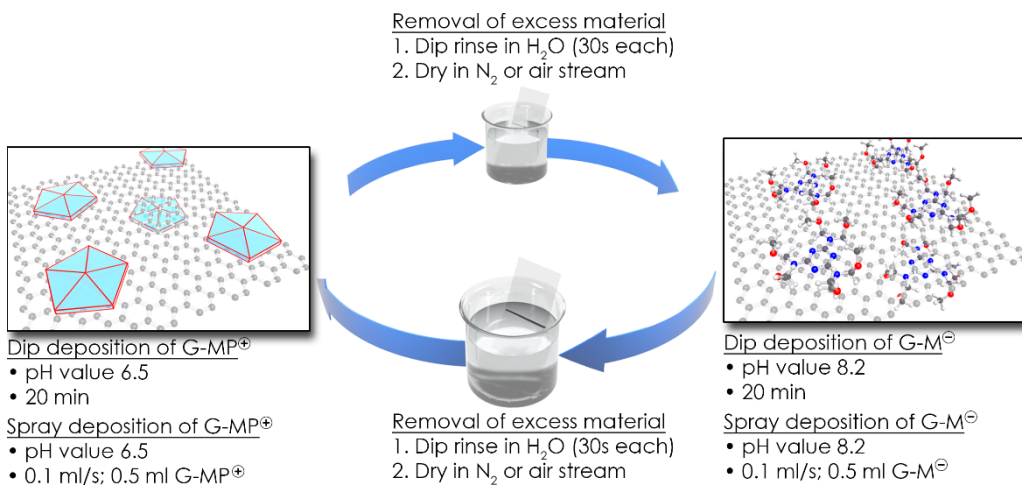


Figure 8.1: Layer-by-layer assembly process scheme (one cycle) for both dip- and spray deposition

Spray coating (S-LBL) of G-MP^\oplus and G-M^\ominus is similar to D-LBL. Each deposition step consists of application of 0.3 ml dispersion for 5 seconds. Sample rinsing and drying was performed in accordance to D-LBL. D-LBL and S-LBL films consisting of two to 15 double layers (N_{DL}) were prepared and accordingly

characterized with respect to film thickness and morphology. Dip-coated samples will be denoted as D-LBL_n with n being the number of double layers. Double layer in this context means one layer of G-MP[⊕] followed by one layer of G-M[⊖]. In accordance with figure 8.1 this corresponds to one deposition cycle. Accordingly spray-coated samples will be denoted as S-LBL_n.

8.2.2 ANALYTICAL STUDIES

G-M[⊖] and G-MP[⊕] dispersions were characterized with respect to zeta potential and particle dimensions. UV-VIS spectroscopy (Evolution 600, Thermo Scientific, Wolfram and Deuterium lamp, 450 nm) was employed to track the amount of deposited graphene. The measured transmission values were correlated to actual film thickness via AFM (Bruker Dimension Icon, Nanoscope V Controller, Peak Force Tapping mode) and SEM (Zeiss Neon 40, U = 3kV, d = 5 mm). Characterization of surface morphology was performed via AFM and SEM.

8.3 RESULTS

Layer-by-layer films consisting of G-M^\ominus and G-MP^\oplus were produced by dip- and spray coating. Spray application speeds up the process as convective flow overcomes the limitation of diffusion processes in the substrates' depletion layer. On the other hand, dip rinsing in contrast to spray rinsing allows the particles to settle and closely adhere to the substrate.

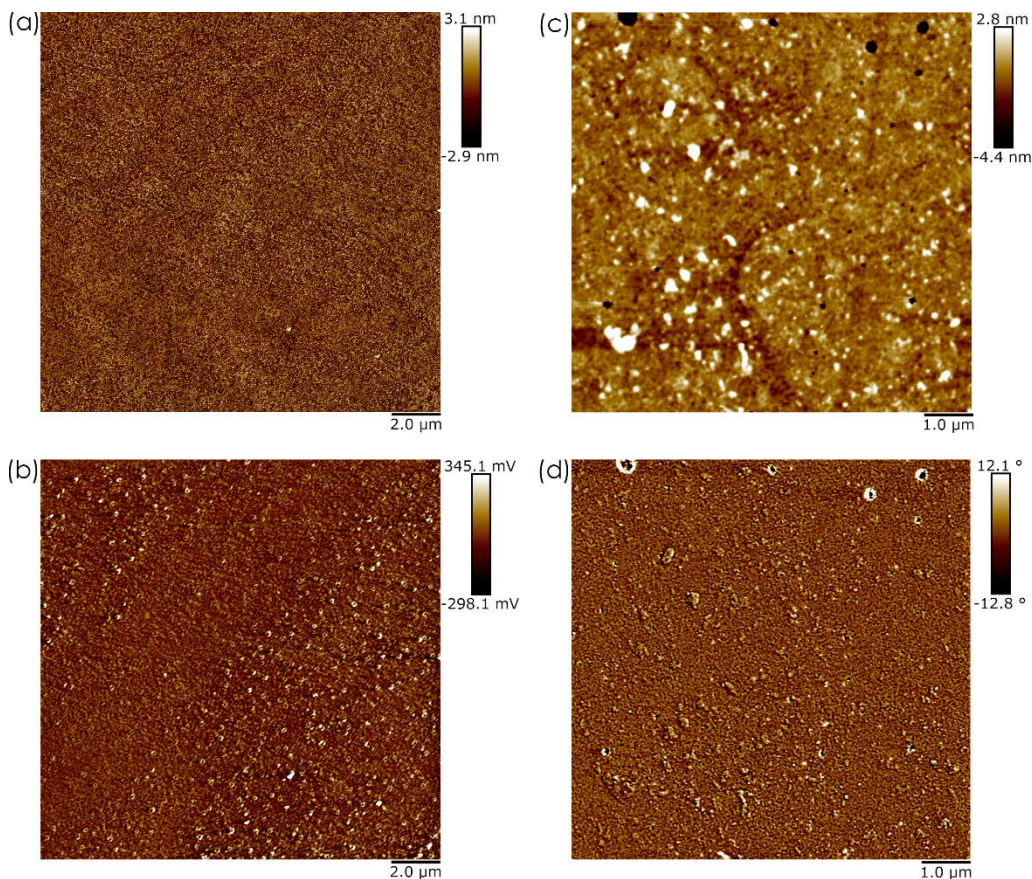


Figure 8.2: AFM (a) height profile and (b) Inphase image of negatively charged glass substrates; AFM (c) height profile and (d) phase image of PEI modified positively charged glass substrates

LBL assembly depends on the parameters substrate surface and charge, deposition time and dispersion pH value. In order to yield closely adherent, densely packed layers, the glass substrates were pre-treated with strong inorganic

acids (3 H₂SO₄ : 1 HNO₃). Negative surface charge is introduced either by chemical or by plasma treatment. Both processes increase the surface charge density without altering the morphology. The pre-treatment has several effects on the assembly. The nitrosyl cation formed during the reaction between reacts with Si-OH groups of the glass surface which yields NO₂ surface groups. The highly negative charge enables dense assembly of the first layer of positively charged particles. Further, the acids decompose organic residues which were not removed in the cleaning procedure. AFM images reveal nano-sized inhomogeneities ($R_q = 1.06$ nm) with slight differences in the material's properties (Figure 8.2).

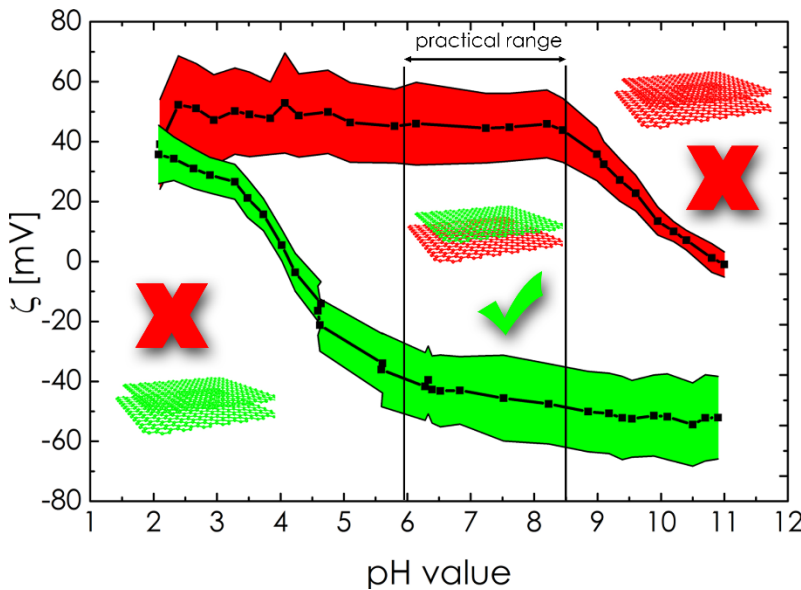


Figure 8.3: pH range for successful LBL assembly of G-M[⊖] and G-MP[⊕]

These local elements may enhance the adsorption of the first layer to the substrate. Positive surface charge can be established by adsorption of low molecular weight polyethylene imine (PEI). In contrast to the acid treatment PEI alters the surface structure of the substrate. The adsorbed polymers crumple and form large domains. These inhomogeneities may influence the particle adsorption as well. The dispersions' pH value and thus the surface charge of the

particles is important for the deposition process. The attractive force which is caused by the opposite charge of particle dispersion and substrate has to persist until the deposition of a layer is complete. Changes in the pH values of the dispersions influence the charge of the particles and of the surface. Extreme pH changes can invert the charge of the surface which causes the deposition to stop. To prevent this, the pH values of the dispersions have to be chosen carefully. Effects like pH gradients close to the surface have to be considered as well. LBL assembly was performed in pH ranges where both species exhibit constant zeta potential.

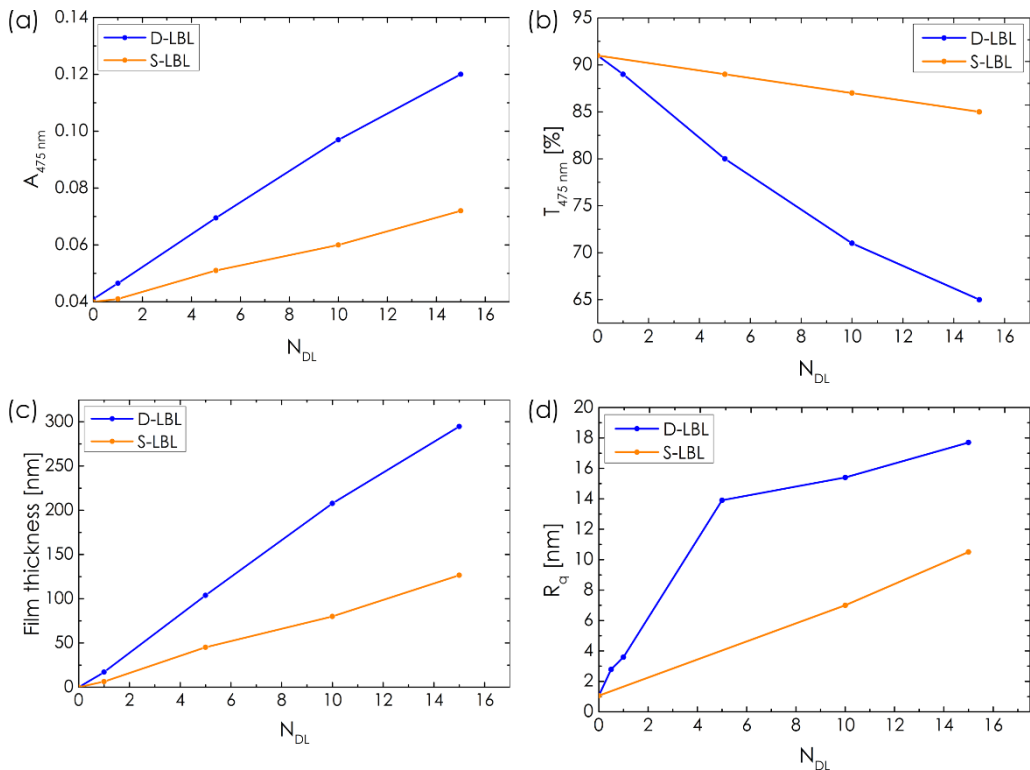


Figure 8.4: Optical and surface properties of dip- and spray assemblies; (a) Absorption as function of double layer count; (b) Transmission as function of double layer count; (c) calculated film thickness as function of double layer count; (d) Mean roughness as function of double layer count

Isoelectric titrations of G-MP $^{\oplus}$ and G-M $^{\ominus}$ were conducted to determine the optimal pH range. Freshly prepared G-MP $^{\oplus}$ dispersions exhibit zeta potentials

around +35 mV at pH 7. G-MP[⊕] is constantly positively charged between pH 2.5 and 10. The wide range of constant positive charge emphasizes the versatility of the composite particles. Charge inversion of a previously deposited G-MP[⊕] layer is only possible if the other material is highly basic. G-M[⊖] possesses almost constant negative potential between pH 6.2 and 11. In contrast to G-MP[⊕] the dispersions are sensitive to changes in the aqueous environment. On account of local pH gradients the practical pH range for LBL of G-MP[⊕] and G-M[⊖] reduces to an effective range between pH 6 and 8.5. G-MP[⊕] could be deposited over the whole range. For the deposition the dispersions' native pH value of 7 was kept. AFM measurements showed that successful G-M[⊖] assembly requires pH values around 8.2 which is close to the upper threshold.

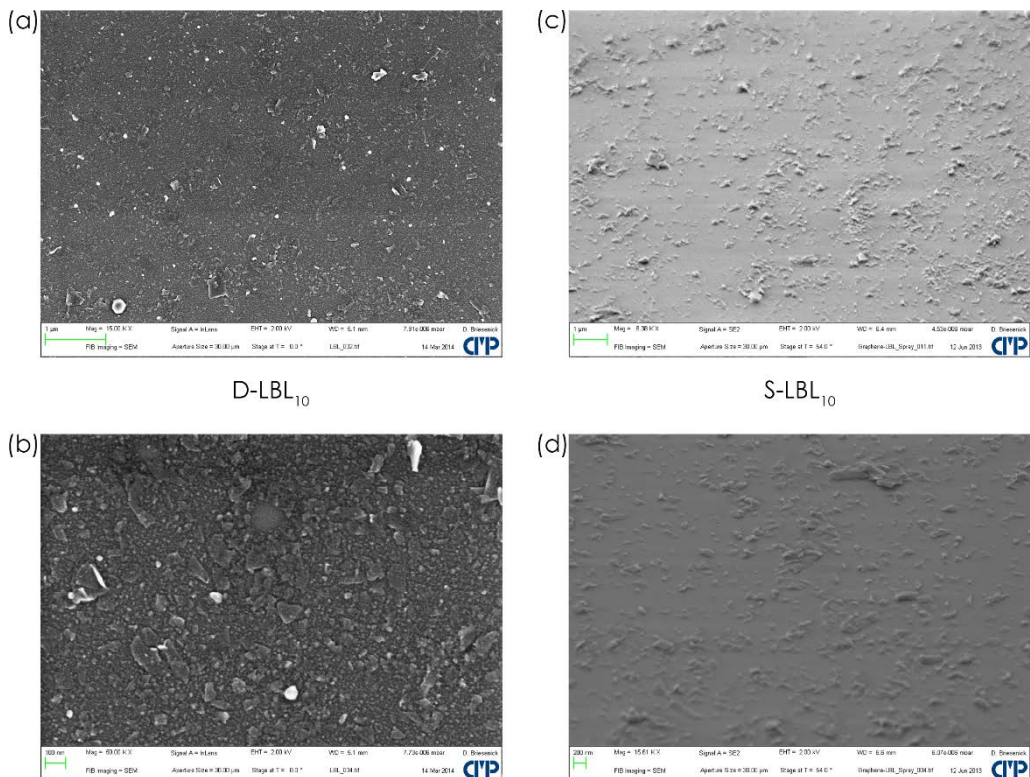


Figure 8.5: SEM images of D-LBL₁₀ and S-LBL₁₀ with different magnifications

LBL assembly of G-MP[⊕] and G-M[⊖] was monitored by means of UV-VIS spectroscopy (475 nm). Due to the dispersed graphene both particle species show

moderate adsorption in the visible range. The transmission of D-LBL and S-LBL films decreases linearly with increasing number of layers. The values were correlated with AFM measurements to calculate the film thickness. Due to the constant removal of weakly adherent particles and agglomerates S-LBL films are generally thinner and smoother than D-LBL films. The calculated thickness of one S-LBL double layer amounts to 10 nm. This value correlates roughly to the height of $\text{G-}\text{MP}^{\oplus}$ (8-10 nm) and $\text{G-}\text{M}^{\ominus}$ (1-2 nm). Dynamic effects leading to reordering in the films are not accounted for. D-LBL double layer can be significantly thicker. Removal of deposited agglomerates is not as effective as it is in S-LBL. The prepared D-LBL films showed thicknesses between 10 and 300 nm. S-LBL film thickness was controlled between 10 and 100 nm (same number of layers). The lower thickness highlights the differences in the deposition processes.

The morphologies of the films were visualized via AFM and SEM. D-LBL₁ and S-LBL₁ films show almost identical morphologies. Higher numbers of D-LBL layers cause increasing deposition of agglomerates. The effect is observed in S-LBL as well, the magnitude however is considerably lower.

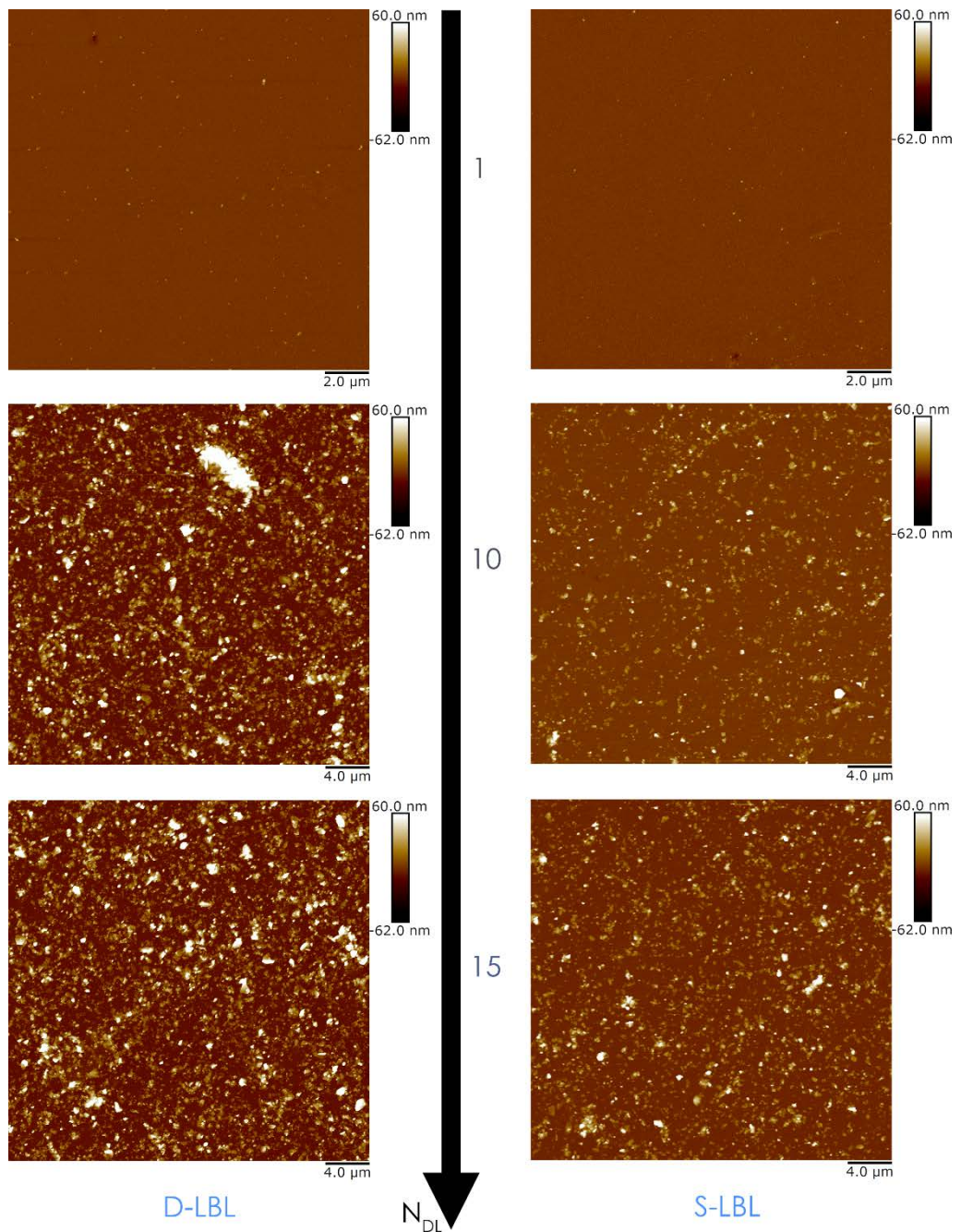


Figure 8.6: Evolution of film morphology for D-LBL and S-LBL with increasing number of double layers

8.4 SUMMARY AND CONCLUSION

G-MP^{\oplus} and G-M^{\ominus} dispersions were successfully deposited in a layer-by-layer fashion.

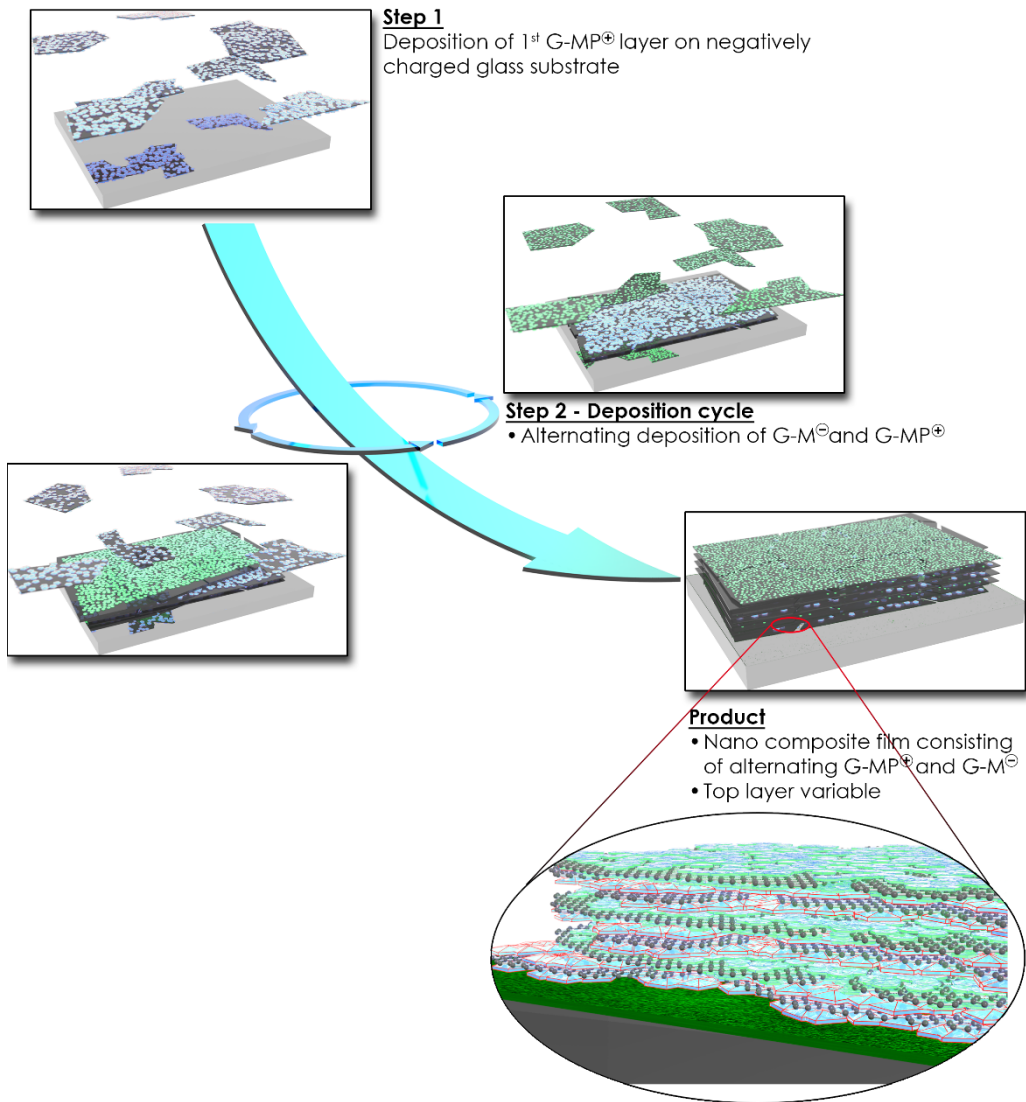


Figure 8.7: Layer-by-layer assembly of G-M^{\ominus} and G-MP^{\oplus} resulting in nano composite films

Both dip-coating (D-LBL) and spray coating (S-LBL) techniques were evaluated. To avoid charge inversion of the underlying substrate layer the pH

values of G-MP^{\oplus} and G-M^{\ominus} were set to 7 and 8.2 respectively. By means of UV-VIS spectroscopy it was shown that the resulting film thickness increases linearly with the amount of deposited double layers. Both D-LBL and S-LBL result in highly transparent, smooth films. S-LBL film quality is slightly superior to D-LBL film quality. The films show less aggregated particles and thus an extremely smooth surface. The convective flow of the particles towards and away from the surface causes removal of adherent agglomerates. S-LBL offers two additional advantages over D-LBL. Cross-contamination does not occur and the deposition process is sped up by a factor of about 240.

Although the deposited films were not yet tested for specific properties like conductivity or mechanical properties, the results emphasize that LBL assembly is a versatile method for manufacture of graphene thin films. The films show high optical transmittance and low surface roughness which is a primary requirement for manufacture of transparent conductive graphene films. Due to the intercalation of MP in the film, capacitive properties should be investigated. Further research should include polymeric substrates and investigation of respective film properties. In addition, both G-M^{\ominus} and G-MP^{\oplus} should be investigated with respect to LBL films using other materials which could greatly increase the range of applications.

Chapter IX

SUMMARY, CONCLUSIONS AND
OUTLOOK

This study consisted of six research project on hexamethoxymethyl melamine (HMMM) and graphene. The individual sections of the study are built each upon the other but also present separate studies with unique results. The topics were:

- HMMM phase behavior (Chapter III)
- HMMM nano particle dispersions (MP) (Chapter IV)
- Graphene-HMMM nano composite dispersions ($G\text{-}M}^{\ominus}$) (Chapter V)
- Graphene-MP nano composite dispersions ($G\text{-}MP}^{\oplus}$) (Chapter VI)
- Electrodeposition of $G\text{-}MP}^{\oplus}$ and $G\text{-}M}^{\ominus}$ (Chapter VII)
- Layer-by-layer assembly of $G\text{-}MP}^{\oplus}$ and $G\text{-}M}^{\ominus}$ (Chapter VIII)

This summary presents the key findings of the different sections.

Aqueous HMMM systems show a complex phase behavior which depends on HMMM concentration, ageing and temperature. Below 30 g/L HMMM forms emulsion droplets (E). Between 30 and 100 g/L the systems consist of emulsion and microemulsion droplets (EME). Concentrations above 100 g/L result in HMMM microemulsions (ME). Depending on the concentration range, two ageing processes were found. HMMM emulsions underlie Ostwald ripening which over time results in phase separation. EME and ME are self-stabilizing systems. By including residual methanol and formaldehyde the amount of thermodynamically stable ME droplets increases while the emulsion droplets decrease in number and diameter. As a result, the EME concentration range shifts to 10 to 60 g/L. The microemulsion threshold drops down to 60 g/L. EME and ME systems exhibit a phase inversion to water in HMMM emulsions. The phase inversion temperature depends on HMMM concentration and ageing. The self-stabilizing effect raises the inversion temperature.

Aqueous HMMM nano particle dispersions (MP) were synthesized by acid-catalyzed self-condensation. Mechanistic and kinetic modeling of the reaction yielded a refined model for the underlying HMMM self-condensation and a full description of the nano particle synthesis. The reaction is sub-divided into two

phases – HMMM phase inversion and particle growth. MP synthesis requires EME systems and the phase inversion leading to W/H emulsions. Hence the possible educt range extends from 30 to 100 g/L. However, concentrations above 55 g/L yield increasing amounts of aggregates. HMMM concentration further influences the rate of the reaction. Due to the complexity of the mechanism a functional interrelation could not be established. The reaction is highly pH sensitive. The amount of catalyst directly controls reaction rate (reaction is 1st order in H⁺) and product properties. Too low concentration yield unstable dispersions. On the other hand, excessive concentrations cause formation of non-reactive intermediates. The reaction possesses an activation energy of 136 ± 35 kJ/mol. By choosing specific catalyst amounts the MP particle size can be controlled between 5 (primary particles) and 250 nm. With increasing diameter, the particles' shapes become more and more anisotropic. Large particles show disc-like structures. This superstructure originates from stacking of HMMM triazine rings and lateral particle growth. The positive surface charge of MP dispersions originates from protons bound by adjacent dimethylene ether bridges. A functional relation between the process parameters and the resulting zeta potential was not found.

Two-dimensional graphene-HMMM composite dispersions (G-M[⊖]) were synthesized from graphite and HMMM emulsions. The maximum concentration of single-layer G-M[⊖] was 43 µg/ml. The dispersions contained hybrid particles with diameters between 50 and 900 nm and heights around 1.7 nm. The negative surface charge (zeta potential around -40 mV at pH 7) originates from a charge transfer complex between graphene and the triazine derivative. Charge inversion to positive surface charge is possible around pH 3.5. Native and charge-inverted dispersions are long-term stable. Due to cancellation of the charge-transfer lower pH values result in rapid precipitation. The stability of the particles is enhanced by aromatic π-stacking interactions.

Nano composite dispersions based on graphene and HMMM nano particle dispersions (G-MP^\oplus) were successfully synthesized and characterized. The highest determined graphene concentration was 0.8 mg/ml. The particles exhibit anisotropic character (height 10 nm and diameter between 50 and 1000 nm). The height accounts for MP adsorbed to both sides of a single graphene sheet. Adsorbed MP introduces positive charge between pH 2 and 10 (zeta potential around 50 mV). Charge inversion is not possible. On a molecular scale MP and graphene interact via ternary hydrogen bridges in combination with cation- π and π -stacking interactions. The multifaceted interactions result in long-term stability of the composite dispersions (several months).

The positively charged G-MP^\oplus dispersions were electrodeposited in form transparent conductive graphene films. The kinetics of the process and the resulting structures were investigated. Film thickness can be controlled between 10 and 110 nm. The deposition mechanism is complex and consists of two stages. During stage one, a dense monolayer of G-MP^\oplus forms. This monolayer is about 10 to 15 nm thick. Excess MP accumulates in form of peak-like structures. The films are highly transparent and possess high electrical conductivity. Further deposition results in multilayer assembly. During this stage, excess MP constantly migrates to the surface. High film tension and electroosmotic effects parallel to the substrate cause the surface structure to change. Instead of a dense film, separate islands form which consist of G-MP^\oplus at the bottom and coagulated MP at the top. Due to the lack of graphene percolation and the insulating MP layer, increasing film thickness is accompanied by decreasing conductivity. The films exhibit an increasing metallic luster.

Layer-by-layer assembly of G-M^\ominus and G-MP^\oplus resulted in transparent graphene films. Experiments regarding electrical properties were not conducted. Based on the intrinsic properties of the dispersions suitable deposition parameters were

developed. Deposition was conducted via spray coating (S-LBL) and dip coating (D-LBL). Both methods provide a high degree of film thickness control and result in highly transparent films. However, S-LBL has two decisive advantages. On the one hand, the deposition process is much faster than D-LBL (factor 200). On the other hand, S-LBL results in monolayer assembly. In addition to diffusive transport which predominates D-LBL assembly, transport processes in S-LBL include convection as well. The resulting forces remove loosely adherent agglomerates from the surface. In comparison to D-LBL films, S-LBL films exhibit lower thickness and lower roughness values.

To conclude, transparent conductive graphene films were successfully prepared via electrodeposition and layer-by-layer assembly. The chemical and physical background to develop and understand the processes was established by investigating HMMM in water, HMMM nano particle dispersions and the respective graphene composite dispersions. In addition to TCFs the developed concepts are valuable for various other applications.

REFERENCES

- [1] Novoselov, K.S.; Geim, A.K.; et al., *Science*, **2004**, 306, 666
- [2] Wainwright, A., “*The Western Fells*”, London, **2003**
- [3] Woodfall, H.; Strahan, W., “*The Statutes at Large: From the Twentieth Year of the Reign of KING GEORGE the SECOND To the Thirtieth Year of the Reign of KING GEORGE the SECOND*”, London, 1764
- [4] Scheele, C.W.K., *Svenska vetensk. Acedem. Handlingar*, **1779**, 40, 238
- [5] Werner, A.G., „*Versuch einer Erklärung der Entstehung der Vulkane durch die Entzündung mächtiger Steinkohleschichten*“, Zürich, **1789**
- [6] Acheson, E.G., US 568323 A, **1896**
- [7] Hull, A.W., *Phys Rev.*, **1917**, 10, 661
- [8] Bernal, J.D., *Proc. R. Soc. A*, **1924**, 106, 749
- [9] Wallace, P.R., *Phys. Rev.*, **1947**, 71(9), 622
- [10] McClure, J.W., *Phys. Rev.*, **1957**, 108, 612
- [11] Slonczewski, J.C.; Weiss, P.R., *Phys. Rev.*, **1958**, 109, 272
- [12] Schroeder, P.R.; Dresselhaus, A., *Phys. Rev. Lett.*, **1968**, 20, 1292
- [13] Rydberg, H.; Dion, M.; et al., *Phys. Rev. Lett.*, **2003**, 91, 126402
- [14] Stankovich, S.; et al., *J. Mater. Chem.*, **2006**, 16, 155
- [15] Brodie, B.C., *Phil. Trans. Roy. Soc. London*, **1859**, 149, 249
- [16] Staudenmaier, *Ber. d. Deutsch. Chem. Ges.*, **1898**, 31(2), 1481
- [17] Hummers, W.S.; Offeman, R.E., *J. Am. Chem. Soc.*, **1958**, 80(6), 1339
- [18] Flowers, L.C., US 3457171, **1969**
- [19] Nakajima, T.; Hagiwara, R.; et al., *J. Electrochem. Soc.*, **1986**, 133(9), 1761
- [20] Ebert, L.B., *Annu. Rev. Mat. Sci.*, **1976**, 6, 181
- [21] Lerf, A.; He, H.; Forster, M.; Klinowski, J., *J. Phys. Chem. B*, **1998**, 102, 4477
- [22] Badami, D.V., *Nature*, **1962**, 193, 570
- [23] Morgan, A.E.; Somorjai, G.A., *Surf. Sci.*, **1968**, 12, 405
- [24] Blakely, J.M.; Kim, J.S.; Potter, H.C., *J. Appl. Phys.*, **1970**, 41, 2693
- [25] Boehm, H.P.; Clauss, A.; et al., *Z. Anorg. Allg. Chem.*, **1962**, 316, 119
- [26] Boehm, H.P.; Setton, R.; Stumpp, E., *Carbon*, **1986**, 24, 241
- [27] Mermin, N.D.; Wagner, H., *Phys. Rev. Lett.*, **1966**, 17, 1133
- [28] Hohenberg, P.C., *Phys. Rev. Lett.*, **1967**, 158, 383
- [29] Lu, X.; Yu, M.; Ruoff, R.S., *Nanotechnology*, **1999**, 10, 269
- [30] Castro Neto, A.H.; Guinea, F.; et al., *Rev. Mod. Phys.*, **2009**, 81, 109
- [31] Raza, H., *Graphene Nanoelectronics, Nanoscience and Technology*, pp. 237 Berlin, **2012**
- [32] Wolff, M., *Exploring the Physics of the Unknown Universe*, Manhattan Beach, **1990**
- [33] Emtsev, K.V.; Bostwick, A.; et al., *Nat. Mater.*, **2009**, 8, 203
- [34] Li, X.; Cai, W.; et al., *Science*, **2009**, 324, 1312

- [35] Geim, A.K.; Novoselov, K.S., *Nat. Mater.*, **2007**, 6, 183
- [36] Morozov, S.V.; Novoselov, K.S.; et al., *Phys. Rev. Lett.*, **2008**, 100, 016602
- [37] Mayorov, A.S.; Gorbachev, R.V.; et al., *Nano Lett.*, **2011**, 11, 2396
- [38] Peres, N.M.R., *Rev. Mod. Phys.*, **2010**, 82, 2673
- [39] Das Sarma, S.; Adam, S.; et al., *Rev. Mod. Phys.*, **2011**, 83, 407
- [40] Peres, N.M.R.; Guinea, F.; et al., *Phys. Rev. B.*, **2006**, 73, 125411
- [41] Stauber, T.; Peres, N.M.R.; et al., *Phys. Rev. B.*, **2008**, 78, 085418
- [42] Ziegler, K., *Phys. Rev. B*, **2007**, 75, 233407
- [43] Dóra, B.; Ziegler, K.; Thalmeier, P., *Phys. Rev. B*, **2008**, 77, 115422
- [44] Martin, J.; Akerman, N.; et al., *Nat. Phys.*, **2008**, 4, 144
- [45] Zhang, Y.; Brar, V.W.; et al., *Nat. Phys.*, **2009**, 5, 722
- [46] Morozov, S.V.; Novoselov, K.S.; et al., *Phys. Rev. Lett.*, **2008**, 100, 016602
- [47] Fang, T.; Konar, A.; et al., *Appl. Phys. Lett.*, **2007**, 91, 092109
- [48] Fernandez-Rossier, J.; Palacios, J.J.; et al., *Phys. Rev. B*, **2007**, 75, 205441
- [49] Leenaerts, O.; Partoens, B.; et al., *Phys. Rev. B*, **2008**, 77, 125416
- [50] Zhang, Y.-H.; Zhou, K.-G.; et al., *Nanotechnology*, **2010**, 21, 065201
- [51] Chang, C.-H.; Fan, X.; et al., *J. Phys. Chem. C*, **2012**, 116, 13788
- [52] Shen, C.C.; Lin, C.T.; et al., *Appl. Phys. Lett.*, **2012**, 101, 111907
- [53] Medina, H.; Lin, Y.-C.; et al., *Adv. Funct. Mater.*, **2011**, 21, 2687
- [54] Lu, Y.H.; Chen, W.; et al., *J. Phys. Chem. B Lett.*, **2009**, 113, 2
- [55] Chen, L.; Wang, L.; et al., *J. Phys. Chem. Lett.*, **2013**, 4, 2158
- [56] Schedin, F.; Geim, A.K.; et al., *Nat. Mater.*, **2007**, 6, 652
- [57] Mak, K.F.; Sfeir, M.Y.; et al., *Phys. Rev. Lett.*, **2008**, 101, 196405
- [58] Nair, R.R.; Blake, P.; et al., *Science*, **2008**, 320, 1308
- [59] Miller, J.R.; Outlaw, R.A.; et al., *Electrochim. Acta*, **2011**, 56(28), 10443
- [60] Stoller, M.D.; Park, S.; et al., *Nano Lett.*, **2008**, 8, 3498
- [61] Chen, Y.; Zhang, X.; et al., *J. Power Sources*, **2010**, 195, 3031
- [62] Yin, S.Y.; Zhang, Y.Y.; et al., *ACS Nano*, **2011**, 5, 3831
- [63] Peigney, A.; Laurent, C.; et al., *Carbon*, **2001**, 39, 507
- [64] Yan, J.; Fan, Z.; et al., *Adv. Funct. Mater.*, **2012**, 22, 2632
- [65] Wang, H.; Liang, Y.; et al., *Nano Res.*, **2011**, 4, 729
- [66] Yan, J.; Fan, Z.; et al., *Carbon*, **2010**, 48(13), 3825
- [67] Wu, Q.; Xu, Y.; et al., *ACS Nano*, **2010**, 4(4) 1963
- [68] Lee, C.; Wie, X.; et al., *Science*, **2008**, 321, 385
- [69] Guo, Z.; Ran, S.; et al., *Comp. Sci. Tech.*, **2013**, 86, 157
- [70] Varhese, T.V.; Kumar, H.A.; et al., *Carbon*, **2013**, 61, 476
- [71] Li, X.; McKenna, G.B.; et al., *Polymer*, **2014**, 55, 248
- [72] Yang, X.; Xu, M.; et al., *Polym. Compos.*, **2014**, 35, 404
- [73] Wu, H.; Drzal, T., *J. Appl. Polym. Sci.*, **2013**, 130(6), 4081
- [74] Castelaín, M.; Martínez, G.; et al., *Macromolecules*, **2013**, 46, 8980
- [75] Balandin, A.A.; Ghosh, S.; et al., *Nano Lett.*, **2008**, 8(3), 902
- [76] Berger, S.; Kwon, Y.-K.; et al., *Phys. Rev. Lett.*, **2000**, 84, 4613
- [77] Czichos, H., *Die Grundlagen der Ingenieurwissenschaften*, Berlin, **2000**
- [78] Ferrari, A.C.; Basko, D.M., *Nat. Nanotechnol.*, **2013**, 8, 235
- [79] Yan, J.-A.; Ruan, Y.; et al., *Phys. Rev. B*, **2008**, 77, 125401
- [80] Malard, L.M.; Pimenta, M.A.; et al., *Phys. Rep.*, **2009**, 473, 51

[81] Sanders, G.D.; et al., *J. Phys.: Condens. Matter*, **2013**, 25, 144201

[82] Kohn, W., *Phys. Rev. Lett.*, **1959**, 2(9), 393

[83] Milošević, I.; Kepčija, N.; et al., *Mat. Sci. Engin. B*, **2011**, 176, 510

[84] Tang, B.; Guoxin, H.; et al., *Appl. Spectroscopy Rev.*, **2010**, 45, 369

[85] Saito, R.; Hofmann, M.; et al., *Adv. Phys.*, **2011**, 60(3), 413

[86] Ferrari, A.C.; Meyer, J.C.; et al., *Phys. Rev. Lett.*, **2006**, 97, 187401

[87] Tsukamoto, T.; Yamazaki, K.; et al., *J. Phys. Chem. C*, **2012**, 116, 4732

[88] Casiraghi, C.; Pisana, S.; et al., *Appl. Phys. Lett.*, **2007**, 91, 233108

[89] Balandin, A.A.; Ghosh, S.; et al., *Nano Lett.*, **2008**, 8(3), 902

[90] Subrahmanyam, K.S.; Voggu, R.; et al., *Chem. Phys. Lett.*, **2009**, 472, 96

[91] Das, B.; Voggu, R.; et al., *Chem. Commun.*, **2008**, 5155

[92] Blake, P.; Hill, E.W.; et al., *Appl. Phys. Lett.*, **2007**, 91, 063124

[93] Busch, G.A., *Silicon Carbide: A High temperature semiconductor: Proceedings of the conference on silicon carbide Boston, Mass.*, pp. 160, Oxford, **1960**

[94] Badami, D.V., *Nature*, **1962**, 193, 570

[95] Bauer, A.; Kräußlich, J.; et al., *Phys. Rev. B*, **1998**, 57(5), 2647

[96] Capitani, G.C.; Di Pierro, S.; et al., *Am. Mineralogist*, **2007**, 92, 403

[97] Hass, J; et al., *Appl. Phys. Lett.*, **2006**, 89, 143106

[98] Srivastava, N.; He, G.; et al., *Phys. Rev. B*, **2010**, 82, 235406

[99] van Bommel, A.J.; Crombeen, J.E.; et al., *Surf. Sci.*, **1975**, 48, 463

[100] Tedesco, J.L.; Jernigan, G.G.; et al., *Appl. Phys. Lett.*, **2010**, 96, 222103

[101] Virojanadara, C.; Syväjärvi, M.; et al., *Phys. Rev. B*, **2008**, 78, 245403

[102] Tromp, R.M.; Hannon, J.B., *Phys. Rev. Lett.*, **2009**, 102, 106104

[103] Emtsev, K.V.; Bostwick, A.; et al., *Nat. Mater.*, **2009**, 8, 203

[104] Berger, C.; Song, Z.; et al., *J. Phys. Chem. B*, **2004**, 108, 19912

[105] Morgan, A.E.; Somorjai, G.A., *Surf. Sci.*, **1968**, 12, 405

[106] Blakely, J.M.; Kim, J.S.; et al., *J. Appl. Phys.*, **1970**, 41, 2693

[107] Zhang, Y.; Zhang, L.; et al., *Acc. Chem. Res.*, **2013**, 46(10), 2329

[108] Yu, Q. K.; Lian, J.; et al., *Appl. Phys. Lett.*, **2008**, 93, 113103

[109] De Arco, L. G.; Zhang, Y.; et al., *IEEE Trans. Nanotechnol.*, **2009**, 8, 135

[110] Reina, A.; Jia, X.; et al., *Nano Lett.*, **2009**, 9, 30

[111] Liu, N.; Fu, L.; et al., *Nano Lett.*, **2011**, 11, 297

[112] Li, X.; Cai, W.; et al., *Science*, **2009**, 324, 1312

[113] Wu, W.; Jauregui, L. A.; et al., *Adv. Mater.*, **2011**, 23, 4898

[114] Li, X. S.; Magnuson, C.W.; et al., *J. Am. Chem. Soc.*, **2011**, 133, 2816

[115] Hofmann, U.; Holst, R., *Ber. Dtsch. Chem. Ges.*, **1939**, 72, 754

[116] Ruess, G., *Monatsch. Chem.*, **1946**, 76, 381

[117] Scholz, W.; Boehm, H.-P., *Z. Anorg. Allg. Chem.*, **1969**, 369, 327

[118] Lerf, A.; He, H.; et al., *J. Phys. Chem. B*, **1998**, 102, 4477

[119] Ciszewski, M.; Mianowski, A., *Chemik*, **2013**, 67(4), 267-274

[120] Shao, G.; Lu, Y.; et al., *J. Mater. Sci.*, **2012**, 47, 4400

[121] Du, Q.; Zheng, M.; et al., *Electrochim. Acta*, **2010**, 55, 3897

[122] Park, S.; et al., *Chem. Mater.*, **2008**, 20, 6592

[123] Liu, L.; Zhang, J.; et al., *Nanoscale*, **2012**, 4, 5910

[124] Paci, J.T.; Belytschko, T; et al., *J. Phys. Chem. C*, **2007**, 111, 18099

[125] Gómez-Navarro, C.; Burghard, M.; et al., *Nano Lett.*, **2008**, 8, 2045

- [126] Bortz, D.R.; Heras, E.G.; et al., *Macromolecules*, **2012**, 45, 238
- [127] Li, Z.; Wang, R.; et al., *Polymer*, **2013**, 54, 6437
- [128] Shi, H.; Li, Y.; et al., *J. Appl. Polym. Sci.*, **2013**, 128(5), 3163
- [129] Jin, S.-X.; Zhou, N.-L.; et al., *Coll. Surf. B*, **2013**, 101, 319
- [130] Cheng, H.K.F.; et al., *ACS Appl. Mater. Interfaces*, **2012**, 4, 2387
- [131] Li, W.; Xu, Z.; et al., *Chem. Engin. J.*, **2014**, 237, 291
- [132] Vallés, C.; Kinloch, I.A.; et al., *Comp. Sci. Technol.*, **2013**, 88, 158
- [133] Kim, J.; Cote, L.J.; et al., *Acc. Chem. Res.*, **2012**, 45(8), 1356
- [134] Li, Y.; Yang, J.; et al., *Langmuir*, **2013**, 29, 13527
- [135] Xu, Z.; Gao, C., *ACS Nano*, **2011**, 5(4), 2908
- [136] Boukharov, D.W.; Katsnelson, M.I., *J. Am. Chem. Soc.*, **2008**, 130, 10697
- [137] Gómez-Navarro, C.; Meyer, J.C.; et al., *Nano Lett.*, **2010**, 10, 1144
- [138] Li, H.; Bubeck, C., *Macromol. Res.*, **2013**, 21(3), 290
- [139] Moussa, S.; Atkinson, G.; et al., *J. Mater. Chem.*, **2011**, 21, 9608
- [140] Cote, L.J.; Cruz-Silva, R.; et al., *J. Am. Chem. Soc.*, **2009**, 131, 11027
- [141] Stankovich, S.; et al., *Nature*, **2006**, 442, 282
- [142] Stankovich, S.; et al., *Carbon*, **2007**, 45, 1558
- [143] Shin, H.-J.; Sim, K.K.; et al., *Adv. Funct. Mater.*, **2009**, 19, 1987
- [144] Zhou, X.; Zhang, J.; et al., *J. Phys. Chem. C*, **2011**, 115(24), 11957
- [145] Sun, L.; Yu, H.; et al., *J. Haz. Mat.*, **2012**, 203-204, 101
- [146] Ma, H.-L.; et al., *ACS Appl. Mater. Interfaces*, **2012**, 4(4), 1948
- [147] Fan, Z.; Wang, K., *Carbon*, **2010**, 48(5), 1686
- [148] Zhang, J.; Yang, H.; et al., *Chem. Commun.*, **2010**, 46, 1112
- [149] Su, C.-Y.; Xu, Y.; et al., *ACS Nano*, **2010**, 4(9), 5285
- [150] Chen, D.; Li, L.; et al., *Nanotechnology*, **2011**, 22, 325601
- [151] Pham, T.A.; Kim, J.S.; et al., *Coll. Surf. A*, **2011**, 386, 195
- [152] McAllister, M.J.; Li, J.-L.; et al., *Chem. Mater.*, **2007**, 19, 4396
- [153] Schniepp, H.C.; Li, J.-L.; et al., *J. Phys. Chem. B*, **2006**, 110, 8535
- [154] Kuilla, T.; Bhadra, S.; et al., *Prog. Polym. Sci.*, **2010**, 35, 1350
- [155] Dreyer, D.R.; Park, S.; et al., *Chem. Soc. Rev.*, **2010**, 39, 228
- [156] Singh, V.; Joung, D.; et al., *Prog. Mater. Sci.*, **2011**, 56, 1178
- [157] Hernandez, Y.; Nicolosi, V.; et al., *Nat. Nanotechnol.*, **2008**, 3, 563
- [158] Hernandez, Y.; Lotya, M.; et al., *Langmuir*, **2009**, 26(5), 3208
- [159] Khan, U.; Porwal, H.; et al., *Langmuir*, **2011**, 27, 9077
- [160] Khan, U.; O'Neill, A.; et al., *Small*, **2010**, 6(7), 864
- [161] Barwick, S.; Khan, U.; et al., *J. Phys. Chem. C*, **2013**, 117, 19212
- [162] Liu, W.W.; Wang, J.N.; et al., *Nanoscale*, **2012**, 4, 425
- [163] O'Neill, A.; Khan, U.; et al., *J. Phys. Chem. C*, **2011**, 115, 5422
- [164] Guardia, L.; Fernández-Merino, M.J.; et al., *Carbon*, **2011**, 49, 1653
- [165] Das, S.; Irin, F.; et al., *Polymer*, **2012**, 53, 2485
- [166] Seo, J.-W.T.; Green, A.A., *J. Phys. Chem. Lett.*, **2011**, 2, 1004
- [167] Parviz, D.; Das, S.; et al., *ACS Nano*, **2012**, 6(10), 8857
- [168] Vadukumpully, S.; Paul, J.; *Carbon*, **2009**, 47, 3288
- [169] Lotya, M.; Hernández, Y.; et al., *J. Am. Chem. Soc.*, **2009**, 131, 3611
- [170] Carrasco, P.M.; Montes, S.; et al., *Carbon*, **2014**, 70, 157
- [171] Bourlingos, A.B.; Georgakilas, V.; et al., *Solid State Commun.*, **2009**, 149, 2172

[172] Hao, R.; Qian, W.; et al., *Chem. Commun.*, **2008**, 48, 6576

[173] Hunter, C.A.; Lawson, K.R.; et al., *J. Chem. Soc. Perkin Trans. 2*, **2001**, 651

[174] Alexander, A.E., *J. Chem. Soc.*, **1937**, 1813

[175] Hughes, A., *Proc. Roy. Soc. London Ser. A*, **1936**, 155, 710

[176] Hunter, C.A.; Sanders, J.K.M., *J. Am. Chem. Soc.*, **1990**, 112, 5525

[177] Wheeler, S.E., *Acc. Chem. Res.*, **2013**, 46(4), 1029

[178] Sabatino, A.; La Manna, G.; et al., *J. Phys. Chem.*, **1980**, 84, 2641

[179] Gutman, V., *Electrochim. Acta*, **1976**, 21, 661

[180] Mao, Y.; Bao, Y.; et al., *Talanta*, **2011**, 85, 2106

[181] Xiao, F.-X.; Miao, J.; Liu, B., *J. Am. Chem. Soc.*, **2014**, 136, 1559

[182] Park, J.S.; Cho, S.M.; et al., *ACS Appl. Mater. Interfaces*, **2011**, 3, 360

[183] Lee, D.W.; Hong, T.-K.; et al., *J. Mater. Chem.*, **2011**, 21, 3438

[184] Wang, D.; Wang, X., *Langmuir*, **2011**, 27(5), 2007

[185] Zhu, J.; Zhang, H.; Kotov, N.A., *ACS Nano*, **2013**, 7(6), 4818

[186] Liu, J.; Tao, L.; Yang, W.; et al., *Langmuir*, **2010**, 26(12), 10068

[187] Shen, J.; Hu, Y.; Qin, C.; et al., *Langmuir*, **2009**, 25(11), 6122

[188] Zeng, G.; Xing, Y.; et al., *Langmuir*, **2010**, 26(18), 15022

[189] Zhu, C.; Gio, S.; et al., *Langmuir*, **2010**, 26(10), 7614

[190] Lu, J.; Liu, W.; et al., *RSC Advances*, **2012**, 2, 10537

[191] Zhang, X.; Li, S.; et al., *Chem. Commun.*, **2011**, 47, 4929

[192] Hong, J.-Y.; Shin, K.-Y.; et al., *Chem. Commun.*, **2011**, 47, 7182

[193] Liu, J.; Tao, L.; et al., *Langmuir*, **2010**, 26(12), 10068

[194] Mulhearn, W.D.; Kim, D.D.; et al., *Soft Matter*, **2012**, 8, 10419

[195] Henry, D.C.; *Proc. R. Soc. Lond. A*, **1931**, 133, 106

[196] Hückel, E.; *Phys. Z.*, **1924**, 25, 204

[197] Von Smoluchowski, M., *Z. phys. Chem.*, **1918**, 92, 129

[198] O'Brien, R.W.; White, L.R., *J. Chem. Soc., Faraday Trans. 2*, **1987**, 74, 1607

[199] Antonietti, M.; Vorweg, L., *Colloid Polym. Sci.*, **1997**, 275, 883

[200] Hamaker, H.C., *Trans. Faraday Soc.*, **1940**, 36, 279

[201] González-Cuenca, M.; Biesheuvel, P.M.; et al., *Aiche J.*, **2000**, 46, 626

[202] Ishikawa, R.; Ko, P.J.; et al., *J. Phys.: Conf. Ser.*, **2012**, 352, 012003

[203] Besra, L.; Liu, M., *Prog. Mater. Sci.*, **2007**, 52, 1

[204] Sima, M.; Enculescu, I.; et al., *Optoelectron. Adv. Mat.*, **2011**, 5(4), 414

[205] Wang, M.; Duong, L.D.; et al., *ACS Appl. Mater. Interfaces*, **2014**, 6, 1747

[206] An, S.J.; Zhu, Y.; et al., *J. Phys. Chem. Lett.*, **2010**, 1, 1259

[207] Bon, S.B.; Valentini, L.; et al., *Phys. Status Solidi A*, **2010**, 207(11), 2461

[208] Koh, A.T.T.; Foong, Y.M.; et al., *Appl. Phys. Lett.*, **2012**, 101, 183107

[209] Lee, S.; Cho, M.S.; et al., *J. Mater. Sci.*, **2013**, 48, 6891

[210] Lin, Y.; Jin, J.; et al., *J. Phys. Chem. C.*, **2013**, 117, 17237

[211] Su, Y.; Zhitomirsky, I., *Coll. Surf. A*, **2013**, 436, 97

[212] Wu, Z.-S.; Pei, S.; et al., *Adv. Mater.*, **2009**, 21, 1756

[213] Li, X.; Zhang, G.; Bai, X.; et al., *Nature Nanotech.*, **2008**, 3, 538

[214] Kim, H.; Mattevi, C.; Kim, H.J.; et al., *Nanoscale*, **2013**, 5, 12365

[215] Zheng, Q.; Ip, W.H.; et al., *ACS Nano*, **2011**, 5(7), 6039

[216] Park, K.H.; Kim, B.H.; et al., *Nano Lett.*, **2012**, 12, 2871

[217] Sutar, D.S.; Narayanan, P.K.; et al.; et al., *Thin Solid Films*, **2012**, 5991

- [218] Jia, B.; Zou, L., *Chem. Phys. Lett.*, **2013**, 568-569, 101
- [219] Ramesh, W.; Rink, H.P., US2007059451 A1, **2007**
- [220] Giannakopoulos, I.; Taylor, A.C., *Prog. Org. Coat.*, **2013**, 76, 1556
- [221] Tsai, K.C.; Kuan, C.F.; et al., *J. Appl. Polym. Sci.*, **2013**, 127, 1084
- [222] Sun, G.; Cho, S.; et al., *J. Am. Chem. Soc.*, **2013**, 135, 4203
- [223] Jung, Y.; Jun, T.; et al., *J. Mater. Chem.*, **2011**, 21, 11879
- [224] Jung, Y.; Yeo, T.H.; et al., *J. Phys. Chem. C*, **2011**, 115, 25056
- [225] Hill, L.W.; Kozlowski, K., *J. Coat. Technol.*, **2007**, 51, 63
- [226] Zhang, W.R.; Zhu, T.T.; Smith, R., *Prog. Org. Coat.*, **2010**, 69, 376
- [227] Hamada, T.; Kanai, H.; Koike, T., *Prog. Org. Coat.*, **1997**, 30, 271
- [228] Snyder, D.M.; Vuk, T.J., *J. App. Polym. Sci.*, **1992**, 46, 1301
- [229] Bauer, D.R.; Budde, G.F., *J. App. Polym. Sci.*, **1983**, 28, 253
- [230] Radicevic, R.; Jovicic, M.; et al., *Prog. Org. Coat.*, **2011**, 71, 256
- [231] Dentinger, P.M.; Taylor, J.W., *J. Vac. Sci. Technol. B*, **1998**, 16, 3759
- [232] Berge, A.; Kvæven, B.; Ugelstad, J., *Eur. Polym. J.*, **1970**, 6(7), 981
- [233] Weber, B.; Bremser, W.; Hiltrop, K., *Prog. Org. Coat.*, **2009**, 2-3, 150
- [234] HM Coalition, *High Production Volume (HPV) Challenge Program, FINAL SUBMISSION for HEXAMETHOXYMETHYLMELAMINE*, **2004**
- [235] Larson, A.C.; Cromer, D.T., *J. Chem. Phys.*, **1974**, 60, 185
- [236] Ma, H.A.; Jia, X.; et al., *Chem. Phys. Lett.*, **2003**, 368, 668
- [237] Glówka, M.L.; Iwanicka, I., *Acta Cryst.*, **1989**, C45, 1765
- [238] Ng, S.W.; *Acta Crys.*, **2012**, E68, o3201
- [239] Lifshitz, I.M.; Slyozov, V.V., *J. Phys. Chem. Sol.*, **1961**, 19(1-2), 35
- [240] Wagner, C., *Zeitschr. f. Elektrochem.*, **1961**, 65(7), 581
- [241] Griffin, W.C., *J. Soc. Cosm. Chemists*, **1954**, 5, 259
- [242] Hansen, C., *Hansen Solubility Parameters: A User's Handbook*, 2nd ed., CRC Press, Boca Raton, **2007**
- [243] Brock, T.; Groteklaes, M., *European Coatings Handbook*, Vincentz, Hannover, **2000**
- [244] Chandler, W.D.; Lee, E.J.; Lee, D.G., *J. Chem. Educ.*, **1987**, 10, 878
- [245] Marchewka, M.K., *Mat. Sci. Engineering*, **2002**, B95, 214
- [246] Larkin, P.J.; Makowski, et al., L.A., *Vibrational Spectroscopy*, **1998**, 17, 53

DECLARATION

I declare that I have completed this thesis without help of a second party and only with the assistance acknowledged therein. I have appropriately acknowledged and referenced all text passages that are derived literally from or are based on the content of published or unpublished work of others, and all information that relates to verbal communications.

LIST OF TABLES

Table 1.1: Physical properties of graphene.....	14
Table 2.1: Charge carrier mobilities	31
Table 2.2: Acronyms of graphene prepared by different methods	41
Table 2.3: Graphene oxide - polymer composites	49
Table 2.4: Aqueous Graphene Dispersions	55
Table 2.5: Published layer-by-layer assemblies of graphene	61
Table 2.6: Graphene thin films by anodic electrodeposition	67
Table 2.7: Graphene thin films by anodic electrodeposition	67
Table 2.8: Macroscopic physical properties of HMMM	70
Table 2.9: Crystallographic data of selected triazine compounds	70
Table 2.10: Distinction between binary liquid systems by droplet diameter.....	71
Table 3.1: Hansen solubility parameters of water and HMMM	76
Table 4.1: HMMM ring vibrations before and after particle synthesis	95
Table 5.1: FTIR bands of HMMM and G-M [⊖]	109
Table 6.1: Selected IR vibrations of MP and G-MP [⊕]	126

LIST OF FIGURES

Figure 2.1: (a) Graphite; (b) Graphite top view; (c) Floating graphene sheet; (d) Electron density map of single layer graphene.....	23
Figure 2.2: (a) Real space crystal lattice of graphene; (b) 1st Brillouin zone of graphene unit cell	24
Figure 2.3: (a) Electronic dispersions of graphene; (b) Electronic dispersion in 1st Brillouin zone 3D; (c) Full density of states; (d) Density of states around Dirac point (analytical solution)	26
Figure 2.4: Graphene lattice with pseudospin (a) up and (b) down.....	29
Figure 2.5: (a) Graphene on Si/SiO ₂ substrate, inset: microscopic image; (b) Electrostatic potential puddles of graphene on Si/SiO ₂ ; (c) Suspended graphene exhibiting flexural phonons as primary scattering mechanism; (d) Point defects and edges as secondary source of scattering in suspended graphene	32
Figure 2.6: (a) n-doping in tetrathiafulvalene decorated graphene; (b) p-doping in melamine decorated graphene	33
Figure 2.7: (a) 1st Phonon Brillouin zone; (b) Phonon dispersions of graphene, Kohn anomalies around G and K are depicted as red lines; (c) G band transitions of graphene; (d) Ring breathing A _{1g} mode; (e) E _{2g} mode; (f) Double resonance process leading to G' band	37
Figure 2.8: Dependence of G' band on graphene layer number.....	39
Figure 2.9: Micromechanical cleavage of HOPG	42
Figure 2.10: Graphitization of 6H-SiC	43
Figure 2.11: Chemical vapor deposition techniques for graphene production	45
Figure 2.12: Oxidation of graphite to graphite oxide according to Hummer's method	46

Figure 2.13: Reduction methods leading to reduced graphene oxide.....	51
Figure 2.14: Ultrasound-assisted exfoliation of graphite in organic solvents to single layer graphene dispersions; pictures relate to exfoliation in NMP.....	52
Figure 2.15: Layer-by-layer assembly of positively (red) and negatively (green) charged graphene sheets	62
Figure 2.16: Process illustration of C-ED of charged graphene dispersions	64
Figure 2.17: (a) Lewis formula of HMMM and (b) 3D model of HMMM; 3D model adopted from calculated structure.....	68
Figure 3.1: Phase diagrams of (a) freshly prepared EME and (b) aged EME	77
Figure 3.2: (a) ME droplet diameter as function of time; (b) E droplet diameter as function of time; (c) pH value as function of time; (d) E and ME droplet diameters as function of HMMM concentration	79
Figure 3.3: (a) Concentration and time-dependent phase behavior of aqueous HMMM systems; (b) Mechanism of HMMM microemulsion formation.....	80
Figure 3.4: (a) Development of HMMM droplet diameter upon temperature increase; (b) Phase inversion temperature as function of HMMM concentration; (c) Emulsion and microemulsion droplet size as function of temperature.....	81
Figure 4.1: Concentration limits of HMMM and proton concentration for successful nano particle synthesis.....	89
Figure 4.2: Temperature and time-resolved hydrodynamic diameters as means to monitor the HMMM nano particle reaction	90
Figure 4.3: Reaction mechanism of HMMM self-condensation	91
Figure 4.4: (a) Exemplary polynomial fit ($c_{\text{RCH}_2\text{OCH}_3} = 0.3$); (b) Initial rate as function of initial proton concentration, constant temperature; (c) Initial rate as function of initial proton concentration, constant initial $R_{\text{CH}_2\text{OCH}_3}$ concentration; (d) Arrhenius plot.....	93
Figure 4.5: (a) Proton conversion as function of time; (b) Proton conversion rate as function of conversion; (c) maximum conversion rate as function of reaction temperature	94
Figure 4.6: (a) FTIR and (b) XRD spectra of HMMM and MP.....	96

Figure 4.7: (a) Hydrodynamic diameter as function of initial proton concentration; (b) AFM image of MP spray coated on Si wafer; (c) and (d) SEM images of MP on Si wafer at different magnification	98
Figure 4.8: (a) Double dimethylene ether bridge between two MP molecules; (b) top view of two MP molecules	95
Figure 4.9: Illustrative mechanism of MP synthesis covering EME phase inversion, solubilization of HMMM and particle growth	99
Figure 5.1: Ultrasonic exfoliation of graphite yielding G-M^\ominus	103
Figure 5.2: (a) Exfoliation kinetics of G-M^\ominus , inset shows UV-VIS spectra of graphite and G-M^\ominus ; (b) dilution series of G-M^\ominus ; (c) Isoelectric titration of G-M^\ominus between pH 2 and 11	107
Figure 5.3: (a) Lewis structure of HMMM; (b) 3D representation of HMMM; (c) electrostatic potential map; (d) LUMO map.....	108
Figure 5.4: Energy diagram of graphene and HMMM.....	108
Figure 5.5: (a) UV-VIS spectra of aq. HMMM and G-M^\ominus ; (b) FTIR spectra of HMMM and G-M^\ominus	110
Figure 5.6: Raman spectra of G-M^\ominus ; (a) full spectra of G-M^\ominus and graphite; (b) G band; (c); G' band of graphite; (d) G' band of G-M^\ominus	111
Figure 5.7: (a) XRD spectra of graphite, aqueous HMMM and G-M^\ominus ; (b) magnification of mid-angle range.....	112
Figure 5.8: (a) AFM image of G-M^\ominus ; (b) cross-section of a single particle; (c) hydrodynamic diameters of G-M^\ominus ; (d) SEM image of vacuum dried G-M^\ominus film	113
Figure 5.9: (a) Top view and (b) perspective view of G-M^\ominus ; (c) Charge transfer from graphene to HMMM resulting in total negative charge of the nano composite	114
Figure 6.1: Ultrasonic exfoliation of graphite in MP yielding G-MP^\oplus	119
Figure 6.2: Isoelectric titration of G-MP^\oplus between pH 2 and 11	121
Figure 6.3: XRD patterns of graphite, MP and G-MP^\oplus ; (a) total spectra and (b) magnification of angles 0 to 40 $^\circ 2\Theta$	122

Figure 6.4: (a) AFM image of G-MP [⊕] ; (b) AFM image and 3D image showing MP adsorbed to graphene; (c) cross-section of a single particle; (d) hydrodynamic diameters of G-MP [⊕] ; (e) SEM image of vacuum dried G-MP [⊕] film	123
Figure 6.5: (a) UV-VIS spectra of MP and G-MP [⊕] ; (b) FTIR spectra of MP and G-MP [⊕] , inset shows full spectrum; (c) Raman spectra of graphite and G-MP [⊕]	125
Figure 6.6: Interaction mechanisms in G-MP [⊕]	126
Figure 6.7: Structure of G-MP [⊕]	127
Figure 7.1: Process scheme for C-ED of G-MP [⊕]	131
Figure 7.2: AFM image processing to reveal graphene substructure (C-ED_10-5-10 ⁻⁴)	133
Figure 7.3: (a) Deposition kinetics of C-ED of G-MP [⊕] ; (b) Film thickness of C-ED_U-t-10-3 as function of time and voltage; (c) Film thickness of C-ED_U-t-10-4 as function of time and voltage; (d) Electrical conductivities of C-ED_U-5-c and C-ED_U-10-c films	134
Figure 7.4: SEM images of C-ED_10-600-10-3 films; (a) top view and (b) top view after partial ablation of coagulated MP top layer	139
Figure 7.5: Development of film during C-ED of G-MP [⊕] (C-ED_7-t-10 ⁻³)	137
Figure 7.6: Mechanism of G-MP [⊕] deposition	136
Figure 7.7: Nanomechanical analysis of C-ED_10-10-10 ⁻³ ; (a) height profile; (b) DMT modulus map; (c) Dissipation map; (d) Adhesion map	136
Figure 7.8: SEM images of A-ED films from G-M [⊖] ; (a) and (b) were recorded at different magnifications	Fehler! Textmarke nicht definiert.
Figure 7.9: Illustration of C-ED of G-MP [⊕]	140
Figure 8.1: Layer-by-layer assembly process scheme (one cycle) for both dip- and spray deposition	145
Figure 8.2: AFM (a) height profile and (b) Inphase image of negatively charged glass substrates; AFM (c) height profile and (d) phase image of PEI modified positively charged glass substrates	147
Figure 8.3: pH range for successful LBL assembly of G-M [⊖] and G-MP [⊕]	148

Figure 8.4: Optical and surface properties of dip- and spray assemblies; (a) Absorption as function of double layer count; (b) Transmission as function of double layer count; (c) calculated film thickness as function of double layer count; (d) Mean roughness as function of double layer count.....	149
Figure 8.5: SEM images of D-LBL10 and S-LBL10 with different magnifications.	150
Figure 8.6: Evolution of film morphology for D-LBL and S-LBL with increasing number of double layers	152
Figure 8.7: Layer-by-layer assembly of G-M [⊖] and G-MP [⊕] resulting in nano composite films	153